I DESIGN, CONTROL, AND CHARACTERIZATION OF THE PASSIVELY MODE LOCKED CW DYE LASER

II PHOTOCONDUCTIVE IMPULSE RESPONSE AND EXCESS CARRIER LIFETIME OF Cr-DOPED GaAs

Thesis by

Pinchas Agmon

In Partial Fulfillment of the Requirements

for the Degree of

Doctor of Philosophy

California Institute of Technology

Pasadena, California

1980

(Submitted June 25, 1979)

To

Nava

Liad

Roey

and My Parents

with Love

ACKNOWLEDGMENTS

Several persons deserve my gratitude for their assistance in bringing this work to a successful conclusion. Above all, I am grateful to Professor Amnon Yariv for granting me the privilege of being a member of his research group at Caltech. I enjoyed his physical insight and keen scientific intuition which made his advice and comments invaluable.

I would like to thank Mr. R. H. Moyer for his collaboration in most of the experimental work reported here, and for critically proofreading this manuscript. Also thanks go to Mr. T. Koch for his contribution to this research.

I wish to acknowledge Professor D. L. Smith of Caltech, Dr. E. P. Ippen of Bell Laboratories, and Dr. S. Margalit of the Technion, Israel, for fruitful discussions. Dr. A. C. Livanos and Dr. A. Katzir are appreciated for their collaboration and friendship.

Special thanks go to Mr. D. Armstrong, without whose technical assistance many of the experiments might have been delayed or deleted. Thanks also to Mrs. Ruth Stratton for her masterful typing of this thesis.

My greatest debt is to my wife, Nava. No words can describe the love, devotion, and support she gave me all along.

ABSTRACT

This thesis consists of two parts. The subject of the first part is the design, control, and characterization of the passively mode locked CW dye laser, which is capable of producing a stable continuous train of subpicosecond pulses. Following a description of the laser's elements, the mode stability of its multi-mirror resonator is studied. The monitoring of the laser operational state by pulsewidth and bandwidth measurements is described.

In the second part, the photoconductive impulse response and excess carrier lifetime of semi-insulating Cr:GaAs is studied experimentally and analytically. In the transient photoconductive experiment, the material is irradiated with a continuous train of picosecond light pulses with photon energy above the band-gap energy, generated by the passively mode locked CW dye laser described in part I. A photoconductive decay time of 67 psec is deduced from the observations and interpreted as the result of both bulk and surface recombination. It is shown that it agrees well with longer carrier lifetime in Cr:GaAs measured under steady state conditions with longer illumination wavelengths.

TABLE OF CONTENTS

Part I

Design, Control, and Characterization of the Passively Mode Locked CW Dye Laser

Part II

Photoconductive Impulse Response and Excess Carrier Lifetime of Cr-Doped GaAs

Part I

DESIGN, CONTROL, AND CHARACTERIZATION OF THE PASSIVELY MODE LOCKED CW DYE LASER

Chapter 1

THE MODE LOCKED LASER--GENERAL INTRODUCTION

1.0 Introduction

Light pulses have been used to study physical processes for hundreds of years. A dramatic improvement in the time resolution took place about fifteen years ago when the mode locked laser was invented. A He-Ne laser was the first to be mode locked, as reported by Hargrove et al. in 1964 [1]. Since then, several methods and many configurations have been demonstrated which produce ultrashort pulses by locking the phases of the laser's modes. To date, pulses as short as 0.3 picoseconds have been reliably generated by some laser oscillators. Analytic models have been developed to a degree that they agree, at least qualitatively, with experimental results.

In 1975-76 when I looked into the possibilities of studying ultrafast phenomena in semiconductors by picosecond light pulses, I found the field of mode locking in a stage of advanced research, but not yet developed to a useful level of practicability. Many investigators had demonstrated the possibility of generating ultrashort optical pulses, but very few had developed mode locked lasers which could have been used as reliable tools in other experiments. The most thoroughly developed mode locked laser at that time was the Nd:glass which produced bursts of picosecond pulses with relatively high energies ($\sim$ mJ/pulse). However, in 1974 a CW dye laser had been mode locked to generate a continuous train of subpicosecond kilowatt pulses [2]. The power stability of this laser was further improved in the subsequent year [3], thus making it the most appropriate laser system to the experiments I planned.

The design, control, and characterization of the passively mode locked CW dye laser is the subject of Part I. In light of the work of other investigators, the emphasis will be on original and unpublished material, and the reader will be referred to the literature when possible.

Before embarking on the subject itself, the concept of mode locking and several methods used to realize it will be briefly reviewed.

1.1 The Concept of Mode Locking

The total electromagnetic field in the laser oscillator is the superposition of all the oscillating modes:

$$\vec{E}_{tot}(x,t) = \sum_n \vec{E}_n(x,t) \qquad (1.1.1)$$

where $E_n(x,t)$ is the electric field amplitude and phase of the n^{th} mode. In general, the modes are not correlated and have random amplitude and phase. The output power, thus, will fluctuate due to interference between the modes, and its frequency bandwidth will be large. More ordered output is expected if this randomness is removed. Allowing only the fundamental Gaussian modes to oscillate, order can be increased in one of two ways: either by eliminating all but one mode, thus trivially avoiding the random interference, or, alternatively, order can be increased by locking all the relative phases, so that the interference is not random.

The first kind described is the single mode, or monochromatic laser, while the second is the mode locked laser which generates short pulses. The short pulses produced by the mode locked laser are a consequence of the coherent interference between the modes. To see this, assume that the modes are plane wave modes of the Fabry-Perot resonator with unit amplitude; then

$$E_{tot} = \sum_n e^{i[(\omega_o + n\Delta\omega)t + \phi_n(t)]} \qquad (1.1.2)$$

in which $\Delta\omega \equiv \pi \frac{c}{L}$, c is the speed of light, L is the length of the cavity, and $\phi_n(t)$ is the phase of mode n. Let all the phases be locked so that $\phi_n(t) = \phi$, then

$$E_{tot}(t) = e^{i[\omega_o t + \phi]} \frac{\sin(N\omega t/2)}{\sin(\omega t/2)} \qquad (1.1.3)$$

where N is the number of oscillating modes. The power, P, is proportional to $|E_{tot}(t)|^2$, so that

$$P(t) \alpha \quad \frac{\sin^2 N\omega t/2)}{\sin^2(\omega t/2)} \qquad (1.1.4)$$

The output is thus a train of pulses, separated in time by 2L/c, and in space by 2L. The pulse width is $\Delta t \sim \frac{2\pi}{N\Delta\omega} \sim \frac{1}{\Delta\nu_\ell}$, where $\Delta\nu_\ell$ is the total band width spanned by the oscillating modes.

1.2 Methods of Mode Locking

Consider first a steady state situation in which a pulse is traveling back and forth in a laser resonator, gated by a shutter. If the shutter opens only when the pulse arrives at it, and closes immediately after the pulse has passed through, then the pulse does not "see" the shutter at all, and the modes, which are its Fourier components, will oscillate without perturbation. All other modes that might be present in the laser resonator will suffer high loss, and consequently will not oscillate.

This simple model, although not covering all the methods used to obtain mode locking, is very helpful in practical considerations of the construction of mode locked lasers.

The ideal shutter keeps the phases of the modes locked. The various methods of mode locking differ from one another mainly by the device or medium which plays the role of this shutter. In the first demonstration of mode locking, a visible He-Ne laser and an ultrasonic diffraction modulator were employed [1]. Shortly afterwards, Yariv [4] showed that mode locking of an inhomogeneously broadened laser can be predicted from Maxwell's equations when either the conductivity (i.e., the loss or the gain) or the dielectric constant (i.e., the phase) is perturbed harmonically. When an acoustooptic or electrooptic modulator is inserted into the cavity to lock the modes, the method is called active mode locking, because the modulator is driven by a source independent of the laser.

Under the category of mode locking by gain modulation, we can include the synchronously mode locked laser. Here one laser is actively mode locked to generate short pulses which are then employed to pump another laser. The optical lengths of the cavities of the two lasers must be matched.

In contrast to active mode locking, passive mode locking does not require any external source to drive the shutter, and the control is provided by the laser itself. The technique is based on the transmission characteristic of saturable absorbers (usually dye solutions), as shown in Figure 1.2.1. The absorption coefficient is a function of the intensity and often can be approximated by

$$\alpha(I) = \frac{\alpha_o}{1 + I/I_s} \qquad (1.2.1)$$

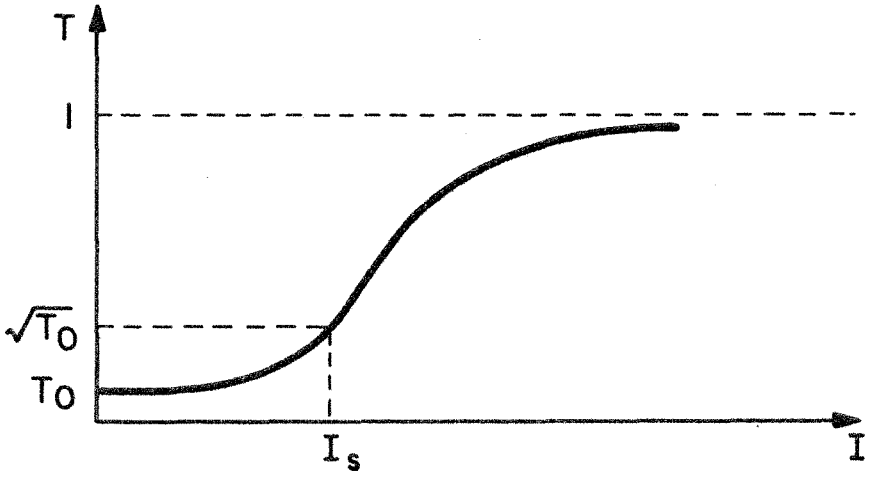

Fig. 1.2.1 Typical dependence of a saturable absorber transmission on intensity.

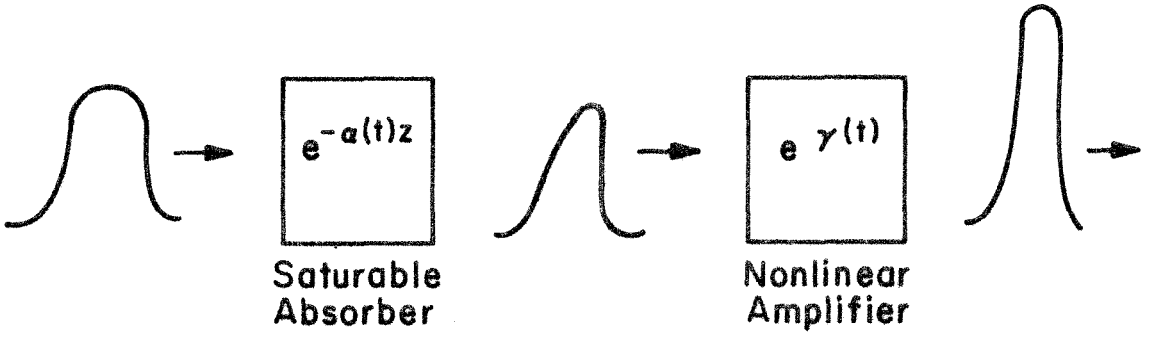

Fig. 1.2.2 Pulse narrowing by a combination of a saturable absorber and a nonlinear amplifier.

I_s is called the saturation intensity. Typically, for dyes suitable for mode locking, $I_s \sim 10^4$-10^7 W/cm^2 (see Sections 2.3 and 2.4).

When passing through a saturable absorber cell, high power pulses suffer minimum loss due to their bleaching action. Using this property of the dye, it is possible to operate the laser such that only a single pulse travels in the cavity, while all the smaller pulses have been attenuated. Visualizing the saturable absorber as a shutter, it can be considered open when the dye is bleached by the leading edge of the pulse, and closed when the absorption of the dye has recovered to its small signal value. For good mode locking, the absorption band of the dye must contain the lasing bandwidth, and its absorption recovery time must be shorter than the round trip time of the pulse in the resonator (assuming the absorber dye cell is near one end of the cavity). Garmire and Yariv [5] showed that the resulting pulse will have duration equal to the recovery time of the saturable absorber. This is expected in light of the simple shutter model described at the beginning of this section.

Pulses which are considerably shorter than the recovery time of the saturable absorber can be generated by a combination of a saturable absorber and a nonlinear amplifier (i.e., the saturable gain medium). To understand the process involved, we assume that a pulse is already traveling back and forth in the cavity. Let us follow Figure 1.2.2. When the leading edge of the wide pulse at the left is absorbed, it bleaches the saturable absorber and the rest of the pulse is transmitted with a minimum of loss. The pulse is thus sharpened asymmetrically. Then it passes through the gain medium. The inversion, which is finite, can be greatly

reduced or even eliminated in the process of amplifying the front edge and the peak of the pulse, leaving little gain for the trailing edge. This will further narrow the pulse. This is the principle beyond the passively mode locked CW dye laser which has generated the shortest pulses to date ($\sim$ 0.3 psec).

1.3 Outline of Part I

In Chapter 2, the passively mode locked CW dye laser system is described in detail. Its multi-mirror resonator is analyzed in Chapter 3. In Chapter 4, the monitoring of the laser operation by pulse and band width measurements is discussed, while the control of the system and its output characteristics are described in Chapter 5.

Chapter 2

THE PASSIVELY MODE LOCKED CW DYE LASER

2.0 Introduction

Several configurations of passively mode locked CW dye lasers which produce subpicosecond pulses have been demonstrated [3],[6]. They are all based on a combination of a slow saturable absorber (with recovery times up to a few nanoseconds) and a nonlinear amplifier. The differences are generally in the optical resonator or the dyes used.

The configuration which will be described here was suggested and demonstrated first by Ippen and Shank [3], but much of the understanding of its behavior was not available and had to be derived here. In this laser, rhodamine 6G is employed as a gain medium, and a mixture of DODCI(3,3'-diethyloxadicarbocyanine iodide) and malachite green is used as a saturable absorber. The output pulses are about 1 psec in duration and are chirped. After compression, their duration can be reduced to $\sim$ 0.3 psec. The absorption band of the absorber limits the tunability to the range of 5900-6150Å. The shortest pulses are obtained within the range of 6100-6150Å.

This chapter starts with a discussion of the mode locking process in the laser. Then, before describing the dyes used in the system, the general properties of dyes are briefly reviewed. Next, the basic configuration of the passively mode locked CW dye laser is presented. The acoustooptic device, used to couple the pulses out of the cavity, is then discussed in detail. Finally, the laser configuration, which has been employed for the experiments reported in the second part of this

thesis is described.

2.1 Mode Locking of a Dye Laser by a Combination of a Saturable Absorber and a Nonlinear Amplifier

In Section 1.2 we saw that when a single saturable absorber is used for mode locking, its recovery time imposes a lower limit on the pulse duration [5]. However, when the saturable absorber is required to control only the leading edge, while the trailing edge is being controlled by the nonlinear amplifier, much narrower pulses can be obtained. A schematic drawing of such a system is shown in Figure 2.1.1. Mathematically, the process can be described by the net gain $\Gamma(t) = \gamma(t) - \alpha(t)$, where $\gamma(t)$ is the amplifier's gain coefficient, and $\alpha(t)$ is the loss coefficient of the saturable absorber. Sharpening of the pulse occurs if $\Gamma(t)$ is positive only in the neighborhood of the peak of the pulse.

The requirements of the resonator and the dyes are [7]: 1) The relaxation time of the amplifying medium should be on the order of the cavity round trip. 2) The absorption cross-section of the absorber is more than twice as large as the amplification cross section of the gain medium. The first requirement ensures correct timing of the arrival of the pulse at the amplifier, while the second ensures that the absorber saturates before the gain medium does. Dyes suitable for use as gain media typically recover within 5 nsec. Consequently, equilibrium is quickly established between radiation in the cavity and the population inversion of the dye molecules. This is in contrast to mode locked solid state lasers, where the recovery time is much longer, so that once depleted the gain never recovers within the duration of the pump pulse.

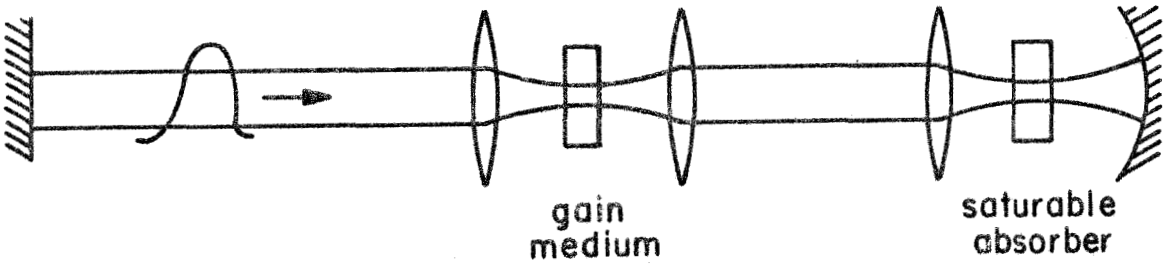

Fig. 2.1.1 Basic configuration of a CW dye laser mode locked by a combination of a saturable absorber and a nonlinear gain medium.

An analytic model which had been proposed by New [7],[8] was refined by Haus [9], who arrived at closed form expressions for the shape, width, and energy of the pulse. The parameters he used to describe the system are the line width, the saturation energies of both dyes, the ratio between the absorbing and amplifying cross-sections, and the ratio of the cavity round trip to the laser medium relaxation time. Haus found that the intensity profile of the pulse is that of a squared secant hyperbolic, i.e.,

$$I(t) \propto \frac{1}{\cosh^2(t/\tau_p)} \qquad (2.1.1)$$

where τ_p is a constant which is related to the pulse width. The pulse width itself was found to be inversely proportional to the prism band width (or any other dispersive element), to the pulse energy, and to the square root of the small signal value of the absorber loss.

Until now, we have not considered the evolution of picosecond pulses from a free running laser. Initially, there are intensity fluctuations which result from the spontaneous emission. When the saturable absorber is inserted into the cavity, short pulses evolve from these fluctuations in a manner similar to that described in Section 1.2. The randomness which is inherent in this process explains the imperfect periodicity in the pulse train emitted from the laser, as well as the incomplete mode locking and the background energy observed between pulses.

The nonlinearity of the process speeds up the narrowing of the pulse. New [8] calculated that it narrows by about $\sqrt{2}$ every cavity round trip. Yasa et al. [10] found that 150-190 round trips are required in

order to achieve a steady state with the narrowest possible pulse.

2.2 General Properties of Dyes

The properties of dyes used in the laser are important for correct design and construction of the system. From the discussion in Section 2.1, it is clear that for mode locking, knowledge of the recovery times and absorption cross section of the dyes is essential. This is in addition to parameters such as the quantum efficiency and losses which affect the performance of free running lasers. Before describing the properties of the dyes used in our laser, we will briefly discuss properties of dyes in general.

An energy level diagram of a typical dye molecule is shown schematically in Figure 2.2.1 [11]. The vibrational-rotational states are grouped according to their electronic states which are separated by about 10000-20000 cm^{-1}. The vibrational levels are separated by about 1000 cm^{-1}, and the rotational levels by 1-10 cm^{-1}. The electron spin is used to classify the states as singlet S and triplet T states. In reality these states are mixed due to spin-orbit interaction.

When a molecule is excited from S_0 to S_1, say by absorbing a photon, it thermalizes to the bottom of S_1 within several picoseconds [11]. This relaxation time might play an important role in synchronously pumped mode locked dye lasers, when the pumping pulses are of duration of several picoseconds. Once at the bottom of S_1, a molecule can change its excitation state by one of the following

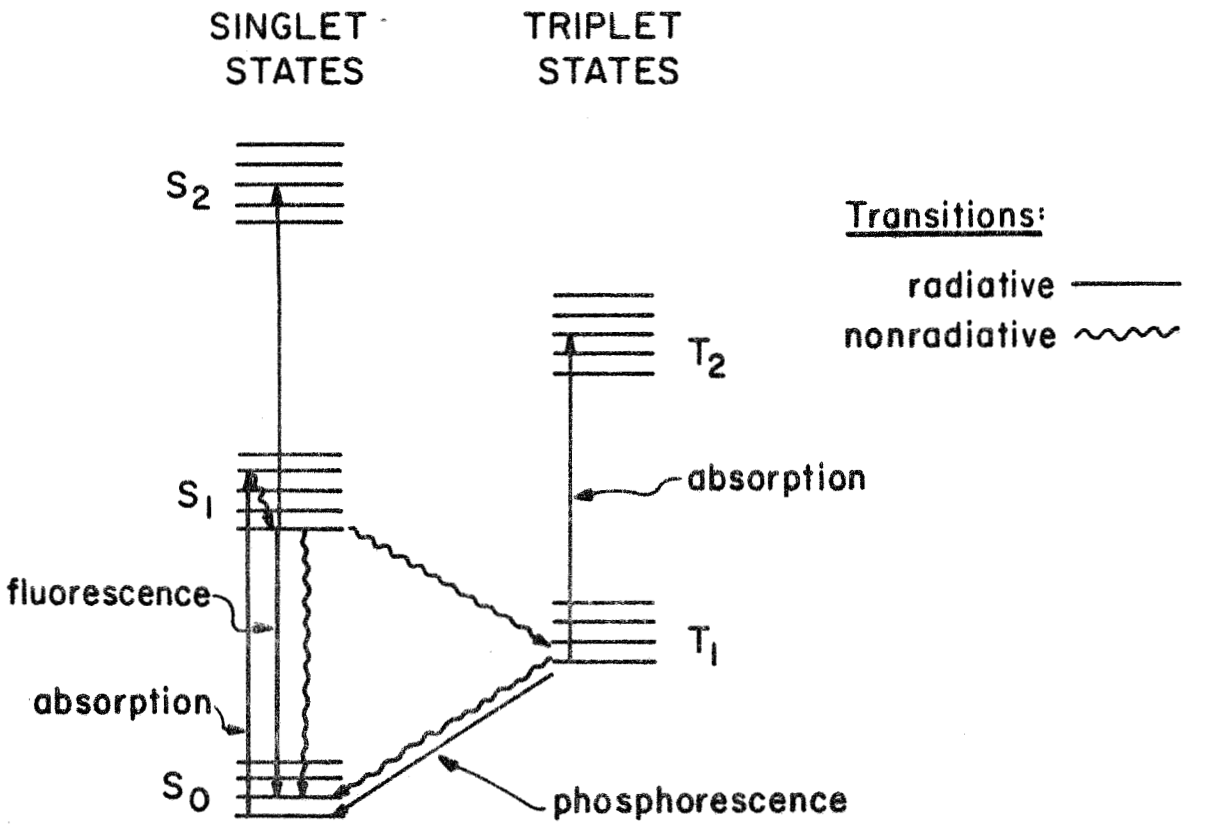

Fig. 2.2.1 A schematic energy level diagram of a dye molecule [11].

competing processes: 1) Radiative relaxation to S_0 (fluorescence), 2) second excitation to a higher singlet state by absorbing another pumping photon, 3) nonradiative internal transition between S_1 and S_0, and 4) nonradiative transition to T. The probability of this last transition is enhanced by the mixing between S and T states.

Populating T_1 has several effects on the dye laser performance: It reduces the population inversion between S_1 and S_0 and it increases absorption of laser photons by $T_1 \rightarrow T_2$ transition.

Several spectral properties are common to many dyes [11]: 1) The fluorescence peak occurs at wavelengths which are longer than that of the principal absorption peak. The fluorescence spectrum is generally a mirror image of that of the principal absorption band, and its width is on the order of 1000 cm^{-1}. 2) The fluorescence lifetime is typically $\sim$ 5 ns. 3) After optical irradiation, new long-lived photoisomers are formed which might absorb at a different band. This formation may or may not be reversible, depending upon the dye and the irradiation intensity.

The formation of the photoisomer, as well as the relatively long lifetime of the T_1 level (10^{-9} to 10^{-3}sec), implies that for CW operation the dye must be replenished continuously. In our laser, for instance, the dye circulates through a reservoir which gives it ample time to relax to its ground state.

2.3 The Gain Medium

The dye rhodamine 6G was chosen as the gain medium of the laser because of its high quantum efficiency ($\simeq$ 0.83 [12]). Its emission

ranges from 5700Å to 6400Å, so that its bandwidth is $\Delta\nu \simeq 2000\ cm^{-1}$. The fluorescence lifetime of rhodamine 6G is $\sim$ 5 nsec [13]. Consequently, the cavity length is chosen to be about 150 cm (10 nsec for a round trip). As a result, the population inversion of the gain medium is recovered to a degree which allows the net gain, $\Gamma(t)$, to be positive only at the neighborhood of the pulse peak (see Section 2.1).

The saturation intensity (at which the absorption coefficient is reduced by a factor of 2) can be easily calculated from

$$I_s(\nu) = \frac{h\nu}{2\tau\varepsilon(\nu)} \qquad (2.3.1)$$

where $h\nu$ is the photon energy, τ is the excited state lifetime, and $\varepsilon(\nu)$ is the extinction coefficient. At the optical pump wavelength, $\lambda = 5145$Å, [27]

$$\varepsilon(5145\text{Å}) = 2.25 \times 10^{-16} cm^2$$

so that

$$I_s(5145\text{Å}) = 1.7 \times 10^5 W/cm^2 \qquad (2.3.2)$$

To minimize degradation of the dye, and thus to allow CW laser operation, the dye solution is circulated. This way, molecules which have been transformed to photoisomers are replaced with unexcited ones. The dye solution flows with a velocity of 10-12 m/sec, so that for a beam spot size of 30 μm diameter, a dye molecule traverses the irradiated area in less than 3 μsec.

To reduce reflection losses and etalon effects, the dye flows in free air. The solvent is ethylene glycol which, due to its viscosity, can be formed into a clean, flat jet by a nozzle which has a nearly

rectangular cross section [14]. The cross section dimensions were measured to be 1.58 x 0.39 mm. However, the jet is not uniformly thick. As a result, the gain of the dye laser, which is an important factor in good mode locking (see Section 2.1), depends on the position of the irradiated area across the jet. Therefore, the jet thickness profile is of interest. It can be found by measuring the transmission of the argon laser beam (λ = 5145Å) through it, as shown, for example, in Figure 2.3.1. The curve indicates that the jet is about three times thicker near its edges than at its center.

2.4 The Saturable Absorber Medium

The saturable absorber medium is a composite of two dyes, DODCI(3,3'-diethyloxidicarboncyanine iodide) and malachite green, in ethylene glycol solution. DODCI is a slow saturable absorber: Its fluorescence lifetime is about 1.2 nsec [15],[17],[18], which is much longer than the subpicosecond pulses generated by DODCI mode locked dye lasers. Its absorption and fluorescence spectra are shown in Figure 2.4.1a [15]. The dashed area indicates the range over which DODCI may be used to mode lock rhodamine 6G lasers [16]. Clearly, the mode locking range is broader than the absorption band. This seeming discrepancy led to the suggestion that a fraction of the DODCI is transformed into a photoisomer which absorbs at longer wavelengths [16]. The spectra of absorption (solid line) and probable fluorescence (broken line) of the photoisomer are shown in Figure 2.4.1b [15]. The ground state lifetime of the photoisomer is $\sim$0.3 msec [15]. The fluorescence lifetime of DODCI is about 1.2 nsec [15,[17],[18]. Shorter absorption recovery times (250 ps [19] and 10 ps [20]) were measured with high

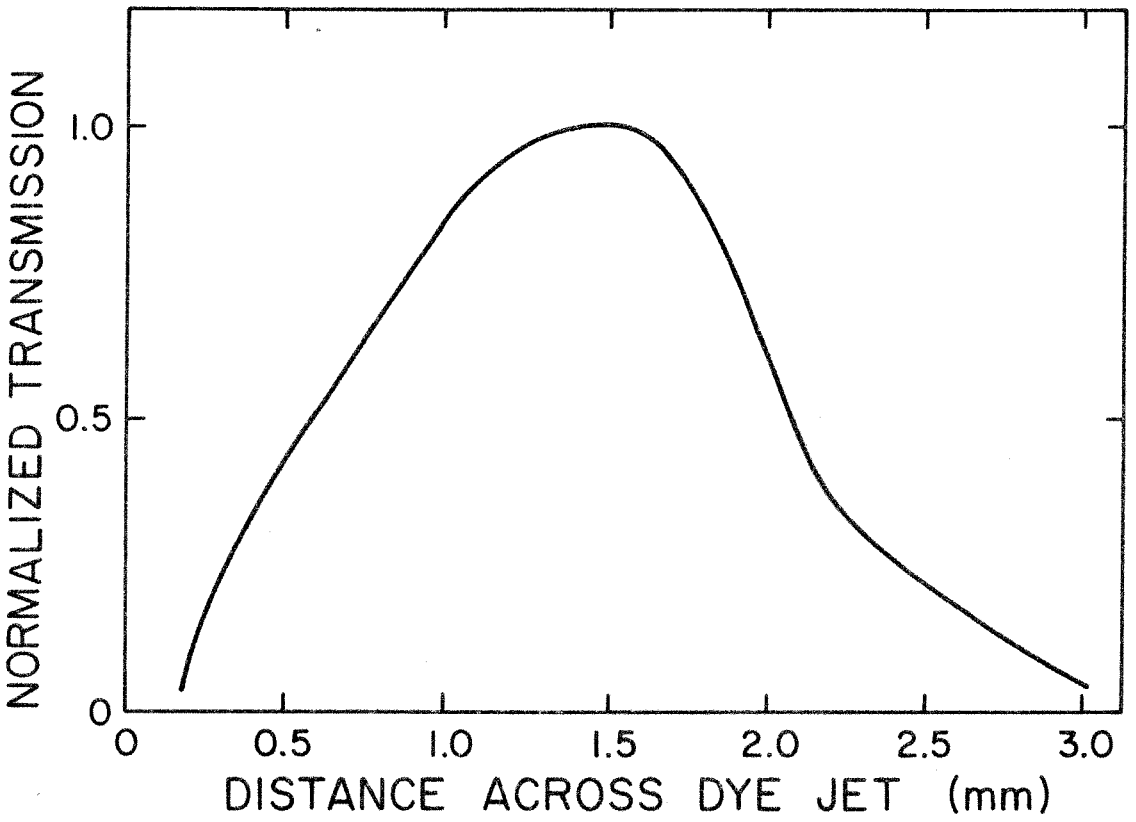

Fig. 2.3.1 Transmission of a focused argon laser beam (λ=5145Å) through the rhodamine 6G gain jet.

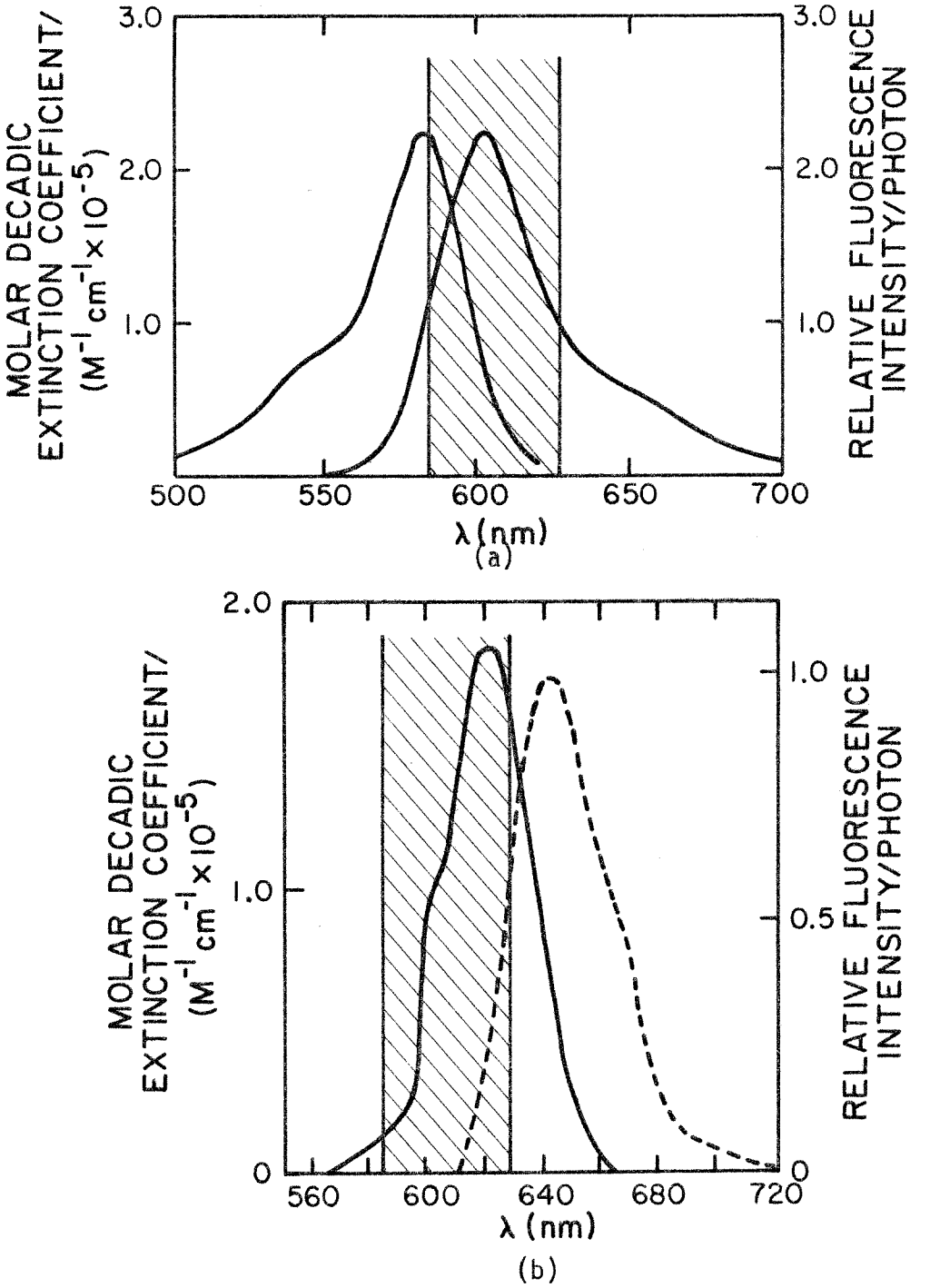

Fig. 2.4.1 Absorption and fluorescence spectra of (a) normal DODCI and (b) its photoisomer [15].

power picosecond pulses.

When mode locking the laser with DODCI only, the pump power is kept near threshold in order to have only a small population inversion at the gain medium (see Section 2.1). Mixing the solution with malachite green permits short pulse operation well above threshold [3]. The recovery time of malachite green is 2 ps [21]; however, by itself, it has not produced stable mode locking [3]. Figure 2.4.2 shows the absorption spectrum of a typical mixture of DODCI + malachite green [22]. The units are of decadic absorption coefficient, i.e., $A = \varepsilon_d M \equiv \frac{1}{L} \log_{10} I_{in}/I_{tr}$, where M is the molar concentration, L is the cell thickness, I_{in} and I_{tr} are the incident and transmitted intensities, respectively, and ε_d is defined by this relation to be the decadic extinction coefficient.

In Table I, features of the absorbing dyes in the laser are summarized. The molar concentration corresponds to the absorption spectrum of Figure 2.4.2. The decadic extinction at 6100Å coefficient is calculated from separate absorption spectra of DODCI and malachite green. In calculating the saturation intensities and energies, each absorber is assumed to be independent of the others, including the photoisomer of the DODCI, the concentration of which is taken to be 1/10 of the normal state of the dye [15]. The interaction volume used is $0.025 \times \pi \times (5 \times 10^{-4})^2 cm^3$. Note that under mode locking conditions a saturation energy rather than a saturation intensity is defined, as the pulses are much shorter than in the excited state

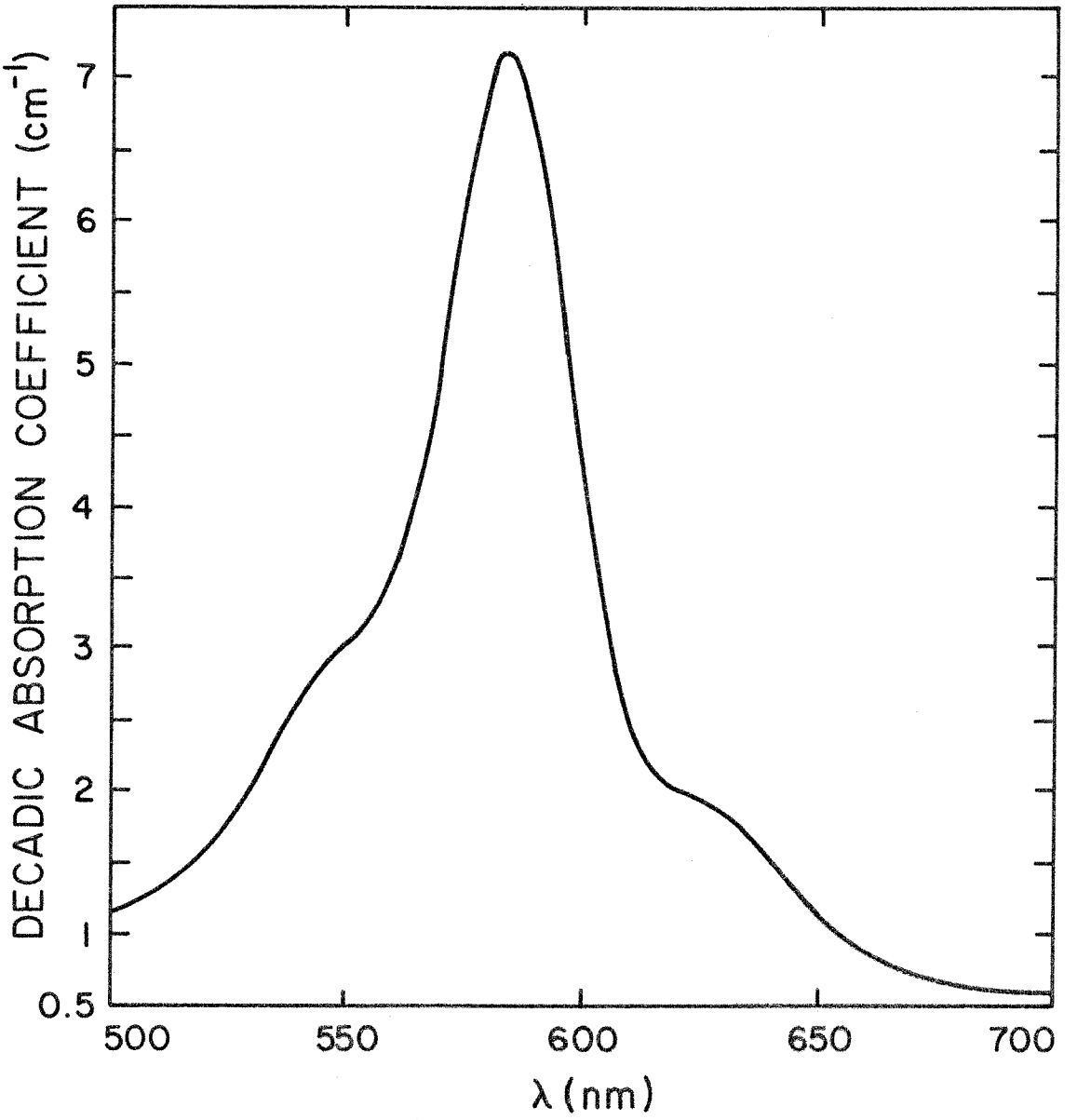

Fig. 2.4.2 Absorption spectrum of a typical mixture of DODCI and malachite green, used to mode lock the dye laser.

lifetime. The saturation energies in Table I are lower than the cavity energy of the picosecond pulses, which is (3-10) x 10^{-9}J.

TABLE I

	DODCI	Malachite Green
Molecular weight	486.35 [23]	330.48 [24]
Excited-state lifetime	1.2 nsec [15,17,18]	2 psec [21]
Molar concentration	3.6×10^{-5}M	2.7×10^{-5}M
Decadic extinction coefficient @ 6100Å	norm.(a) $0.3 \times 10^{5}M^{-1}cm^{-1}$ ph.is.(a) 1.3×10 $M^{-1}cm^{-1}$ [15]	$0.4 \times 10^{5}M^{-1}cm^{-1}$
Saturation intensity @ 6100Å	norm. 1.2×10^{6} W/cm^2 ph.is.(b) 2.7×10^{5} W/cm^2	5.1×10^{8} W/cm^2
Saturation energy @ 6100Å	norm. 1.2×10^{-9}J ph.is.(b) 2.6×10^{-10} J	8.5×10^{-10}J

(a) norm = normal; ph.is.= photoisomer

(b) Assuming quantum efficiency for photoisomer formation = 10% [15].

2.5 Basic Configuration of the Passively Mode Locked CW Dye Laser

The basic configuration of the passively mode locked CW dye laser was shown schematically in Figure 2.1.1. A folded cavity configuration operated by us is shown in Figure 2.5.1. The gain medium

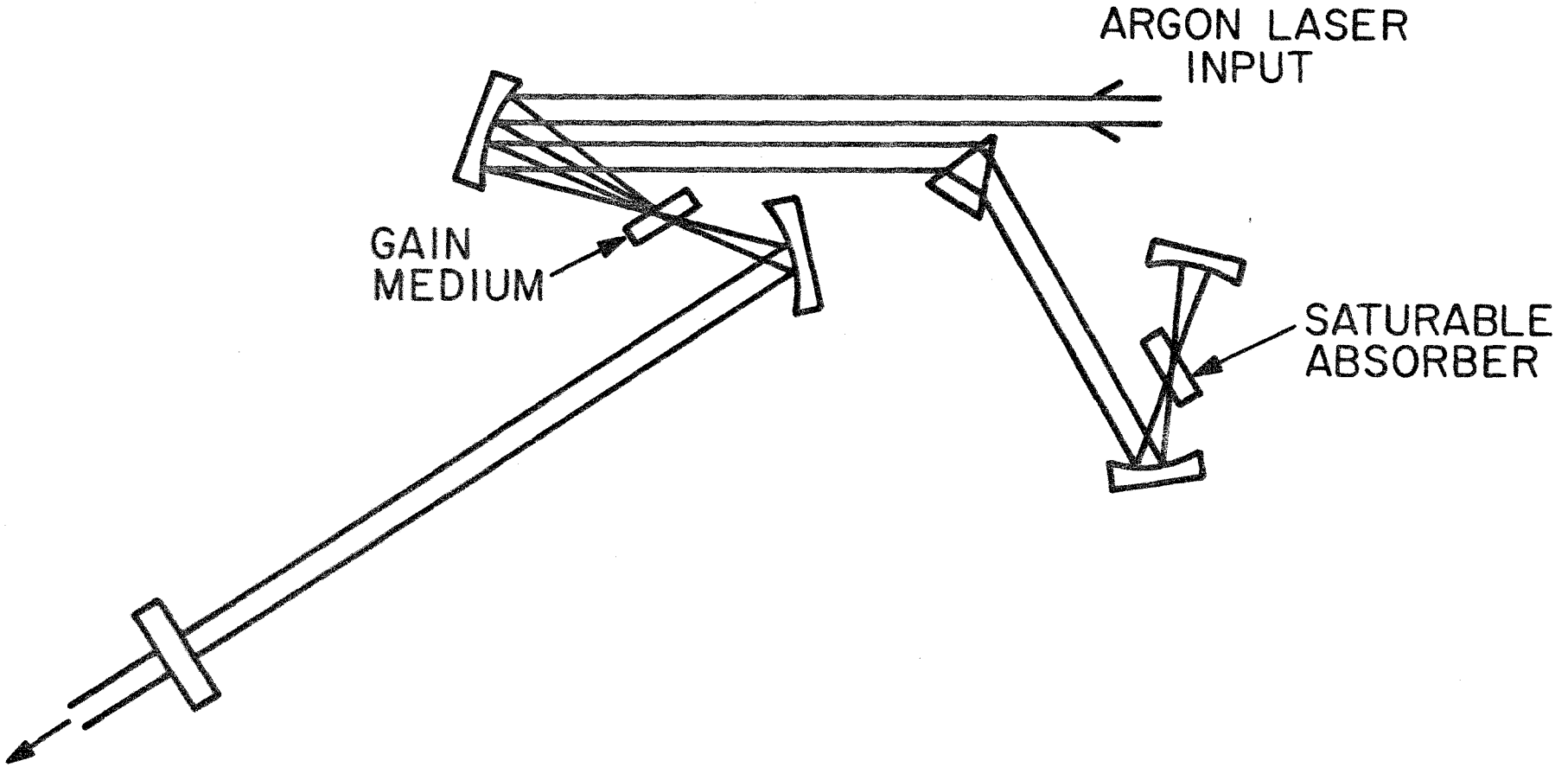

Fig. 2.5.1 A schematic diagram of the folded cavity passively mode locked CW dye laser

is shifted from the center of the cavity to the side opposite the saturable absorber. As a result, the amplifier recovery will be more complete for pulses arriving from the absorber than it will for pulses arriving from the other end. The cavity length is ∿162.5 cm, so that the round trip time is ∿10.8 nsec, slightly more than twice the recovery time of the rhodamine 6G. The mirrors' radii of curvature are 10 cm at the gain arm and 5 cm at the absorber arm. The output coupling mirror is flat and its transmission is 2% or less. All other mirrors are dielectric coated to have high reflectivity in the band 4500-6500Å, and all are mounted in mounts with angular resolution of 0.1 mrad [25]. In each arm one of the mirror mounts is mounted on a translation stage.

The circulating systems of both media are identical. One is schematically drawn in Figure 2.5.2. The dye pumps are miniature hydraulic pumps. The pore size of the filters is 0.8 μm [27]. The role of the shock cushion [28] is to reduce the vibrations of the flowing dye. The nozzle was purchased from Coherent Radiation [14] and assembled in a holder which allows smooth rotation around the center line of the jet. The holder is mounted on an x-y-z micropositioner which controls the jet position with a resolution better than 25 μm. The dye solutions flow at a rate of ∿12m/sec (∿ 7.4 cm^3/sec). The circulating system is designed so that it can be drained by the pump when the motor rotates forward. It adds convenience, saves labor, and reduces contamination.

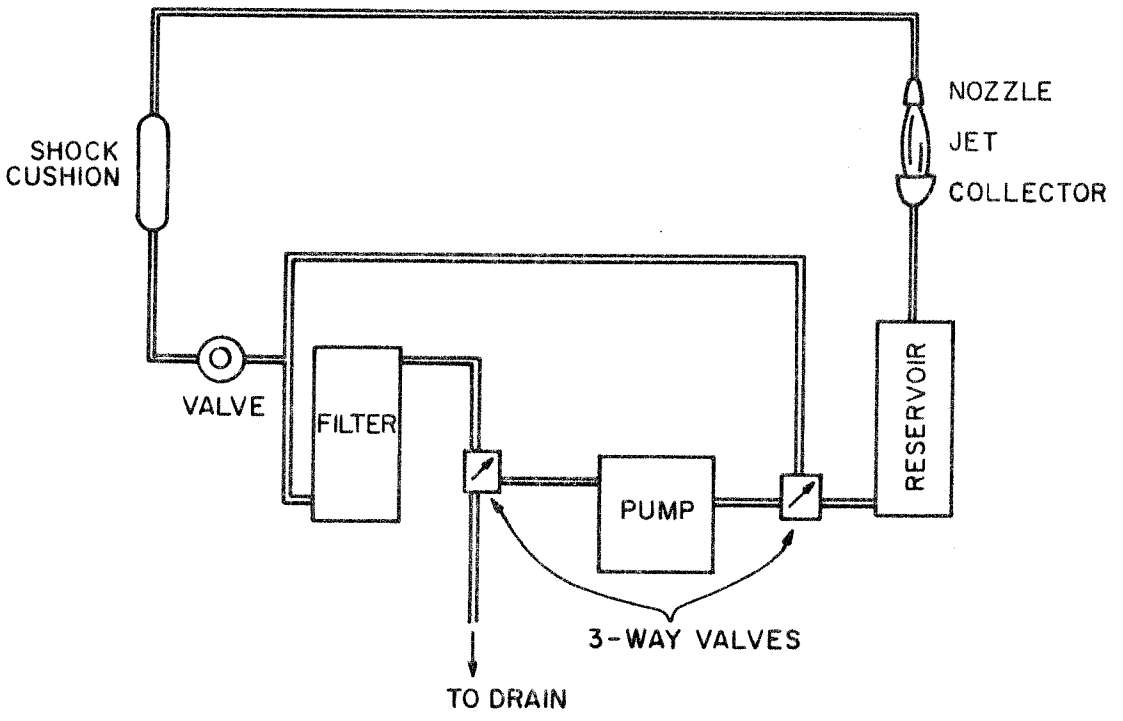

Fig. 2.5.2 The dye solution circulating system.

The prism is the tuning element of the laser. Its role is to force the laser to operate at ∿6100Å rather than at short wavelengths ($\lambda < 5100$Å), where the DODCI absorbs less and the rhodamine 6G amplification is higher. It is a full Littrow prism with an apex angle of 69° so that the 6100Å dye laser beam is incident at a Brewster angle from both directions.

The argon-ion laser beam is focused on the gain jet by one of the 10 cm radius of curvature internal mirrors. Its spot size is 50 μm while the spot size of the dye laser beam is ∿42 μm on the gain jet and ∿27 μm on the absorber jet.

The laser system described in this section is capable of generating a continuous train of picosecond pulses such as those shown in Figure 5.1.3. However, the output power is quite low: 50-100W peak power. The modification of the laser, so that it will emit more powerful pulses, is described in the next two sections.

2.6 Increasing the Output Power of the Laser: The Dumper

The saturable absorber adds loss to the cavity. To lower the overall loss, and thus to improve the cavity Q-factor, the transmission of the output mirror must be low, typically 2% or less. As a result, only a small fraction of the cavity energy is coupled out.

To increase the output power, all the mirrors are coated to high reflectivity and an acoustooptic modulator, made of fused silica crystal and a transducer, switches the beam out of the cavity by Bragg diffraction whenever it is energized by an rf wave. For physical details see, for example, Ref. [29a].

An acoustooptic output coupler Model 365 was purchased from Spectra Physics [30]. The medium is a block of fused silica (4.8 x 4 x 4.8 mm). A thin film transducer is sputtered on the bottom surface, and acoustic power up to 16 MW/cm^2 can be delivered. The transducer is driven by Model 465 modulator driver by Spectra Physics [30], which is an externally triggered rf pulser with 5 nsec rise time. The rf frequency is fixed to 470 MHz.

To achieve a short overall rise time, the acoustic wave should traverse quickly across the optical beam. Consequently, the dye laser beam must be focused down to a waist diameter of

$$2w_o = v_s t_r \tag{2.6.1}$$

For t_r = 5 nsec and $v_s = 5.95 \times 10^5$ cm/sec [29b], (2.6.1) implies $2w_o = 30$ μm. To focus the beam, the flat end mirror of Figure 2.5.1 is replaced by a folding curved mirror (R = 20 cm) and an end curved mirror (R = 10 cm). Figure 2.6.1 shows the "dumper arm." P is the primary diffracted beam, and S is the secondary. If the diffraction efficiency of the primary beam is η, then the efficiency of the secondary beam is $(1-\eta)\eta$. Therefore, while in principle the primary beam can contain 100% of the cavity pulse, the secondary can have at most 25% of it. The diffraction efficiency is given by [29a]

$$\eta = \frac{I_d}{I_i} = \sin^2\left(\frac{\pi \ell}{\lambda\sqrt{2}} \sqrt{M I_a}\right) \tag{2.6.2}$$

in which ℓ is the interaction length, M is an acoustooptic figure of merit, and I_a is the intensity of the acoustic wave in watts/m^2.

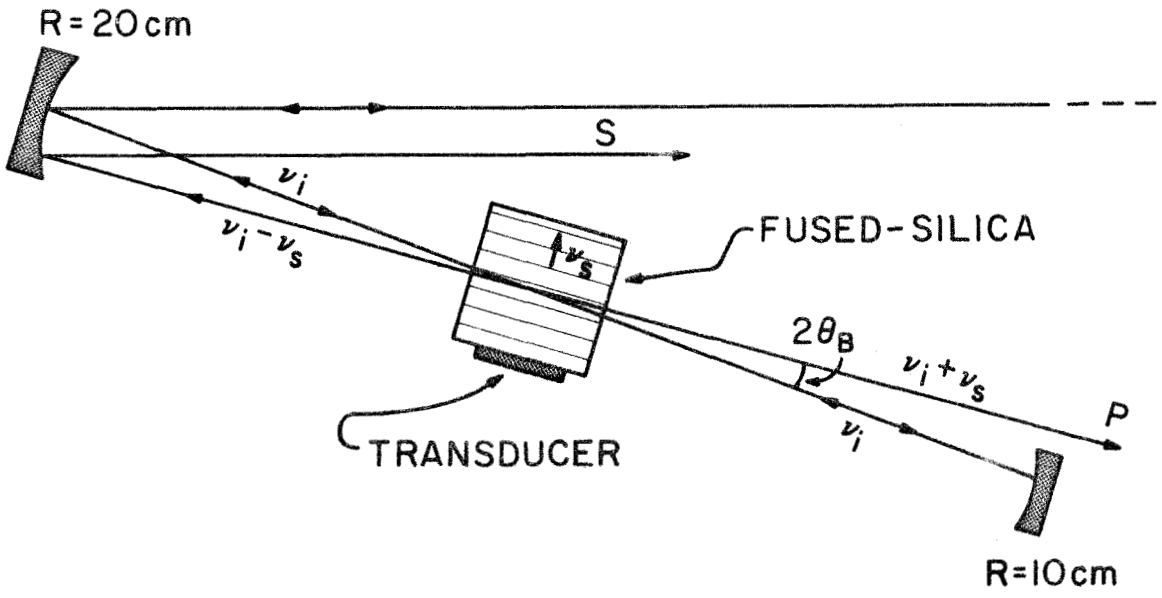

Fig. 2.6.1 The dumper arm. P is the primary beam extracted from the cavity, S is the secondary one (see text).

For $M = 1.51 \times 10^{-15}$ MKS and $n = 1.46$ [29b], equation (2.6.2) predicts maximum efficiency of 98%, but in practice it has been measured to be $\sim$ 30% in the lowest order of diffraction.

When a cavity dumper is operated in a passively mode locked dye laser, the process of extracting energy perturbs the steady state of the laser system. As a result, some time is required to restore the power and pulse duration to their steady state values (see Section 2.1). Consequently, the following requirements are imposed upon the dumper:
1) It must have a rise time shorter than the cavity round trip time (to operate at maximum diffraction efficiency).
2) The dumper should not be activated for longer than twice the cavity round trip time (to enable dumping of a single pulse at a time.)
3) Pulses should be dumped at a rate which allows the system to recover. The randomness inherent in the passively mode locked dye laser (see Section 2.1) and the perturbation by the dumper result in a train of pulses which are not perfectly periodic. This imposes a fourth requirement:
4) Activation of the dumper must be synchronized with the cavity pulses.

To meet these requirements, the synchronizing loop of Figure 2.6.2 has been devised. A fast detector [31] samples the pulses as they are weakly reflected from the prism. The resulting current pulses are amplified and activate a counter [32]. Every 2048 ($=2^{11}$) counts, which are equivalent to $\sim$22 μsec, a voltage pulse generator is triggered. The delay between the trigger and the generator output pulse can be controlled as well as the pulse height and width. This voltage pulse activates the driver and gates its rf output, as seen in Figure 2.6.3. The

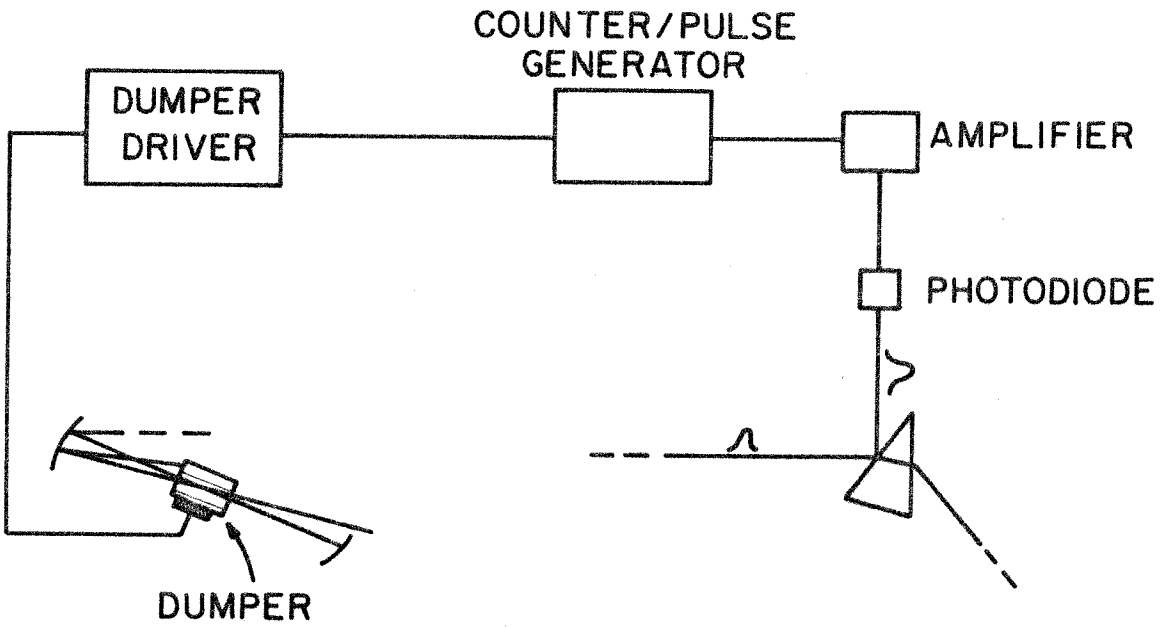

Fig. 2.6.2 The dumper synchronizing loop.

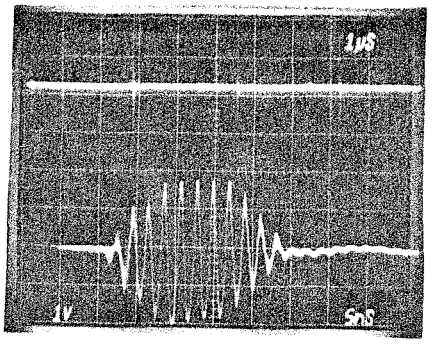

Fig. 2.6.3 The amplitude-modulated rf voltage of the dumper driver.

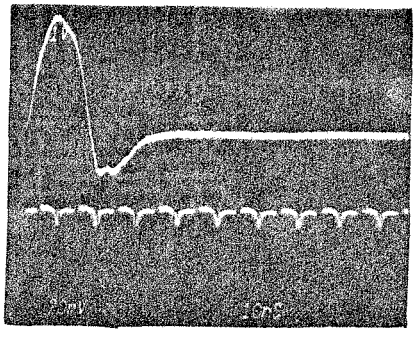

Fig. 2.6.4 The duration of the shortest activation pulse compared to the cavity round trip time of the picosecond pulse.

shortest activating pulse is of ∿16 nsec FWHM, but is more than 20 nsec wide at its bottom (its rise time is ∿4 nsec), as seen in Figure 2.6.4. As a result, when delayed for optimum efficiency, there are still remnants of the two pulses adjacent to the main one (see Figure 2.7.2).

2.7 The Passively Mode Locked CW Dye Laser with a Dumper

The configuration of the passively mode locked dye laser with the dumper is drawn schematically in Figure 2.7.1. This is the laser system which has been used for the experiments which are described in the second part of this thesis.

Oscilloscope displays of the dumped pulse and of the cavity energy (sampled from reflection at the prism) are shown in Figures 2.7.2 and 2.7.3, respectively. Notice the remnant of the pulses adjacent to the main dumped pulse (Figure 2.7.2) and the system recovery time (Figure 2.7.3). This laser emits 1-4 kW pulses of duration 1-2 psec at a repetition rate of $\sim 4.5 \times 10^4$ pps. The wavelength of the pulses is 6100-6150Å, the pulses are chirped, and it is possible to compress them to a width of ∿0.3 psec [3].

In the following chapters the laser resonator, picosecond pulse width measurements, and the alignment of the system will be discussed.

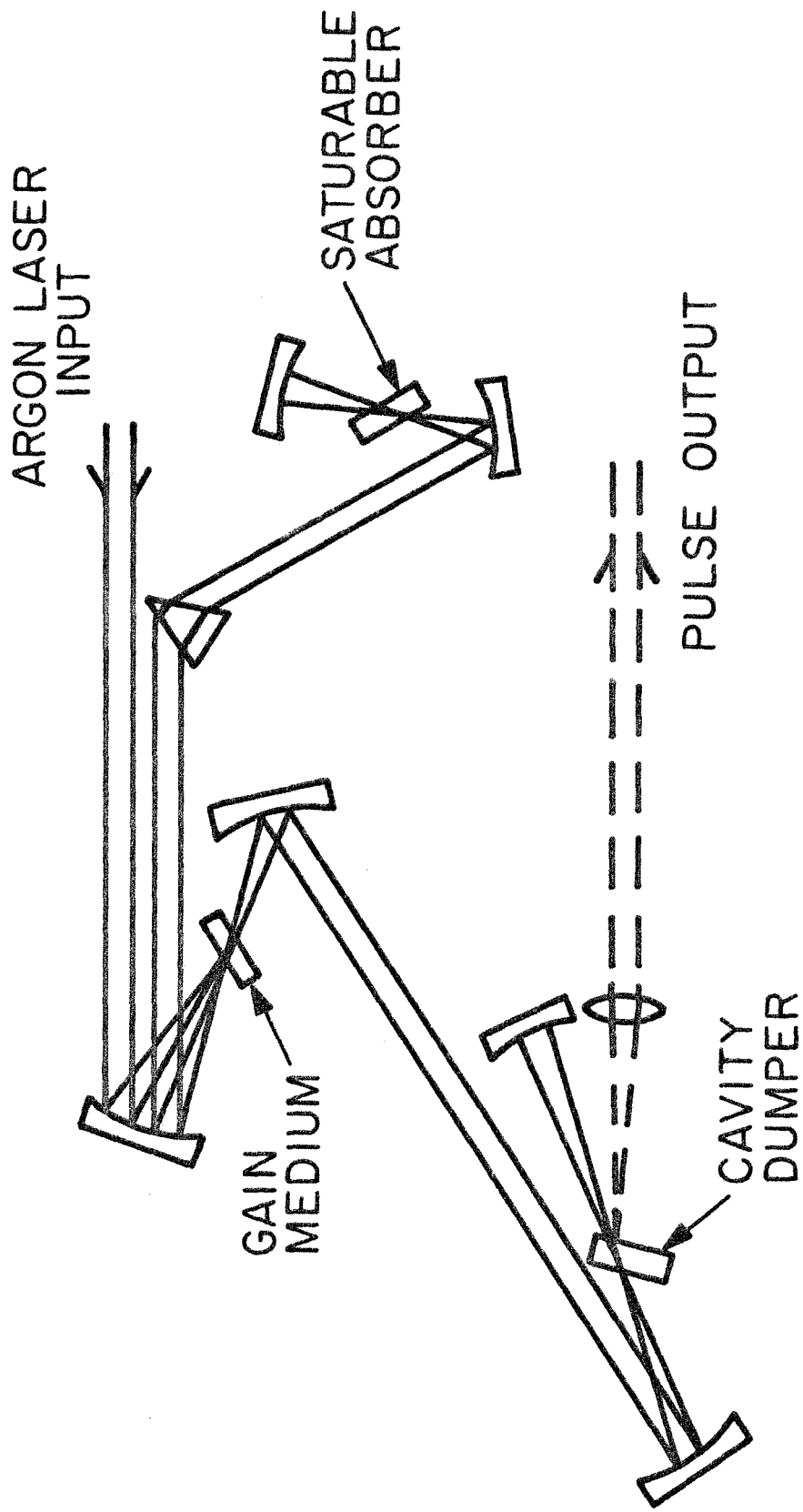

Fig. 2.7.1 A schematic diagram of the passively mode locked CW dye laser with a dumper

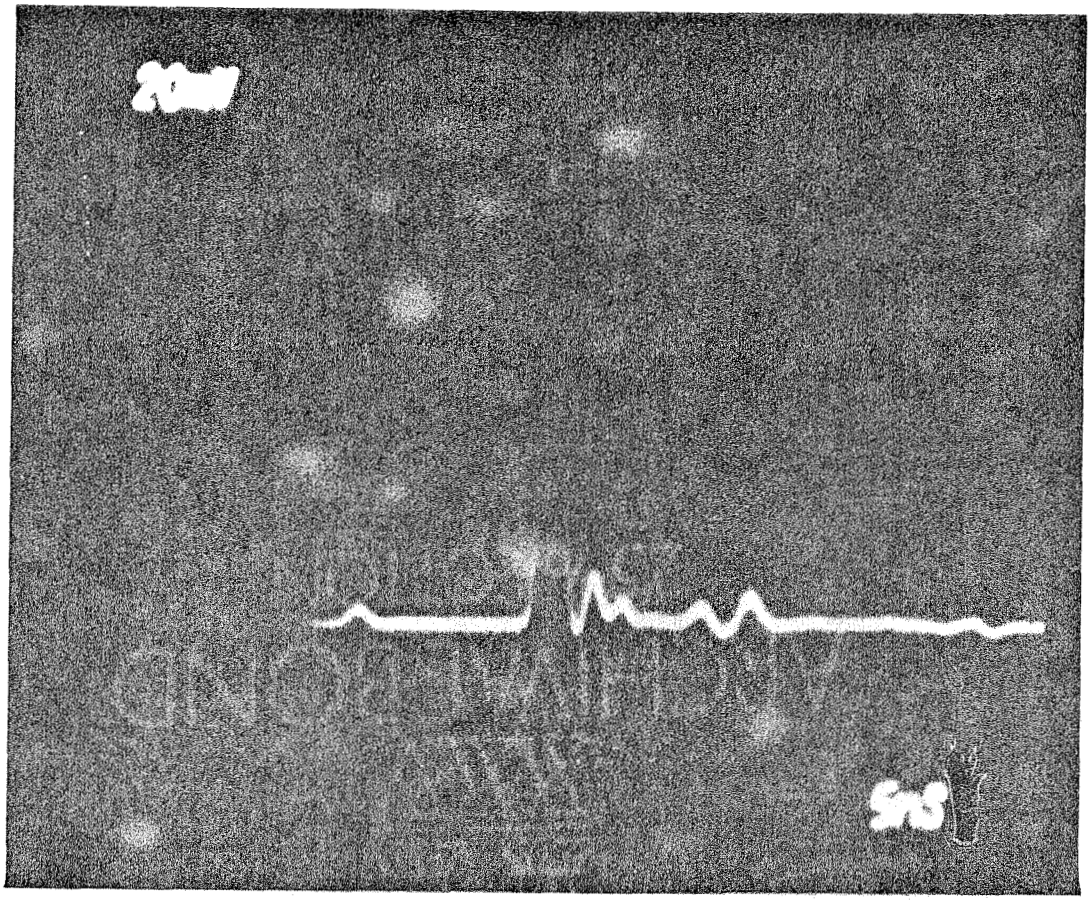

Fig. 2.7.2 A detector-limited display of the dumped picosecond pulse. Note the remnants of the previous and the following pulses (±10 ns from the main pulse). Pulse energy is several nanojoules.

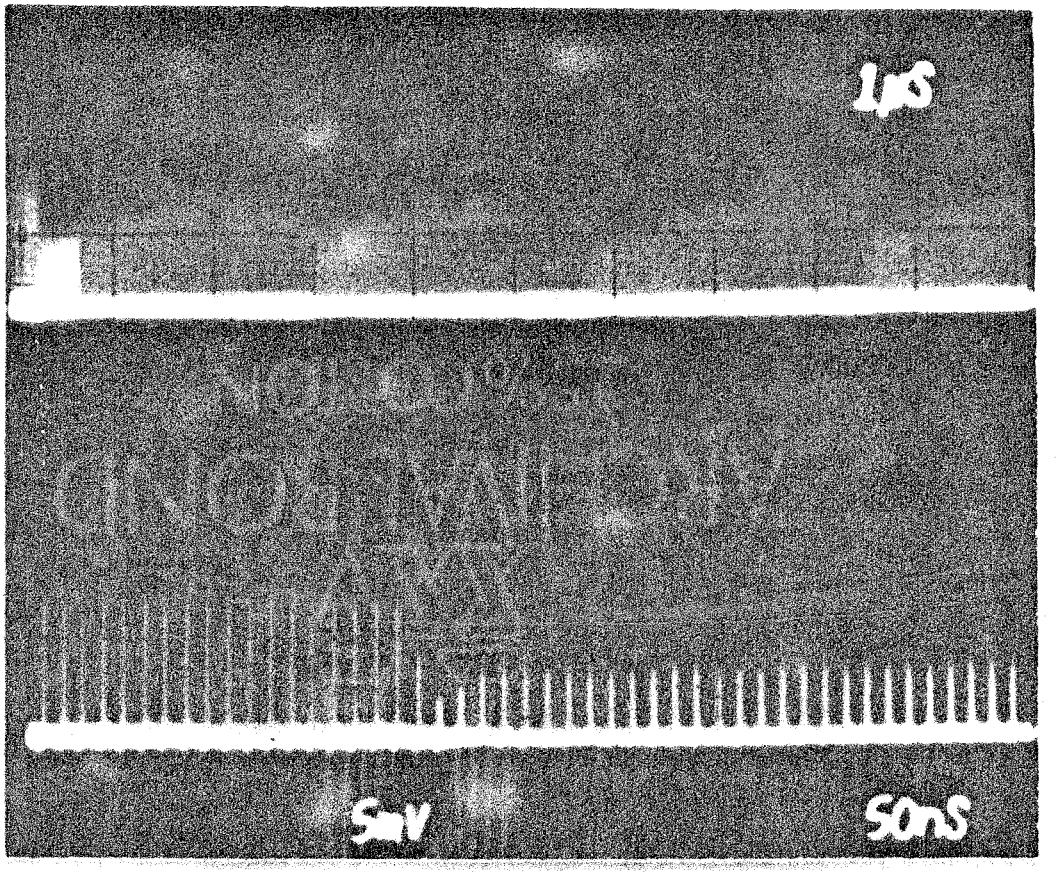

Fig. 2.7.3 The cavity energy of a dumped laser. The lower trace shows the individual pulses. Coupling efficiency is seen to be ∿40%. The upper trace shows the system recovery time. To ensure full recovery, the repetition rate was reduced from that shown in the figure to $\sim 4 \times 10^4$pps.

Chapter 3

MULTI-ELEMENT RESONATORS FOR FREE-RUNNING AND MODE LOCKED CW DYE LASERS

3.0 Introduction

There are certain dimensional constraints imposed on an optical resonator if it is to support low loss laser modes [33]. A resonator which satisfies these conditions is commonly referred to as stable. The stability requirement is complicated in our system, since it employs two end-mirrors which form the resonator, four focusing optical elements (lenses or mirrors), two flowing jets, a fused-silica block (the dumper), and a prism. The understanding of the effect of all these components on the stability of the resonator and on the beam parameters in it, i.e., the size and location of the beam waists, is very important for a correct design and a proper alignment procedure of the multi-element laser.

This problem is addressed in this chapter. It starts by preparing the mathematical tools used in resonator analysis. Then a cavity with only one internal lens is studied. The compensation of the astigmatism which is introduced by tilted components in this cavity, such as a dye cell, is also discussed. The analysis of this simple cavity not only clarifies analytically the numerical investigation of the multi-mirror cavity, but also formulates a design of a CW dye laser which is optimal in terms of power stability and best collimated output beam. Next,

the cavity of the passively mode locked dye laser with a dumper is analyzed.

3.1 Characterization of Gaussian Beams

Unlike the mathematically defined plane waves, optical beams are confined in space. The spatial and temporal distribution of the beam energy can be found by solving Maxwell equations in the proper medium. This solution will be reviewed briefly here so as to define the various parameters involved in the calculations which follow. Detailed solutions can be found in many textbooks. The discussion here follows Yariv [29c].

Maxwell equations in an isotropic charge-free medium are

$$\vec{\nabla} \times \vec{E} = -\mu \frac{\partial \vec{H}}{\partial t}$$

$$\vec{\nabla} \times \vec{H} = \varepsilon \frac{\partial \vec{E}}{\partial t}$$

$$\nabla \cdot (\varepsilon \vec{E}) = 0 \qquad (3.1.1)$$

Assume a harmonic field

$$\vec{E}(x,y,z,t) = \mathrm{Re}[\vec{E}(x,y,z)e^{i\omega t}] \qquad (3.1.2)$$

Then

$$\nabla^2 \vec{E} + k^2(r)\ \vec{E} = 0 \qquad (3.1.3)$$

in which

$$k^2(r) = \omega^2 \mu \varepsilon(r)[1 - i\sigma(r)/\omega\varepsilon] \qquad (3.1.4)$$

In a homogeneous medium, k is independent of r. Defining the propagation direction to be z, we can define a function $\psi(x,y,z)$ by

$$E(x,y,z) = \psi(x,y,z)e^{-ikz} \tag{3.1.5}$$

Assuming $k \frac{\partial}{\partial z}\psi >> \frac{\partial^2}{\partial z^2}\psi << k^2$, (3.1.3) becomes

$$\nabla_t^2 \psi - 2ik \frac{\partial \psi}{\partial z} = 0 \tag{3.1.6}$$

where $\nabla_t^2 \equiv \frac{\partial^2}{\partial x^2} + \frac{\partial^2}{\partial y^2}$. Transforming to cylindrical coordinates (r,ϕ,z) in which $r = \sqrt{x^2 + y^2}$, ∇_t^2 becomes

$$\nabla_t^2 \psi = \frac{1}{r}\frac{\partial}{\partial r}\left(r \frac{\partial \psi}{\partial r}\right) + \frac{1}{r^2}\frac{\partial^2 \psi}{\partial \phi^2} \tag{3.1.7}$$

The most fundamental solution is found when no azimuthal variation of ψ is assumed, i.e., $\partial\psi/\partial\phi = 0$. In this case (3.1.6) is solved to give

$$E(x,y,z) = E_o \frac{w_o}{w(z)} \exp\left\{-i[kz - \eta(z)] - i \frac{kr^2}{2q(z)}\right\} \tag{3.1.8}$$

where

$$\frac{1}{q(z)} \equiv \frac{1}{R(z)} - i \frac{\lambda}{\pi n w^2(z)} \tag{3.1.9}$$

in which, by defining

$$z_o \equiv \frac{n\pi w_o^2}{\lambda} \tag{3.1.10}$$

the parameters are defined by

$$w^2(z) \equiv w_o^2\left(1 + \frac{z^2}{z_o^2}\right) \tag{3.1.11}$$

$$R(z) \equiv z\left(1 + \frac{z_o^2}{z^2}\right) \tag{3.1.12}$$

and

$$\eta(z) = \tan^{-1} \frac{z}{z_0} \tag{3.1.13}$$

It is easy to see that the electric field (the real part of (3.1.8) has a Gaussian distribution, and it falls to its 1/e peak value at a distance $r = w(z)$ from the optical axis. The minimum of $w(z)$, w_0, occurs at the so-called "waist of the beam," which, in the calculations above, was taken to be at $z = 0$. At the waist $R(0) = \infty$, and at $z^2 >> r^2$, $R(z)$ approaches the radius of curvature of a spherical wave. Accordingly, it is referred to as the "radius of curvature" of the beam. The confocal parameter, z_0, is a convenient variable (sometimes it is defined by $b = 2z_0$). Notice that if $z = z_0$, then $w^2(z_0) = 2w_0^2$, and $R(z_0) = 2z$.

The diffraction angle is given by

$$\tan \theta = \frac{w(z)}{z} \tag{3.1.14}$$

or, for $z >> z_0$ and $\lambda << w_0$,

$$\theta \simeq \frac{\lambda}{\pi w_0} \tag{3.1.15}$$

3.2 The ABCD Transfer Matrix and the Imaging Rules

When propagating a distance d through a homogeneous space, the complex beam parameter q, is transformed linearly

$$q(z+d) = q(z) + d \tag{3.2.1}$$

When passing through a thin lens, $w(z)$ is conserved, while the beam radius of curvature is transformed by

$$\frac{1}{R_{out}} = \frac{1}{R_{in}} - \frac{1}{f} \tag{3.2.2}$$

Therefore,

$$\frac{1}{q_{out}} = \frac{1}{q_{in}} - \frac{1}{f} \tag{3.2.3}$$

If q_{in} and q_{out} are measured at distances d_1 and d_2 from the lens, respectively, then by combining (3.2.1) and (3.2.3) we find

$$q_{out} = \frac{(1-d_2/f)q_{in} + (d_1+d_2-d_1d_2/f)}{-q_{in}/f + (1-d_1/f)} \equiv \frac{Aq_{in} + B}{Cq_{in} + D} \tag{3.2.4}$$

The constants A,B,C, and D are identical to the elements of a matrix which transforms the parameters of a paraxial ray when it passes through the same optical system [34],[33],[29c]:

$$\begin{bmatrix} r_{out} \\ r'_{out} \end{bmatrix} = \begin{bmatrix} A & B \\ C & D \end{bmatrix} \begin{bmatrix} r_{in} \\ r'_{in} \end{bmatrix} \tag{3.2.5}$$

where r is the ray distance from the optic axis and r' is its slope with respect to this axis.

This identification of A,B,C, and D as matrix elements is very helpful in tracing a Gaussian beam when propagating through a series of complex lens-like media, as the ABCD matrix of the system can be found by sequential multiplication of the ray matrices of the subsystem units.

An important application of the ABCD matrix is found in calculating the complex parameter of a beam in an empty resonator: If we trace the beam along a round-trip of the cavity, its complex parameter, q, should be self-consistent, regardless of the plane at which we started the tracing. If we denote by z the coordinate along the cavity and substitute $q = q_{in} = q_{out}$ in equation (3.2.4), we find

$$\frac{1}{q(z)} = \frac{D-A}{2B} \pm \frac{i}{2B}\sqrt{4-(A+D)^2} \tag{3.2.6}$$

so that

$$R(z) = \frac{2B}{D-A} \tag{3.2.7}$$

and

$$\frac{\pi w^2(z)}{\lambda} = \frac{2|B|}{\sqrt{4-(A+D)^2}} \tag{3.2.8}$$

Clearly, the resonator is stable only if

$$\frac{|A+D|}{2} < 1 \tag{3.2.9}$$

For example, assume an empty two-mirror resonator. It is easy to show that

$$\frac{A+D}{2} = \frac{2}{R_1R_2}d^2 - 2\left(\frac{1}{R_1}+\frac{1}{R_2}\right)d + 1 \tag{3.2.10}$$

in which R_1 and R_2 are the radii of curvature of the mirrors, defined positive when their centers of curvature are in the direction of each other, and d is the spacing between them.

The parabola (3.2.10) is plotted in Figure 3.2.1. The heavy line is the region where the inequality of (3.2.9) is satisfied. We will call it the "stability region." Thus, there are two stability regions:

$$\text{(a)} \qquad 0 < d < R_1$$

$$\text{(b)} \qquad R_2 < d < R_1 + R_2 \tag{3.2.11}$$

This example is far more general than it might seem to be. Any resonator with internal lenses can be mathematically transformed to an equivalent empty two-mirror resonator by employing the imaging rules

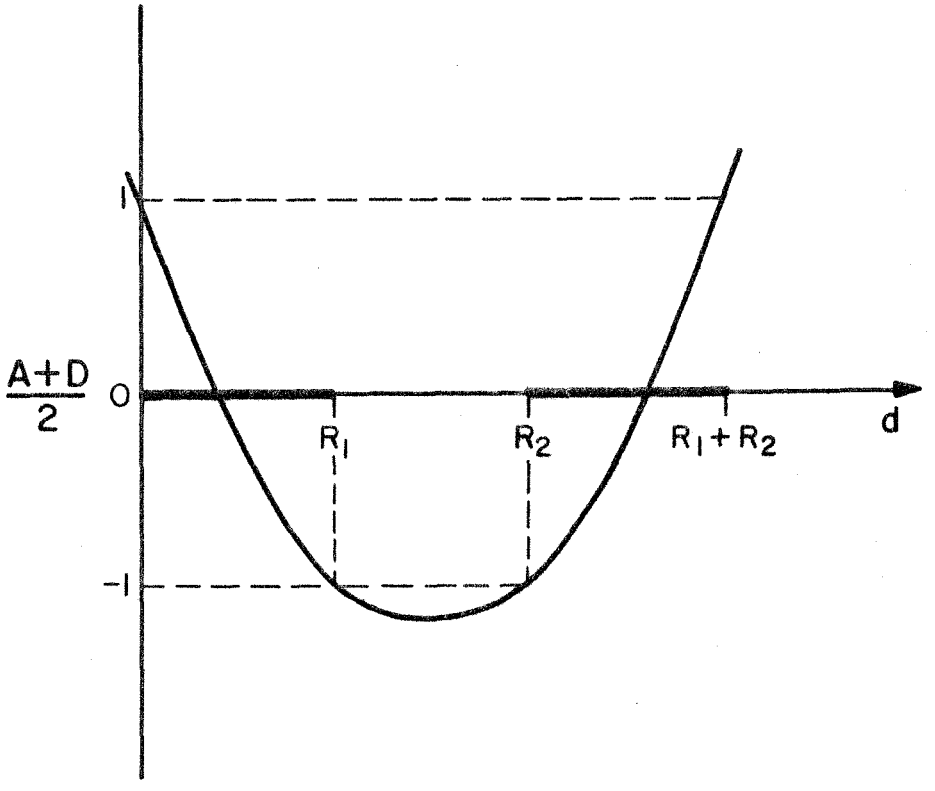

Fig. 3.2.1 A stability diagram for two mirror resonators. A+D is the ABCD matrix trace, d is the mirror spacing, and R_1 and R_2 are their radii of curvature. Stability regions are indicated by the heavy lines.

given by Kogelnik [33]. Referring to Figure 3.2.2, these rules state that the combination of the mirror R and the lens f can be replaced by a single equivalent mirror, the radius of curvature of which is given by

$$R' = \frac{Rf^2}{(d-f)(d-R-f)} \tag{3.2.12}$$

positioned at a distance

$$d' = \frac{df}{d-f} \tag{3.2.13}$$

away from the lens. The diameters of the two mirrors are related to each other by

$$\frac{a'}{a} = \frac{f}{f-d} \tag{3.2.14}$$

3.3 Resonators with an Internal Lens

Two-mirror resonators are not very stable when used for CW dye lasers. Consider the cavity of Figure 3.3.1. Using the beam parameters defined in Section 3.1, it is easy to show that

$$\frac{\delta w_o}{w_o} = \left(1 - \frac{L^2}{z_o^2}\right) \frac{\delta L}{4L} \tag{3.3.1}$$

where w_o is the radius of the beam at the flat mirror, z_o is the confocal parameter, and L is the mirror spacing. Assume typical values of these parameters: L = 20 cm (so that a tuning element can be inserted into the cavity), w_o = 10 μm, and λ = 6000Å, then

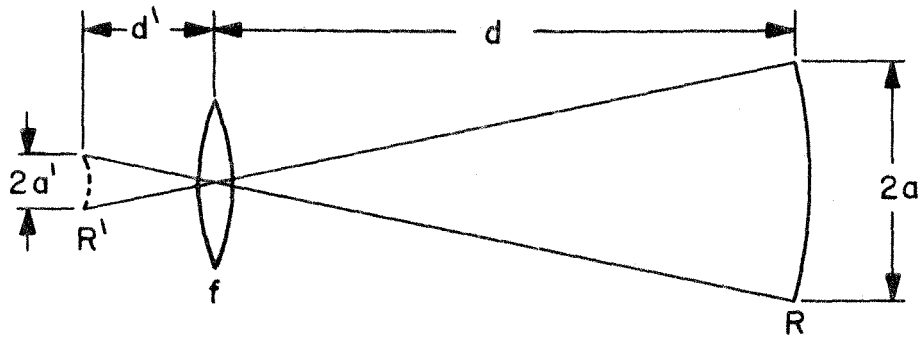

Fig. 3.2.2 Imaging of a mirror by a lens.

$$\frac{\delta w_o}{w_o} = -1.8 \times 10^3 \, \delta L \qquad (3.3.2)$$

If the mirrors vibrate or are misplaced by 10 μm

$$\left|\frac{\delta w_o}{w_o}\right| = 1.8 \qquad (3.3.3)$$

This stringent requirement on the mirror spacing is relieved when a focusing element is inserted in the cavity.

A resonator with an internal lens is shown in Figure 3.3.2. The beam parameters (i.e., the beam waists and their locations) are found by solving for the self-consistent complex beam parameter, q (see Section 3.2). Taking advantage of the imaging rules of the last section, straightforward round trip matrix multiplication is avoided by replacing the three-element cavity by an equivalent empty two-mirror resonator [35]. Various cavity configurations for CW dye lasers have been analyzed [35], [36]. A simple and convenient resonator is shown in Figure 3.3.3. Here, the output coupling mirror is flat and the beam spot size at the flowing dye is small (typically 20-40 μm in diameter). The stability regions and other beam parameters are easily found by applying the imaging rules to replace the lens and the flat mirror by an equivalent mirror. Nevertheless, an alternative approach is presented here which, although closely related to the imaging rules, allows a deeper insight into the properties of this type of cavity.

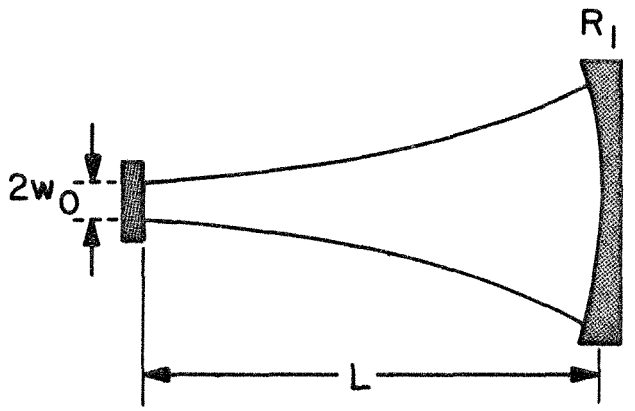

Fig. 3.3.1 Two mirror resonator for a CW dye laser.

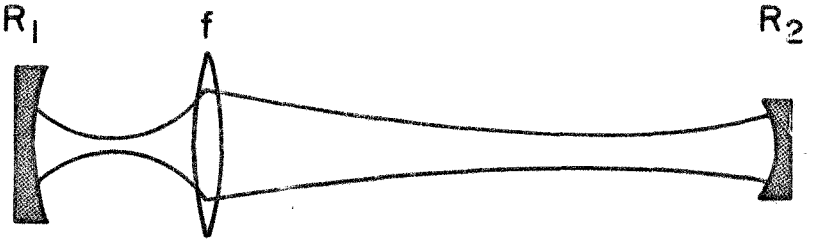

Fig. 3.3.2 A resonator with an internal lens.

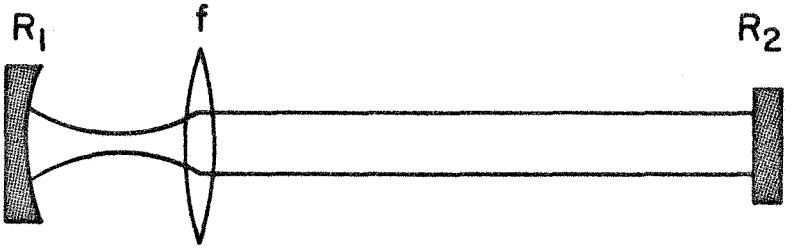

Fig. 3.3.3 A typical resonator for Cw dye lasers. This resonator is analyzed in Section 3.3.

Assume first a Gaussian beam with confocal parameter z_{10} and a waist at a distance ℓ_1 from a lens of focal length f (Figure 3.3.4). Rearranging (3.2.4), and recalling that the radius of curvature at a waist is infinite, we find that the waist beyond the lens will be at a distance

$$\ell_2 = \frac{f(\ell_1^2 - \ell_1 f + z_{10}^2)}{(f - \ell_1)^2 + z_{10}^2} \tag{3.3.4}$$

and its confocal parameter is

$$z_{20} = \frac{z_{10} f^2}{(f - \ell_1)^2 + z_{10}^2} \tag{3.3.5}$$

Assume that ℓ_2 is kept fixed. Then, the distance between the waist of the incident beam and the lens is given by

$$\ell_1 = \frac{-b \pm \sqrt{b^2 - 4c}}{2} \tag{3.3.6}$$

in which

$$b = \frac{f^2 - 2f\ell_2}{\ell_2 - f} \tag{3.3.7}$$

and

$$c = z_{10}^2 + \frac{f^2 \ell_2}{\ell_2 - f} \tag{3.3.8}$$

Similarly, we solve (3.3.4) for z_{10}:

$$z_{10}^2 = \frac{f\ell_1(\ell_1 - f) - \ell_2(f - \ell_1)^2}{\ell_2 - f} \tag{3.3.9}$$

The confocal parameter, z_{10}, is plotted in Figure 3.3.5 as a function of ℓ_1 for ℓ_2 = 150 cm and f = 2.5 cm. It is easy to show that the

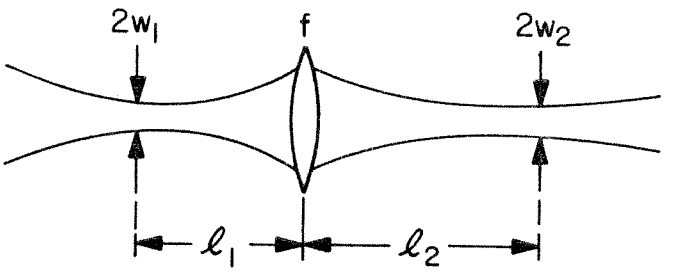

Fig. 3.3.4 A Gaussian beam focused by a thin lens.

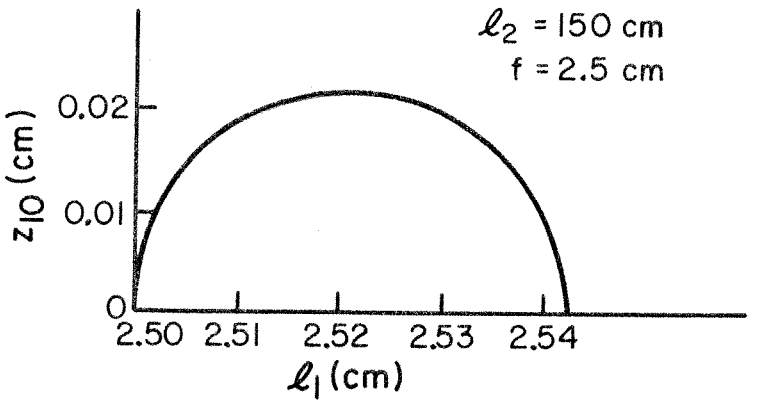

Fig. 3.3.5 The confocal parameter of an incident Gaussian beam as a function of its waist distance from a thin lens (f=2.5 cm), for an image waist distance of ℓ_2 = 150 cm.

maximum value of z_{10} is

$$\hat{z}_{10} = \frac{f^2}{2(\ell_2 - f)} \tag{3.3.10}$$

so that the optimum distance of the waist from the lens is

$$\hat{\ell}_1 = \frac{2f\ell_2 - f^2}{2(\ell_2 - f)} \tag{3.3.11}$$

which can be shown also to satisfy

$$\hat{\ell}_1 = f + \hat{z}_{10} \tag{3.3.12}$$

For ℓ_2 = constant, both z_{10} and ℓ_1 can change only within a certain range:

$$0 < z_{10} \leq \hat{z}_{10} \tag{3.3.13}$$

and

$$f \leq \ell_1 \leq f + 2\hat{z}_{10} = \hat{\ell}_1 + \hat{z}_{10} \tag{3.3.14}$$

We are ready now to design the resonator. To keep ℓ_2 fixed, R_2 is taken flat. This ensures that the resonator mode will have a waist there. The other end mirror, with a radius of curvature R_1, is set at a distance z from the waist at ℓ_1, so that (from (3.1.12))

$$R_1 = z + \frac{z_{10}^2}{z} \tag{3.3.15}$$

and we define

$$d_1 \equiv \ell_1 + z \tag{3.3.16}$$

to be the spacing between the R_1 mirror and the internal lens.

Typically, $z_{10}^2/R^2 << 1$ (for example, for $w_o = 20$ μm, $\lambda = 6000\text{Å}$, and $R = 5$ cm, $z_{10}^2/R^2 = 1.75 \times 10^{-3}$), therefore, z can be either

$$(a) \qquad z = R_1 - \frac{z_{10}^2}{R_1} \simeq R_1$$

or

$$(b) \qquad z = \frac{z_{10}^2}{R_1} \simeq 0 \tag{3.3.17}$$

We may, therefore, assume that if we position the mirror R_1 at a distance $d_1 = \ell_1 + R_1$ or at $d_1 = \ell_1$ from the lens, the mirror will not affect the beam parameters, and (3.3.6)-(3.3.14) will be valid in the short arm of the resonator. Consequently, the resonator's stability regions, one for each value of z (3.3.17), can be found from (3.3.14). However, positioning the mirror R_1 at a distance z_{10}^2/R_1 from the waist is impractical because there is not enough space for a dye cell. We will, therefore, consider only the second stability region, i.e.,

$$R_1 + f < d_1 < R_1 + f + 2\hat{z}_{10} \tag{3.3.18}$$

The stability range is now readily found to be

$$2s = 2\hat{z}_{10} = \frac{f^2}{(\ell_2 - f)} \tag{3.3.19}$$

It is obvious that in order to produce stable oscillations (in terms of output power) it is desirable to operate at $\ell_1 = \hat{\ell}_1$ where $z_{10} = \hat{z}_{10}$. It is possible to show from (3.3.5) and (3.3.12), that at that value of mirror spacing

$$\hat{z}_{20} = \frac{f^2}{2\hat{z}_{10}} = \ell_2 - f \tag{3.3.20}$$

This equation indicates the symmetric relation between the two arms of the cavity.

When the cavity is tuned to $\ell_1 = \hat{\ell}_1$, not only is the laser power most stable, but its output beam is the most collimated possible. To see this, (ℓ_2/f) is plotted in Figure 3.3.6 against (ℓ_1/f) for Gaussian (solid line) and geometric (dashed line) beams. The solid line is calculated from

$$1 = \frac{\ell_2}{f} = \frac{1 - \frac{\ell_1}{f}}{(1 - \frac{\ell_1}{f})^2 - (z_{10}/f)^2} \tag{3.3.21}$$

which is identical to (3.3.4), while the dashed line is calculated from

$$\frac{1}{(\ell_1/f)} + \frac{1}{(\ell_2/f)} = 1 \tag{3.3.22}$$

In this figure, $b_1 = 2z_{10}$. It is well known that a geometric beam, which suffers no diffraction, can be collimated by placing the source at the focal point. For that beam, as seen in the figure, $\ell_1 = f$ leads to $\ell_2 = \infty$. But a Gaussian beam is diffracted, and for $\ell_1 = f$, ℓ_2 is also equal to f. Further, ℓ_2 is always finite regardless of the value of ℓ_1. In other words, a Gaussian beam cannot really be collimated. The best "collimation" is achieved by maximizing ℓ_2. It can be seen from Figure 3.3.6 that this is done by positioning the waist of the incident beam at $\ell_1/f = 1 + b_1/2f = 1 + z_{10}/f$ or $\ell_1 = f + z_{10}$, which is exactly the relation between $\hat{\ell}_1$ and $\hat{z}_{10}$ given in (3.3.12). It is also evident from the figure that $(\ell_2)_{max} = f + f^2/2\hat{z}_{10}$, which from (3.3.20), identifies again $\ell_2 = (\ell_2)_{max}$ when $\ell_1 = \hat{\ell}_1$. Thus, when the cavity is adjusted to its most stable operation, its output beam is the most "collimated" possible. Its diameter D at the exit, i.e., immediately beyond the flat output coupling mirror, is easily found from (3.3.20) to be

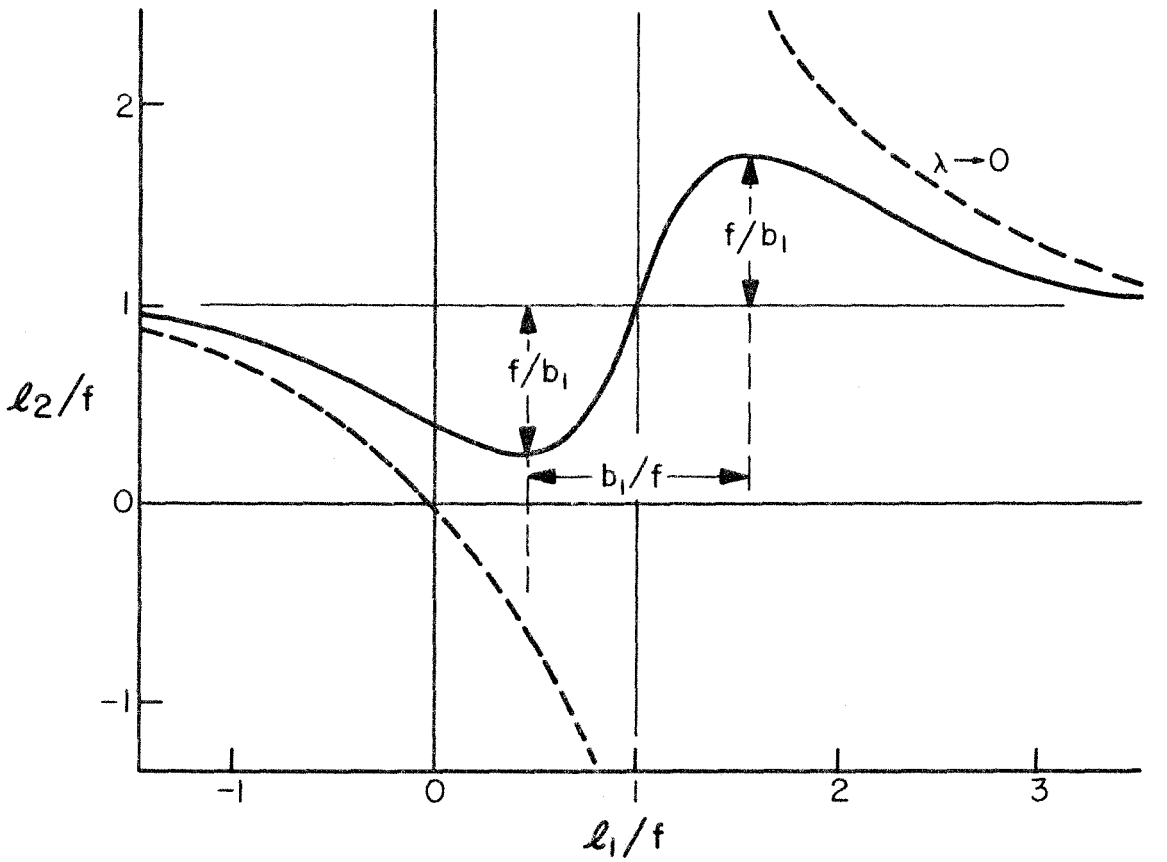

Fig. 3.3.6 The image waist-lens spacing (ℓ_2) as a function of the object waist-lens sapcing (ℓ_1), for Gaussian beams (solid line) and geometric rays (dashed line). $b_1=2z_{10}=2\pi w_{10}^2/\lambda$, where $2w_{10}$ is the object waist diameter.

$$D = 2\sqrt{\frac{\lambda(\ell_2 - f)}{\pi}} \tag{3.3.23}$$

To conclude, for stable operation of a resonator with an internal thin lens, the following simple relations hold: For given ℓ_2 and f, the confocal parameters are

$$\hat{z}_{10} = \frac{f^2}{2(\ell_2 - f)} \tag{3.3.24a}$$

and

$$\hat{z}_{20} = \ell_2 - f \tag{3.3.24b}$$

The optimum spacing between the lens and the curved mirror is

$$d_1 \simeq R_1 + \hat{\ell}_1 \tag{3.3.25}$$

where $\hat{\ell}_1$, which is given by

$$\hat{\ell}_1 = f + \hat{z}_{10} \tag{3.3.26}$$

is the optimum distance between the waist in the focusing arm and the lens. Finally, the stability range is

$$R_1 + f \leq d_1 \leq R_1 + f + 2\hat{z}_{10} \tag{3.3.27}$$

3.4 Astigmatically Compensated Three-Mirror Cavity

When the dye cell is inserted in the short arm of the three-element cavity described in the previous section, it is usually tilted at a Brewster angle so as to minimize reflection losses. It can be shown that when a Gaussian beam passes through a Brewster window, the window affects the rays in the plane parallel to the axis of rotation (called here the x-plane), and the rays in the plane perpendicular to it (the y-plane) differently ([35] and references therein). In the ray matrix formalism, this

can be expressed by two different effective distances, t_x and t_y which the rays, or the Gaussian beam, have to traverse.

The effective distances are

$$t_x = t \frac{\sqrt{n^2+1}}{n^2} \tag{3.4.1}$$

and

$$t_y = t \frac{\sqrt{n^2+1}}{n^4} \tag{3.4.2}$$

where t is the window thickness and n is its index of refraction.

This difference between the paths imparts astigmatic distortion to the beam. It also means that the effective length of the cavity is not the same in the x- and y-planes. Consequently, the stability regions in the two planes might not fully overlap, so that the stability region of the real cavity narrows down or, in the case of no overlap, does not exist at all.

It was shown by Kogelnik et al. [35] that maximum overlap of the x- and y-stability regions can be achieved by replacing the internal lens by a mirror tilted in an appropriate angle. Such a cavity is shown in Figure 3.4.1.

Referring to the notation in Figure 3.4.1, the effective focal lengths of the mirror in the x- and y-planes are [35]

$$f_x = f/\cos\theta \tag{3.4.3}$$

$$f_y = f \cos\theta \tag{3.4.4}$$

where $f = R_f/2$ and R_f is the radius of curvature of the folding mirror. Optimal overlap of the stability regions in the two planes can be

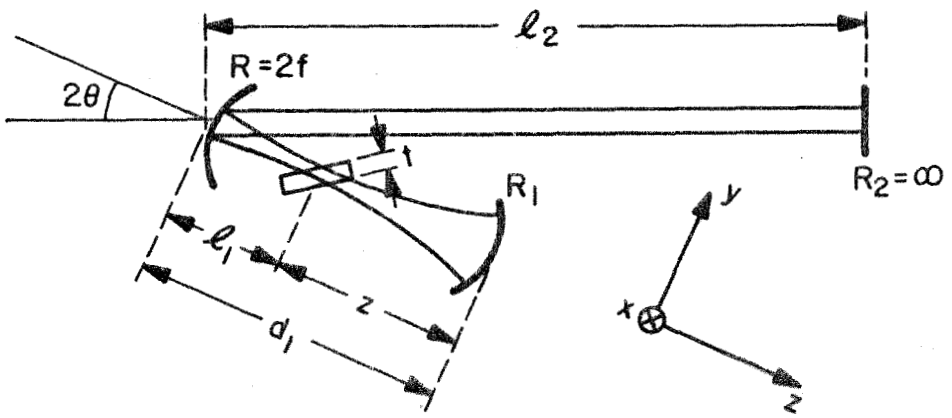

Fig. 3.4.1 A folded three mirror cavity.

achieved by requiring

$$d_{1x} - d_{1y} = t_x - t_y \tag{3.4.5}$$

where d_{1x} and d_{1y} are the optimum effective lengths of the short arm in the respective planes, shown in the previous section to be given by

$$d_{1x,y} = R_1 + f_{x,y} + \hat{z}_{10,x,y} \tag{3.4.6}$$

for one stability region of each plane, or by

$$d_{1x,y} = f_{x,y} + \hat{z}_{10,x,y} \tag{3.4.7}$$

for the other. For both regions (3.4.5) becomes

$$(f_x - f_y) + (\hat{z}_{10,x} - \hat{z}_{10,y}) = t_x - t_y \tag{3.4.8}$$

For small folding angles and $\ell_2 >> f$, $\hat{z}_{10,x} \simeq \hat{z}_{10,y}$. Therefore, (3.4.8) can be approximated to be

$$(f_x - f_y) \simeq t_x - t_y \tag{3.4.9}$$

which, from (3.4.1) - (3.4.4), becomes

$$2Nt = R_f \sin\theta \tan\theta \tag{3.4.10}$$

where

$$N = \frac{(n^2 - 1)\sqrt{n^2 + 1}}{n^4} \tag{3.4.11}$$

A result of the previous discussion is that both stability regions, specified by (3.4.6) and (3.4.7), are astigmatically compensated by a single angle θ. Note that although the stability regions overlap, there

are still some astigmatic differences that remain after compensation, such as the location of the waists [35].

Instead of a tilted mirror, the astigmatism can be compensated by a suitably tailored astigmatic lens. However, a mirror has an advantage over a lens, in that the lens adds reflection losses to the cavity.

3.5 Stability and Beam Parameters of the Resonator of the Passively Mode Locked CW Dye Laser with a Dumper

The cavity of the passively mode locked CW dye laser with a dumper, shown in Figure 2.7.1, is investigated here. The discussion will be confined to the dimensions, the radii of curvature of the mirrors, and the folding angles of the actual cavity used in our laser. After the initial alignment of the laser, the procedure for which will be described in Section 5.1, the laser is tuned to optimal operation by fine adjustments of the mirrors' positions and angular orientation. Accordingly, we will study here the cavity properties as functions of the length of only one of the arms, chosen to be the gain arm, while keeping all other cavity dimensions fixed.

Assume first the empty linear cavity of Figure 3.5.1, with the following mirror spacings: d_d = 20 cm, d_{dg} = 40 cm, d_{ga} = 85 cm, and d_a = 7.5 cm (for notations please refer to Figure 3.5.1). As in Section 3.2, a necessary condition for the cavity stability is $\left|\frac{A+D}{2}\right| < 1$, where A and D are the diagonal elements of the ray matrix of a cavity round trip. Therefore, we first plot $\left|\frac{A+D}{2}\right|$ as a function of the length of the gain arm, d_g. This is shown in Figure 3.5.2. The heavy lines indicate the stability regions, which are found to be

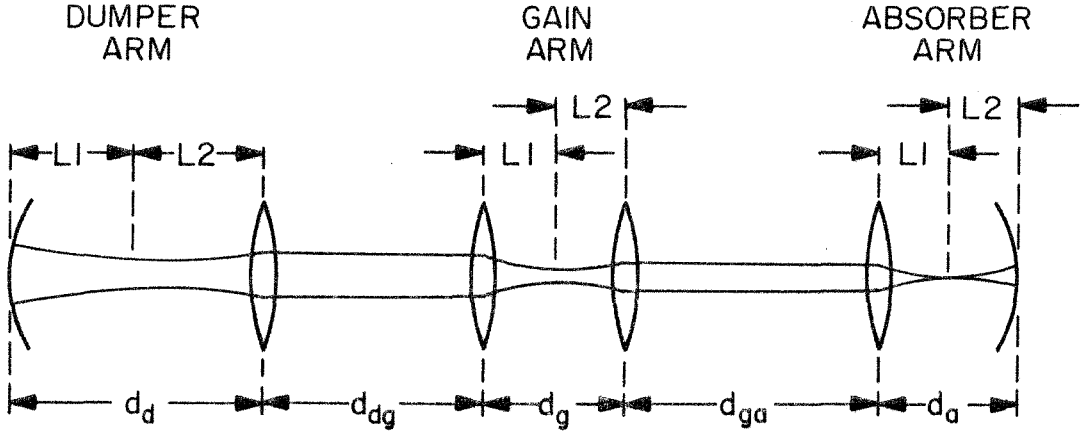

Fig. 3.5.1 A linear cavity for passively mode locked dye lasers with a dumper. Dimensions used in this section computations are: d_d = 20 cm, d_{dg} = 40 cm, d_{ga} = 85 cm, d_a = 7.5 cm, and d_g is variable.

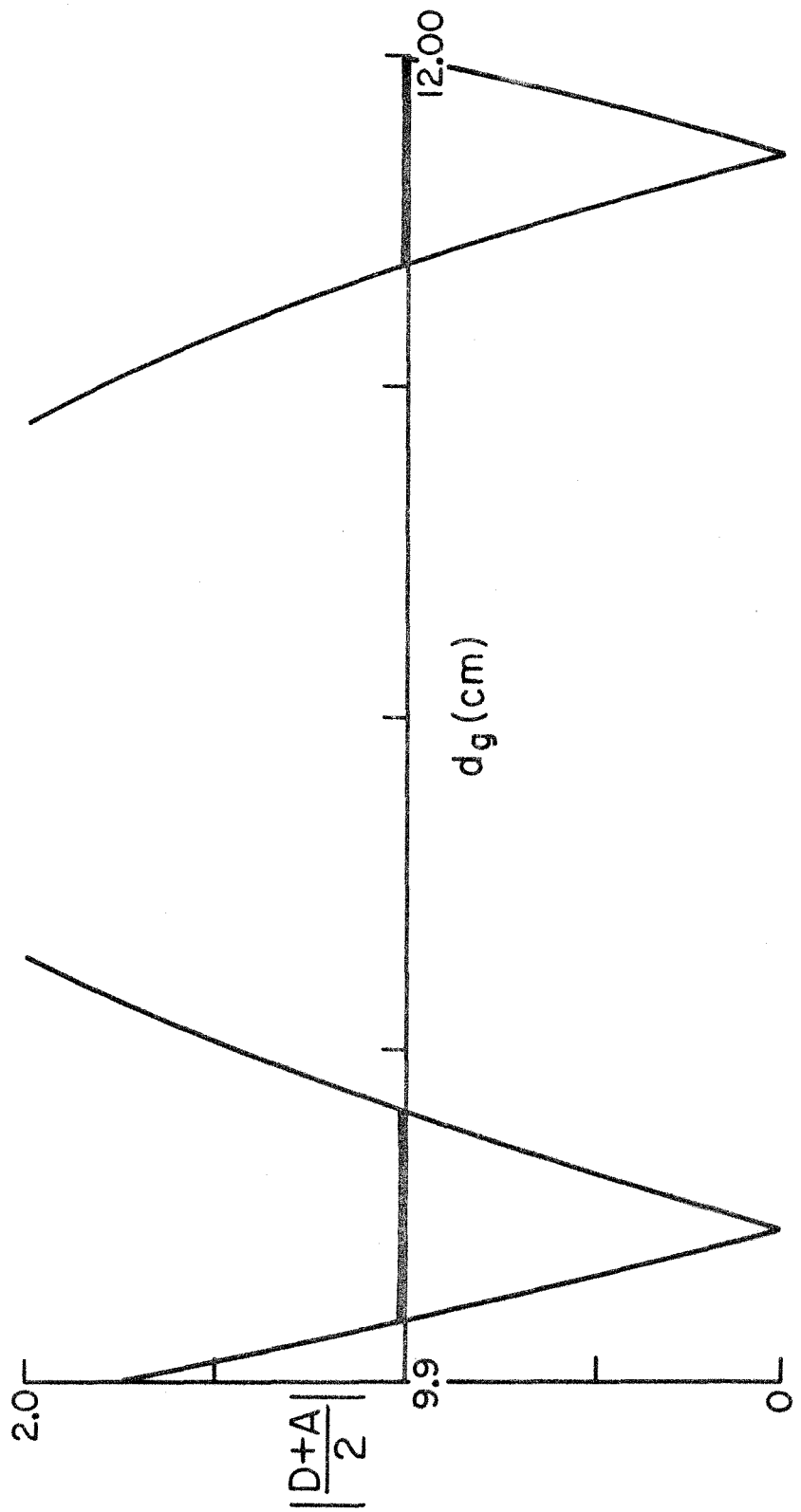

Fig. 3.5.2 $|(D+A)/2|$ v.s. d_g of the linear cavity of Fig. 3.5.1.
The heavy lines indicate the stability regions.

$$\text{(a)} \qquad 10.00 < d_g < 10.33 \text{ cm}$$
$$\text{(b)} \qquad 11.67 < d_g < 11.99 \text{ cm} \tag{3.5.1}$$

(It should be noted that the application of the imaging rules quoted in Section 3.2 in conjunction with the example given there for a two-mirror cavity simplifies the calculation of the stability ranges significantly, compared to the straightforward round trip multiplications of the ABCD matrices.) The confocal parameters in the three arms are plotted in Figure 3.5.3. The region near the boundary of the stability range of Figure 3.5.3c (the absorber arm) is shown in expanded scale in Figure 3.5.3d. The behavior of the confocal parameter at the absorber arm emphasizes the high sensitivity of the laser optimal operation to correct mirror spacings. This has been observed in the alignment of our laser.

The optimal length of the gain arm is seen to be $d_g = 10.180$ cm in the first stability region and $d_g = 11.81$ cm in the second. Small deviations from these spacings ($\sim \pm 50$ μm), for instance due to small vibrations of the mirrors, will not cause significant fluctuations in the beam spot size.

The beam parameters in each arm, i.e., the confocal parameter and the waist radius (at $\lambda = 6150$Å) and its location, at the optimal length of the gain arm, are listed in Table I for the two stability regions (the notations are as in Figure 3.5.1). The spot size at the absorber arm is smaller than that of the gain arm, as required for proper mode locking (see Section 2.1). Note, however, that all the waist radii are calculated in free air, not in the dye jets or the dumper, since we assumed

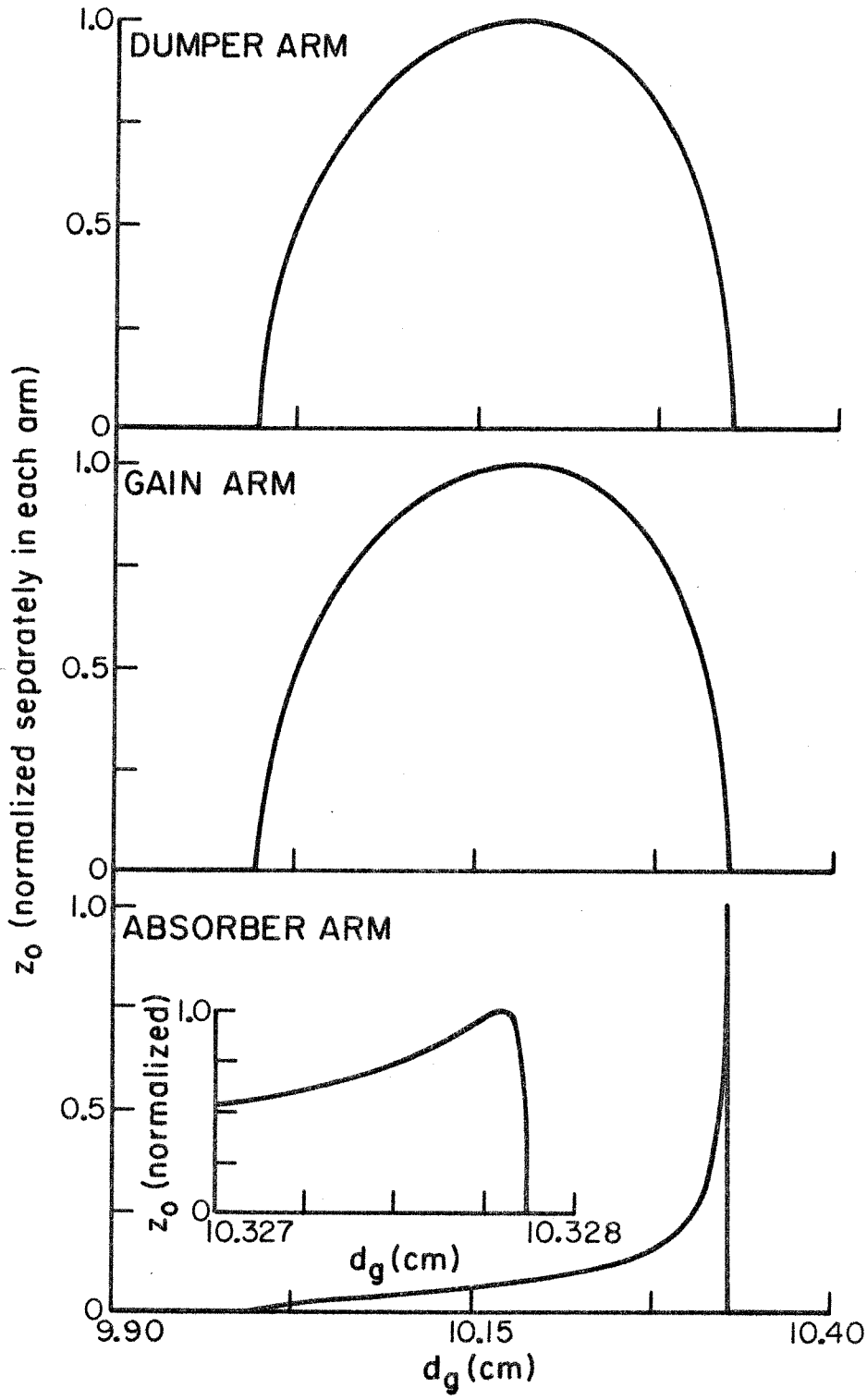

Fig. 3.5.3 The confocal parameters in the three arms of the linear cavity of Fig. 3.5.1. The inset in the absorber arm is a blow-up of the sharp peak of z_0 at this arm.

TABLE I

Beam parameters for each arm of the empty linear cavity of Figure 3.5.1 at the optimal length of the gain arm. Mirror spacing is the same as in Figure 3.5.1.

ARM	L1 (cm)	L2 (cm)	z_o(cm)	w_o(μm) @ 6150Å
First stability range: $10.00 < d_g < 10.33$ cm				
Dumper	9.96	10.04	0.659	35.9
Gain	5.02	5.16	0.164	17.9
Absorber	2.50	5.00	0.082	12.7
Second stability range: $11.67 < d_g < 11.99$ cm				
Dumper	0.22	19.78	1.458	53.4
Gain	6.65	5.16	0.164	17.9
Absorber	2.5	5.00	0.082	12.7

an empty resonator. It is also clear that it is impractical to operate the laser in the second stability range, since the beam waist in the dumper arm is located very close to the end mirror. As a result, not only would there not be enough space to insert the dumper, but also, the primary diffracted beam would not be sufficiently separated from the undiffracted beam at the end mirror so as to be efficiently extracted from the cavity. Nevertheless, for the completeness of the discussion, both stability ranges will be considered here.

Let us now include the dumper and the two dye jets in the cavity, all at their respective Brewster angles. Following the discussion of Section 3.4, we consider "parallel" and "perpendicular" cavities. Considering the same cavity dimensions used above for the empty linear cavity, we replace each Brewster window by its effective optical path, given by (3.4.1) and (3.4.2). The "parallel" and "perpendicular" empty cavities are treated similarly to the empty linear cavity. To point out the astigmatic effect of the Brewster windows on the stability region of the laser, the confocal parameter in the absorber arm of the parallel cavity is plotted in Figure 3.5.4, sharing a common axis with that of the perpendicular cavity. The beam parameters in the empty parallel and perpendicular effective cavities, at the gain arm optimal length of the first stability region, are listed in Table II.

The effect of the astigmatism on the beam parameters is evident from the table. Its effect on the effective range over which stable operation of the laser is achievable, is dramatized by the peculiar behavior of the confocal parameter in the absorber arm. Clearly the effective stability range is narrowed significantly, compared to that of the empty linear cavity.

To increase the stability range of the cavity, we resort to the method of astigmatism compensation by tilted mirrors, described in Section 3.4. The astigmatism in each arm is compensated separately, independent of the others. Equation (3.4.10) can be used for the two end arms, but it must be modified for the gain arm, because unlike the others, it includes two folded mirrors, which add up their astigmatic effects.

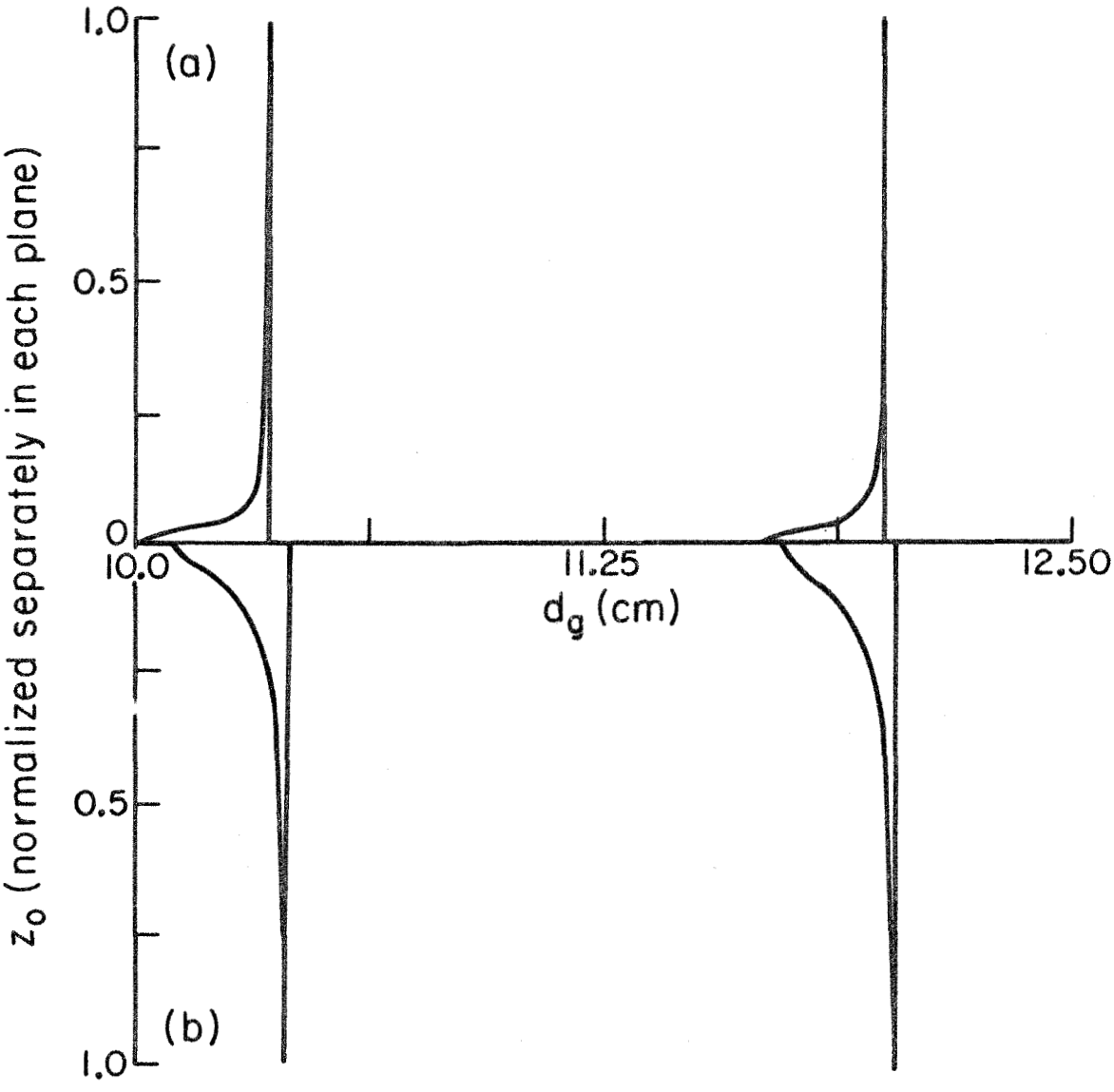

Fig. 3.5.4 The confocal parameter in the absorber arm as a function of the gain arm spacing in (a) the parallel and (b) the perpendicular linear cavities of Fig. 3.5.1 with Brewster windows.

TABLE II

Beam parameters for each arm at the optimal length of the gain arm for the linear cavity with the Brewster elements inserted in it. The mirror spacings are the effective optical paths (see text) of the real spacing of Figure 3.5.1. Waist diameter is in free air. Both planes are calculated in their first stability range (par = parallel plane, per = perpendicular plane).

ARM	Plane	L1 (cm)	L2 (cm)	z_o (cm)	w_o (μm) @ 6150Å
Dumper	par	9.96	9.96	0.668	36.2
	per	9.95	9.75	0.685	36.6
Gain	par	5.04	5.17	0.160	17.7
	per	5.08	5.18	0.148	17.03
Absorber	par	2.50	5.00	0.084	12.8
	per	2.49	5.00	0.091	13.35

To investigate the astigmatic compensation in the gain arm, the equivalent cavities are drawn in Figure 3.5.5. We set the dumper and the absorber arms such that their spacing is equal to the sum of the respective end-mirror radius of curvature and the focal length of the lens (or closely so, when the lens is replaced by a mirror tilted at a small angle). As a result $R_1 >> D_1$, f, and $R_2 >> D_2$, f (for notations please refer to Figure 3.5.5). Therefore, it can be seen from (3.2.12) that

$$R_{1,2} \simeq -f^2/(D_{1,2} - f) < 0 \qquad (3.5.2)$$

so that the radii of curvature of the equivalent mirrors point away from each other, as shown in the figure.

To find the stability region, we compare the equivalent empty two-mirror resonator to the similar resonator analyzed in Section 3.2. Accordingly, we identify the following regions of stability:

$$\text{(a)} \quad D_1' + D_2' + R_1' + R_2' < d_g < D_1' + D_2' + R_1'$$

$$\text{(b)} \quad D_1' + D_2' + R_2' < d_g < D_1' + D_2' \qquad (3.5.3)$$

or, using (3.2.13) and (3.5.2),

$$\text{(a)} \quad 2f < d_g < 2f + \frac{f^2}{D_2 - f}$$

$$\text{(b)} \quad 2f + \frac{f^2}{D_1 - f} < d_g < 2f + \frac{f^2}{D_1 - f} + \frac{f^2}{D_2 - f} \qquad (3.5.4)$$

Let us now replace the gain arm lenses by mirrors, both set at the same angle; then the effective spacings in the x- and y-planes are

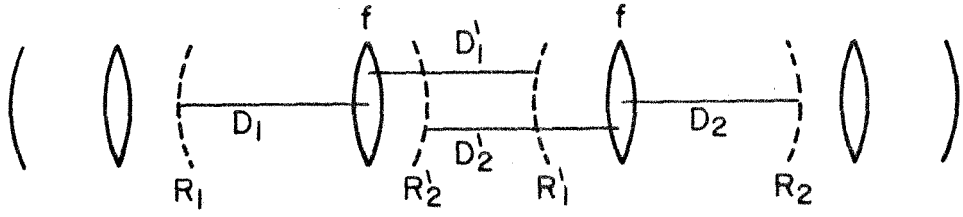

Fig. 3.5.5 The equivalent two mirror resonator of the linear cavity of Fig. 3.5.1.

$$
\text{(a)}\qquad
\begin{aligned}
d_{gx} &= 2f_x + \delta_x \qquad & 0 < \delta_x < \frac{f_x^2}{D_2 - f_x} \\
d_{gy} &= 2f_y + \delta_y \qquad & 0 < \delta_y < \frac{f_y^2}{D_2 - f_y}
\end{aligned}
$$

$$
\text{(b)}\qquad
\begin{aligned}
d_{gx} &= 2f_x + \frac{f_x^2}{D_1 - f_x} + \delta_x \qquad & 0 < \delta_x < \frac{f_x^2}{D_2 - f_x} \\
d_{gy} &= 2f_y + \frac{f_y^2}{D_1 - f_y} + \delta_y \qquad & 0 < \delta_y < \frac{f_y^2}{D_2 - f_y}
\end{aligned}
\qquad (3.5.5)
$$

Following the discussion in Section 3.4, we find that in order to compensate the astigmatism we require in the first stability region

$$2(f_x - f_y) = d_x - d_y \qquad (3.5.6)$$

while in the second

$$2(f_x - f_y) + \frac{f_y^2}{D_1 - f_x} - \frac{f_y^2}{D_1 - f_y} = d_x - d_y \qquad (3.5.7)$$

It is thus obvious that the astigmatism in the two regions of stability cannot be compensated by the same folding angle θ_g of the gain arm mirrors. Also for typical dimensions of cavities, D_1 is not very large or small compared with f_x and f_y, so that the solution of (3.5.7) for the folding angle is complicated. On the other hand, (3.5.6) is easily solved in a manner similar to that of Section 3.4, i.e.,

$$Nt = R_f \sin\theta \tan\theta \qquad (3.5.8)$$

where N, t, R_f, and θ are defined in Section 3.4.

Applying equations (3.4.10), (3.4.11), and (3.5.8) to the folded cavity of Figure 2.7.1, using for the dumper t = 0.48 cm and n = 1.46 and for the dye jets t = 0.015 cm and n = 1.43, we find

$$\theta_d = 0.15 \text{ rad} = 8°36'$$

$$\theta_{g1} = \theta_{g2} = 0.026 \text{ rad} = 1°29'$$

$$\theta_a = 0.051 \text{ rad} = 2°55' \qquad (3.5.9)$$

The confocal parameter in the gain arm of the parallel and perpendicular empty cavities (no Brewster elements), folded at these angles, is shown in Figures 3.5.6 as a function of the length of that arm. Note that the relative displacement of the stability ranges is in the opposite direction to that of the linear cavity which includes the Brewster elements (Figure 3.5.4).

Finally, the confocal parameters in the gain and the absorber arms in the astigmatically compensated cavity are shown in Figure 3.5.7 as a function of d_g. This cavity is folded at the angles of (3.5.9) and includes the Brewster elements. As expected, only the first regions of stability of the x- and y-plane cavities fully overlap. To compensate the astigmatism of the second stability region, smaller folding angles are required (as can also be seen by comparing equation (3.5.7) with (3.5.6)), which are not practical in the construction of a real laser.

Conclusion

Throughout this section, the length of the gain arm has been varied while keeping the rest of the arms fixed at a predetermined mirror spacing. In practice, it is impossible to determine the mirror spacing to

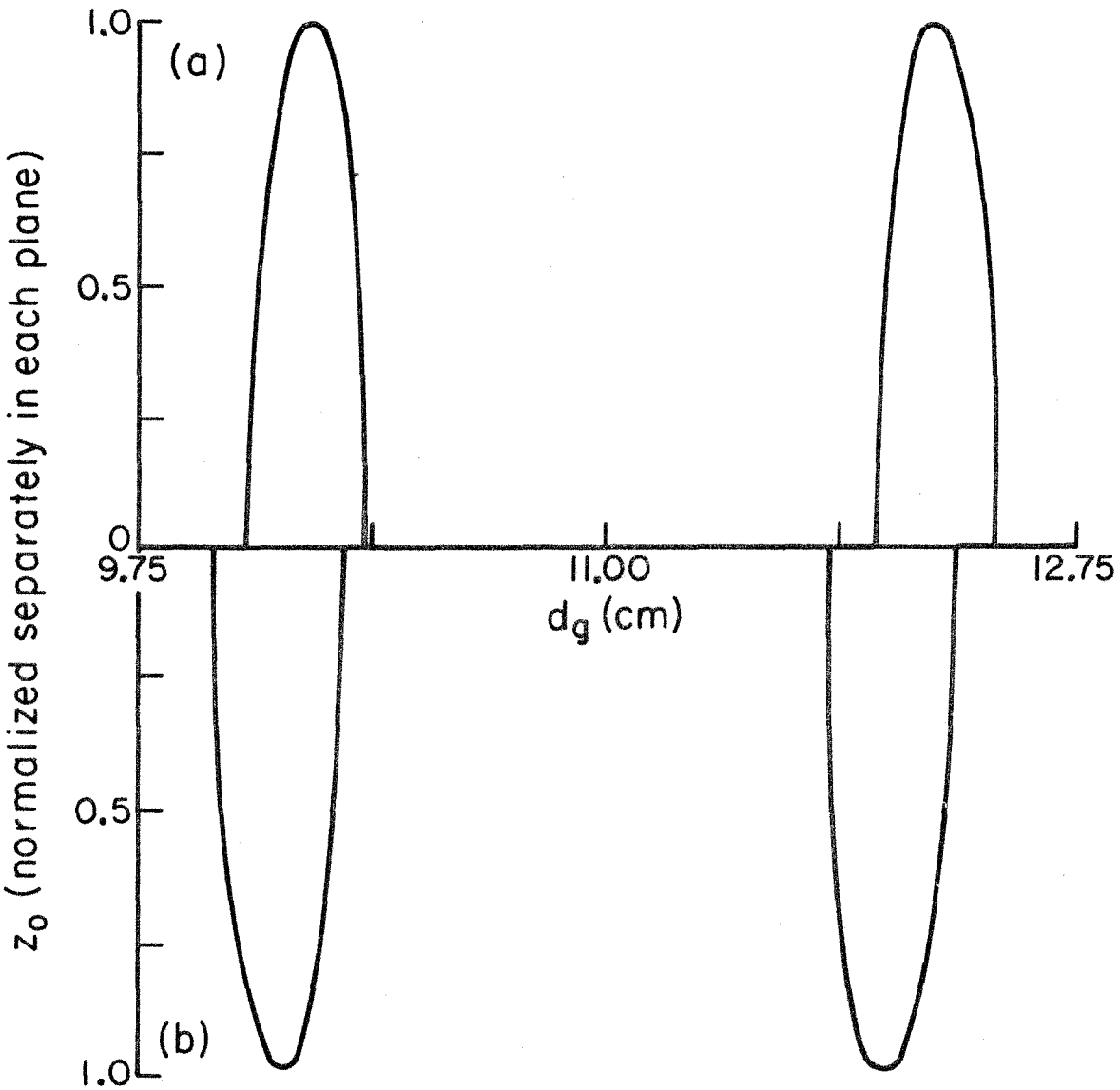

Fig. 3.5.6 The confocal parameter in the gain arms of (a) the parallel and (b) the perpendicular empty folded cavities, for dimensions as in Fig. 3.5.1 and $\Theta_d = 8°36'$, $\Theta_{g_1} = \Theta_{g_2} = 1°29'$, and $\Theta_a = 2°55'$.

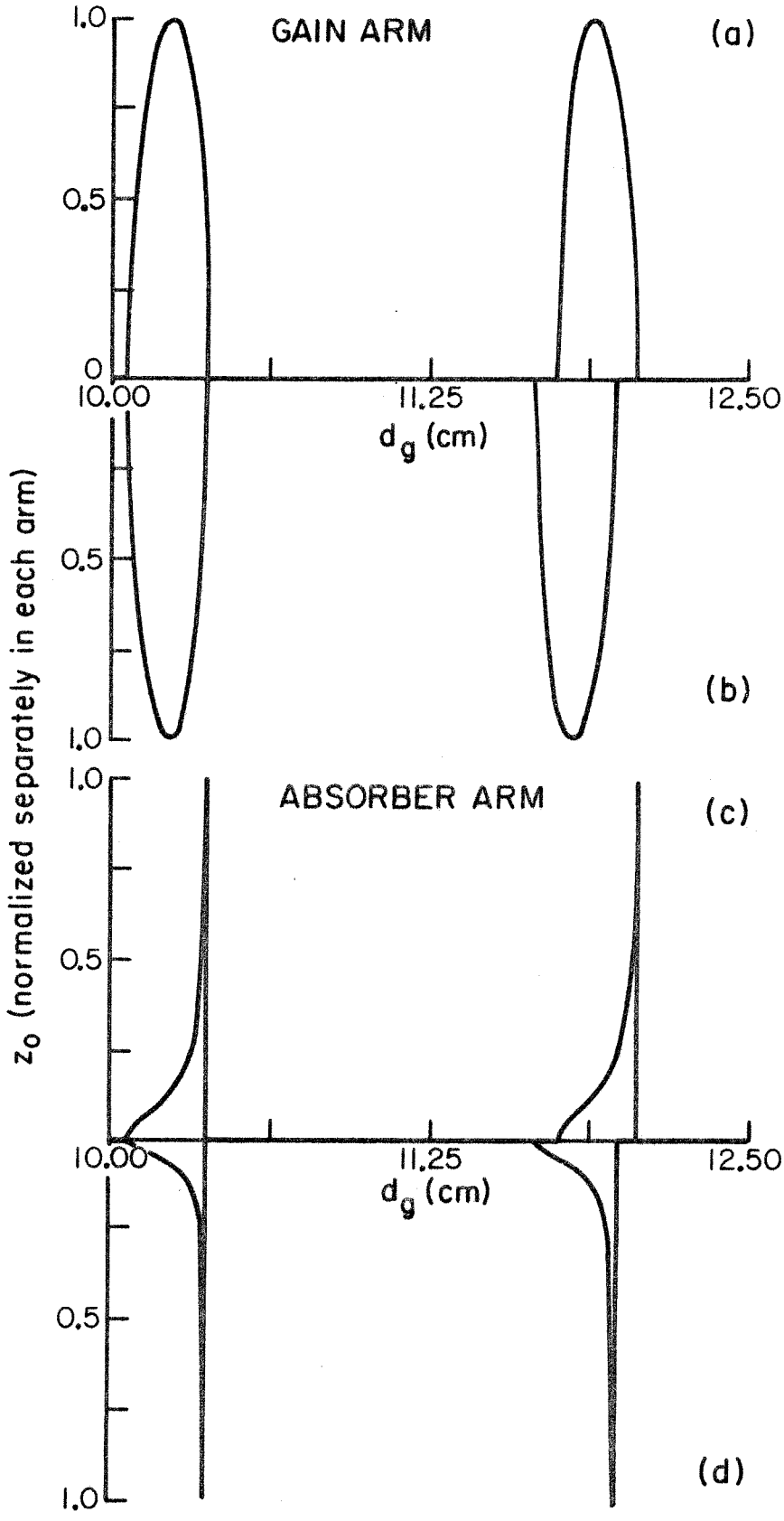
GAIN ARM
(a)
1.0
0.5
0
10.00
11.25
12.50
d_g (cm)
0.5
1.0
(b)
ABSORBER ARM
(c)
1.0
0.5
10.00
11.25
12.50
d_g (cm)
0.5
1.0
(d)
z_o (normalized separately in each arm)

Fig. 3.5.7 The confocal parameters in the gain and absorber arms of the astigmatically compensated cavity. (a) and (c) are in the parallel plane, (b) and (d) in the perpendicular. Dimensions are as in Fig. 3.5.1.

an accuracy of less than 1-2 millimeters. However, as will be clear from Section 5.1, once two arms are set, the third one can be adjusted to its appropriate spacing within 25 μm. Accordingly, the calculations of this section can be used as a guide line in the alignment procedure of the cavity, both in the initial alignment as described in Section 5.1, and in the following fine tuning of the cavity.

Chapter 4

PULSE WIDTH MEASUREMENTS

4.0 Introduction

Picosecond pulses are shorter than the temporal resolution limit of any combination of a photodetector and oscilloscope. Sampling oscilloscopes, which require a continuous train of pulses, are limited to rise times of $\sim$ 25 psec or longer, and the fastest photodetectors available today are limited to rise times of 30-50 psec.

Special techniques have been developed to measure the temporal behavior of subpicosecond pulses. A review of these techniques can be found in references [38] and [39]. The only direct linear method capable of supplying information regarding the pulse intensity profile is the streak camera [38]. However, it is very expensive (> \$50,000) and for experiments in which the required resolution time is longer than several times the estimated pulse width, it can be given up in favor of less expensive techniques. The most common of these involve nonlinear effects, such as two-photon absorption (TPA) and second harmonic generation (SHG). They give good estimates of the pulse width, but are insensitive to pulse asymmetry. More complete information is obtained by higher orders of nonlinear measurements [39]. The SHG technique, which has been used to measure the width of pulses generated in our experiment is the subject of Sections 4.1 and 4.2.

Although a SHG measurement is used to determine the pulse duration, it cannot be easily used as a real time monitor of the laser's operational state. Instead, a real time measurement of the laser band

width is performed. Such a measurement cannot determine the pulse width, unless the pulse is transform limited. However, it has been found very helpful in the process of system alignment and in monitoring the laser's operational stability. The real time bandwidth measurement is described in Section 4.3.

4.1 Pulse Width Measurement by Second Harmonic Generation

Nonlinear techniques can indicate the operational state of the laser, and if mode locked, can give an estimate of its pulse width. It was suggested and demonstrated first by Weber [40] and independently by Armstrong [41], that the width of picosecond pulses could be determined from second harmonic generation (SHG) measurements. In this section, the principles of the SHG technique will be developed. In the next section the experimental set-up is described, and the requirements of both the nonlinear crystal and the optical beam for maximum SHG efficiency will be discussed.

Consider traveling plane waves of the form

$$\vec{E}_{\omega}(\vec{r},t) = \frac{1}{2}\left[\vec{E}_{\omega}(z)\, e^{i(\omega t - \vec{k}_{\omega}\vec{r})} + \text{c.c.}\right] \tag{4.1.1}$$

then, the second harmonic induced polarization is given by

$$P^{NL}_{2\omega,\alpha} = d_{\alpha\beta\gamma}\, E_{\omega,\beta}\, E_{\omega,\gamma}\, e^{i\Delta\vec{k}\cdot\vec{r}} \tag{4.1.2}$$

where α, β, and γ represent the directions of polarization of the fields, $d_{\alpha\beta\gamma}$ is a tensor which depends on the properties of the crystal, and

$$\Delta\vec{k} = \vec{k}_{2\omega,\alpha} - \vec{k}_{\omega,\beta} - \vec{k}_{\omega,\gamma} \tag{4.1.3}$$

is the phase mismatch. For optimum SHG, $\Delta\vec{k}$ must vanish. The conditions under which this phase matching is satisfied will be discussed in the next section. We will assume here that $\Delta\vec{k} = 0$. The SHG power can be shown to be proportional to $|P^{NL}_{2\omega,\alpha}|^2$, i.e.,

$$P_{2\omega,\alpha} = K\, d^2_{\alpha\beta\gamma}\, |E_{\omega,\beta}\, E_{\omega,\gamma}|^2 \tag{4.1.4}$$

where, for the purpose of this discussion, K is a constant.

Let us refer now to the SHG set-up of Figure 4.2.1 . Each pulse is split into two identical halves which follow different paths before impinging upon the nonlinear crystal. A time delay between these pulses is established by changing the optical path length of one of them.

Two types of SHG are defined according to the polarization of the two fundamental waves. In the first type, both polarizations are the same, while in the second they are perpendicular to each other. The two types give somewhat different results in SHG measurements.

SHG of the First Type

Assume first that the two fundamental waves propagate colinearly then the total electric field at the crystal is

$$E_{\omega,\beta} = E(t)e^{i\omega t} + E(t+\tau)\, e^{i\omega(t+\tau)} \tag{4.1.5}$$

where E(t) is the field envelope of the quasi-monochromatic pulse, and τ is the delay time between the two pulses. Then the SH power is

$$P_{2\omega,\alpha} = K\, d^2_{\alpha\beta\beta}|E^2_{\omega,\beta}|^2 = K\, d^2_{\alpha\beta\beta}\{[I^2(t) + I^2(t+\tau) + 4I(t)\, I(t+\tau) + 2I(t)\, I(t+\tau)\cos 2\omega\tau + 4[I(t) + I(t+\tau)]\, E(t)\, E(t+\tau)\cos\omega\tau\} \tag{4.1.6}$$

where $I(t) \equiv |E(t)|^2$. The SH power is detected by a photodetector with a resolution time which is much longer than the pulse duration (several nanoseconds compared to picoseconds). The photocurrent is, therefore, proportional to $\int_0^\infty P_{2\omega,\alpha}(t)\,dt$, or to the average of $P_{2\omega,\alpha}(t)$, which we will denote by $\langle P_{2\omega,\alpha}(t)\rangle_t$. Thus, at a pulse delay time τ, the photocurrent $i(\tau)$ is found from (4.1.6) to be proportional to

$$i(\tau) \propto \langle P_{2\omega,\alpha}(t)\rangle_t \propto g_1(\tau) \equiv 1 + 2G^{(2)}(\tau) + C(\tau) \tag{4.1.7}$$

where $G^{(2)}(\tau)$ is the autocorrelation function of the pulse intensity, defined by

$$G^{(2)}(\tau) \equiv \frac{\langle I(t)\ I(t+\tau)\rangle_t}{\langle I^2(t)\rangle_t} \tag{4.1.8}$$

and

$$C(\tau) = G^{(2)}(\tau)\cos 2\omega\tau + 2\,\frac{\langle [I(t) + I(t+\tau)]\ E(t)\ E(t+\tau)\rangle}{\langle I^2(t)\rangle}\cos\omega\tau \tag{4.1.9}$$

At $\tau = 0$, $g_1(0) = 8$, while at $\tau = \infty$, $g_1(\infty) = 1$. However, if the delay varies at a rate higher than λ/RC, where λ is the optical wavelength and RC is the time constant of the recording system, $C(\tau)$ averages out to zero and

$$g_1(\tau) = 1 + 2G^{(2)}(\tau) \tag{4.1.10}$$

so that near $\tau = 0$, $g_1(\tau \simeq 0) = 3$.

SHG of the Second Type

Since the fundamental fields must be orthogonal for second harmonic generation, the SH power is given simply by

$$P_{2\omega,\alpha} = K\, d^2_{\alpha\beta\gamma} |E_\gamma(t)\, E_\gamma(t+\tau)|^2 \qquad (4.1.11)$$

so that

$$i(\tau) \propto P_{2\omega,\alpha} \propto g_2(\tau) \equiv G^{(2)}(\tau) \qquad (4.1.12)$$

so that $g_2(\infty) = 0$ and $g_2(0) = 1$. The functions $g_1(\tau)$ and $g_2(\tau)$ are shown in Figure 4.1.1 for three modes of operation of the laser: free running, noise burst, and single pulse. A pulse which results from an incomplete mode locking can be considered a noise burst, and its coherence is determined from the width of the spike at $\tau = 0$ of the corresponding SH trace. The behavior difference between these three cases of $g_1(\tau)$ and $g_2(\tau)$ serves as an indication of the operational state of the laser.

If the shape of the pulse intensity is known, then by substituting its mathematical expression in (4.1.8), the relation between the widths of $G^{(2)}(\tau)$ and of the pulse can be found. For example, for a Gaussian $\Delta\tau/\Delta t_p = \sqrt{2}$, where $\Delta\tau$ and Δt_p are the full widths at half maximum of $G^{(2)}(\tau)$ and $I(t)$, respectively. Similarly, for a secant hyperbolic pulse, $\Delta\tau/\Delta t_p = 1.55$

It is preferred that the SHG measurement is performed with fundamental Gaussian beams, because the interpretation of the results is based on the assumption that the overlap of the two pulses depends only on the relative delay between them. If higher transverse modes are used, transverse misalignment of the beams will affect the SHG, even if the incident beams are colinear, so that the corresponding photocurrent will not be represented by $G^{(2)}(\tau)$ [42].

Notice that $G^{(2)}(\tau)$ is symmetric in τ. As a result, the SHG is insensitive to the pulse asymmetry, and might give erroneous results if

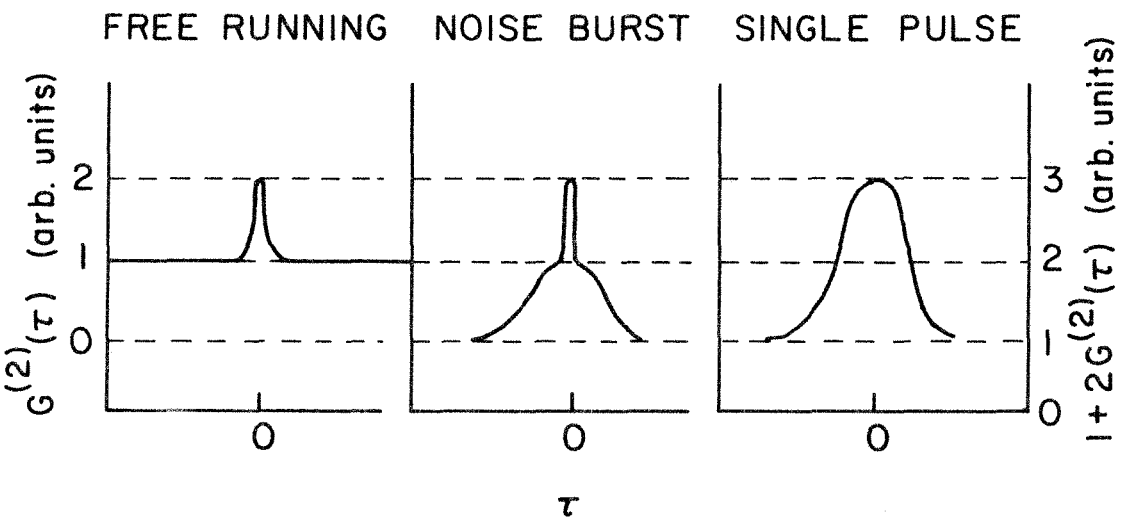

Fig. 4.1.1 Autocorrelation traces of colinear SHG of the first type ($1 + 2G^{(2)}(\tau)$), and of the second type ($G^{(2)}(\tau)$). Noncolinear SHG of the first type also results in measuring $G^{(2)}(\tau)$.

the exact pulse shape is not known. However, as long as the resolution required by the experiment in which the picosecond pulses are employed is several times the estimated pulse duration, this technique is satisfactory.

4.2 The SHG Set-Up

The SHG set-up used by us is shown in Figure 4.2.1. (It is identical to the one used by Ippen and Shank [3].) It can be divided into three stages: The interferometer, the second harmonic generator, and the detection system. The first stage is straightforward and only some of its technical details will be given. The design of the second stage involves many general properties of SHG and will be discussed in detail. In the third stage, only the averaging process needs some explanation and analysis, which will be presented.

(i) The Interferometer

The interferometer is designed so that the beam is not reflected back to the laser. Its movable arm is driven by a stepping motor with a resolution in optical delay of 2.12×10^{-14}sec/step.

(ii) The SHG Stage

This stage consists of a KDP (KH_2PO_4) crystal and a focusing lens. The KDP has natural birefringence, which allows phase matching. The phase matching condition

$$\Delta\vec{k} = \vec{k}_{2\omega,\alpha} - \vec{k}_{\omega,\beta} - \vec{k}_{\omega,\gamma} = 0 \qquad (4.2.1)$$

for $\lambda \simeq 6100\mathring{A}$ in KDP can be satisfied only if the two fundamental waves are ordinary and the second harmonic wave is extraordinary. If the angle between the fundamental beams is 2β, then equation (4.2.1) can be

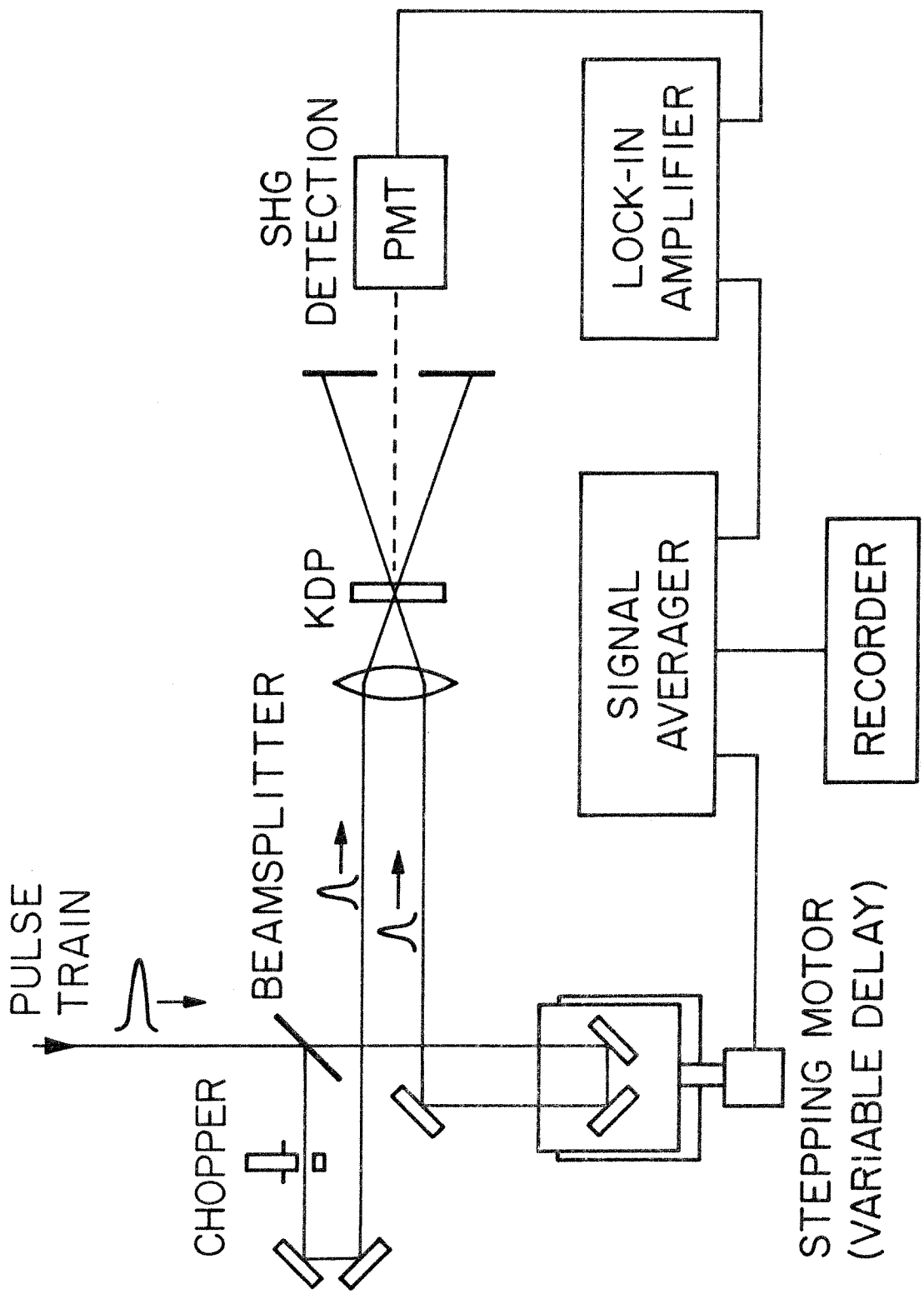

Fig. 4.2.1 Second harmonic generation set up for pulse autocorrelation measurements.

shown to be equivalent to

$$n_e^{2\omega}(\theta_m) = n_o^{\omega} \cos \beta \tag{4.2.2}$$

where θ_m is the angle between the optical axis of the crystal and the direction of propagation of the second harmonic beam, $n_e^{2\omega}(\theta_m)$ is the extraordinary index of refraction in this direction at angular frequency 2ω, and n_o^{ω} is the ordinary index of refraction at ω.

From the birefringent properties of KDP [29e], it can be shown that

$$\sin^2\theta_m = \frac{(n_o \cos \beta)^{-2} - (n_1^{2\omega})^{-2}}{(n_e^{2\omega})^{-2} - (n_o^{2\omega})^{-2}} \tag{4.2.3}$$

Since $\sin^2\theta_m \leq 1$, β is confined to

$$\beta < \cos^{-1} \frac{n_e^{2\omega}}{n_o^{\omega}} \tag{4.2.4}$$

In KDP, at $\lambda = 6100\text{Å}$, $n_e^{2\omega} = 1.496752$, $n_o^{2\omega} = 1.543934$, and $n_o^{\omega} = 1.508818$ so that $\beta < 7°15'$. The crystal in the set-up is cut for normal incidence at $\theta_m = 60°28'$. Therefore, from (4.2.3), the angle between each of the fundamental beams and the normal to the crystal plane is $\beta = 2°5'$.

Notice that when $\beta > 0$, the SH photocurrent is proportional to $G^{(2)}(\tau)$ and not to $1 + 2G^{(2)}(\tau)$, as it is for SHG of the first type with colinear beams (see the previous section). This method improves the resolution at the tails of $G^{(2)}(\tau)$. It also makes it easier to block the fundamental beams from getting into the photodetector, thus improving the signal-to-noise ratio.

There is one more degree of freedom to be determined: The azimuthal angle, ϕ, of the polarization of the fundamental beams with respect to the crystallographic axis. It is chosen so as to maximize the second order nonlinear coefficient d, which for SHG of the first type under phase matching conditions is found (by coordinate transformation) to be

$$d = d_{14} \sin 2\phi \sin \theta_m \tag{4.2.5}$$

where d_{14} is an element of the second order nonlinear susceptibility tensor. Consequently, $\phi = 45°$ and $d = 0.87\ d_{14}$ ($d_{14} = 4.4 \times 10^{-24}$ in MKS units [29f]).

Now that the orientation of the crystal is determined, the question of its thickness is addressed. The thickness is chosen so that the optical path is shorter than the effective coherence length due to phase mismatch.

$$\Delta k = \frac{2\omega}{c} [n_{e,\theta_m}(2\omega) - n_o(\omega) \cos \beta] \tag{4.2.6}$$

Taking

$$\Delta k = \left.\frac{d\Delta k}{d\nu}\right|_{\nu_o,\theta_m} \cdot \Delta\nu \tag{4.2.7}$$

and using the index ellipsoid formula for KDP [29e] and the expression for $n_e(\bar{\nu})$ and $n_o(\bar{\nu})$ given by Zernike [43], the coherence length is found to be

$$\ell_c = \frac{2\pi}{\Delta k} \simeq 1 \text{ cm} \tag{4.2.8}$$

for $\lambda = 6100$ Å, $\theta_m = 60°28'$, and $\beta = 2°5'$. Accordingly, the thickness of the KDP crystal was chosen to be 1 mm.

The Focusing Lens

In a thin crystal and with an unfocused beam, the efficiency of SHG is proportional to ℓ^2/A, where ℓ is the optical path length in the crystal and A is the cross sectional area of the beam. It is, therefore, tempting to focus the beam and to use a thick crystal in order to increase the second harmonic power. However, several factors limit the SHG efficiency. First, the smaller the spot size, the stronger the diffraction of the beam. Then, not only does the cross-sectional area increase rapidly away from the waist, but also a phase mismatch is built up. Second, there is the double refraction feature of the birefringent material in which the SH wave propagates in a different direction than the fundamental. The refraction angle can be shown to be given by

$$\tan \rho = \frac{n_o^2(\omega)}{2} \sin 2\theta_m \left[\frac{1}{n_e^2(2\omega)} - \frac{1}{n_o^2(2\omega)}\right] \qquad (4.2.9)$$

For a KDP crystal and $\lambda = 6100\text{Å}$, the refraction angle is $\rho = 1°31' = 0.026$ rad. As a result, the effective interaction length between the fundamental beams and the SH beam is limited. Boyd et al. [44] showed that the effective coherence length associated with diffraction is actually identical with that which is associated with double refraction. Boyd and Kleinman [45] calculated the optimum SH power as a function of ℓ, z_o (the confocal parameter of the beam), ρ, λ, and n. Using their results, we find that for $\ell = 1$ mm, $n \simeq 1.5$, and $\lambda = 6100\text{Å}$, the optimum confocal parameter is

$$z_o = \frac{1}{4}\ell = 250\mu m \qquad (4.2.10)$$

i.e., waist diameter of $2w_o$ = 14 μm. Accordingly, by employing Gaussian beam focusing rules (see Section 3.3 or Ref. [37]), a lens with a focal length of 5 cm was chosen.

The Detection System

The detector is a photomultiplier (RCA 1P28) covered by an ultraviolet filter (Schott UG-5). Between the filter and the KDP crystal there is a slot which allows only radiation along the bisector of the fundamental beams to be detected, so that the transmitted fundamental beams are blocked.

The signal averager is Nic 1174 [46], which is synchronized with the moving arm when scanning both in the forward and backward directions. We will show here that the averaging increases the accuracy of the measured autocorrelation function in the case of fluctuations in the pulse intensity. Assume

$$I(t) = \bar{I}(t) + \Delta I(t) \qquad (4.2.11)$$

Then, due to the detection system integration time (see Section 4.1),

$$\begin{aligned} \langle I(t)\, I(t+\tau)\rangle_t = {} & \langle \bar{I}(t)\, \bar{I}(t+\tau)\rangle_t + \langle \Delta I(t)\, \bar{I}(t+\tau)\rangle_t \\ & + \langle \bar{I}(t)\, \Delta I(t+\tau)\rangle_t + \langle \Delta I(t)\, \Delta I(t+\tau)\rangle_t \end{aligned} \qquad (4.2.12)$$

where τ is the delay time between the pulses. If we repeat measuring (4.2.12) N times, and then average the results, we will get

$$\frac{1}{N}\sum^{N} \langle I(t)\ I(t+\tau)\rangle = \langle \overline{I}(t)\ \overline{I}(t+\tau)\rangle + \frac{1}{\sqrt{N}} \overline{\langle \Delta I(t)\ \Delta I(t+\tau)\rangle}_{N} \qquad (4.2.13)$$

where the bar denotes average. Thus, the signal-to-noise ratio improves by $\sqrt{N}$.

An experimental trace of $G^{(2)}(\tau)$ will be presented in the next chapter which summarizes the properties of the passively mode locked CW dye laser.

4.3 Simultaneous and Continuous Monitoring of the Laser Bandwidth

The pulse bandwidth has been monitored continuously during laser operation. Each pulse is sampled by its reflection from the dye jet or the dumper's quartz block, and is guided by an optical fiber to a monochromator (GCA/McPherson 2051). The exit slit of the monochromator is removed and the diffracted light is detected by a vidicon detector of an optical multichannel analyzer (P.A.R., OMA Model 1205A). The resolution of the combined system is $\sim$0.185Å, and it is calibrated with He-Ne and argon lasers.

The OMA enables us to observe the laser wavelength and its bandwidth continuously, simultaneous with any running experiment. This is an important tool in alignment and monitoring the laser, as will be clear from the next chapter.

Chapter 5

CONTROL AND OUTPUT CHARACTERISTICS OF THE PASSIVELY MODE LOCKED CW DYE LASER

5.0 Introduction

In the previous chapters the concepts of a passively mode locked CW dye laser and of its monitoring system have been discussed and analyzed. In the present chapter the control of the laser, for proper operation, will be described. At the conclusion its output characteristics will be given.

5.1 Initial Alignment of the Laser

The multimirror resonator has been analyzed in Section 3.5. In practice, it is difficult to construct a cavity with exact predetermined dimensions. The spacing between the strongly curved mirrors ($R = 5$ and 10 cm) cannot be easily measured, and the clumsiness of the mirror mounts, which are designed large in order to have high angular resolution, make the small folding angles unattainable. Therefore, the cavity is constructed with dimensions as close as possible to the desired ones, and then it is tuned to optimum laser operation by trial and error. The results of the analysis of Section 3.5 are used as a guideline to the alignment procedure.

Initial alignment is performed with the aid of the fluorescence emitted by the rhodamine 6G. The point source, formed by the focused argon laser beam, is imaged back on the jet after passing through the

cavity and being reflected backward by the end mirror (see Figure 2.7.1). By synchronizing the image and the source on the jet (in practice it is done by imaging both on a far screen) a stable cavity is formed for the fluorescence. This alignment places the cavity just at the edge of its stability range and fine adjustment of the mirror spacing is needed to obtain a stable cavity for laser operation.

The laser is monitored by three separate systems: 1) a fast photodiode with ∿100 ps rise time [31] detects the cavity radiation and displays it on an oscilloscope (1 ns rise time); 2) an optical multichannel analyzer (OMA, see Section 4.3); and 3) second harmonic generation with equal optical path (i.e., $\tau = 0$, see Section 4.1). With the OMA monitoring its wavelength, the laser is tuned to λ = 6100Å-6150Å and aligned to operate in its TE_{00} mode at threshold power of 600-800 mW (at the argon laser line λ = 5145Å). At that stage the laser is free running; its bandwidth is ∿5Å when operated near threshold, and wider when operated much above it. Under certain circumstances more than one band of frequencies would oscillate, as shown in Figure 5.1.1.

When the saturable absorber is introduced into the cavity, and the pumping power is kept near threshold, only one band of frequencies oscillates, and the bandwidth is reduced to ∿2-3Å. If the concentration of the absorber is not high enough, or its jet is not positioned correctly, the laser intensity is modulated with frequency $1/T_R$, where T_R is the cavity round trip time (see Figure 5.1.2).

When the absorber jet is better located, ∿1 ns detector limited pulses are displayed on the oscilloscope screen, as shown in Figure 5.1.3.

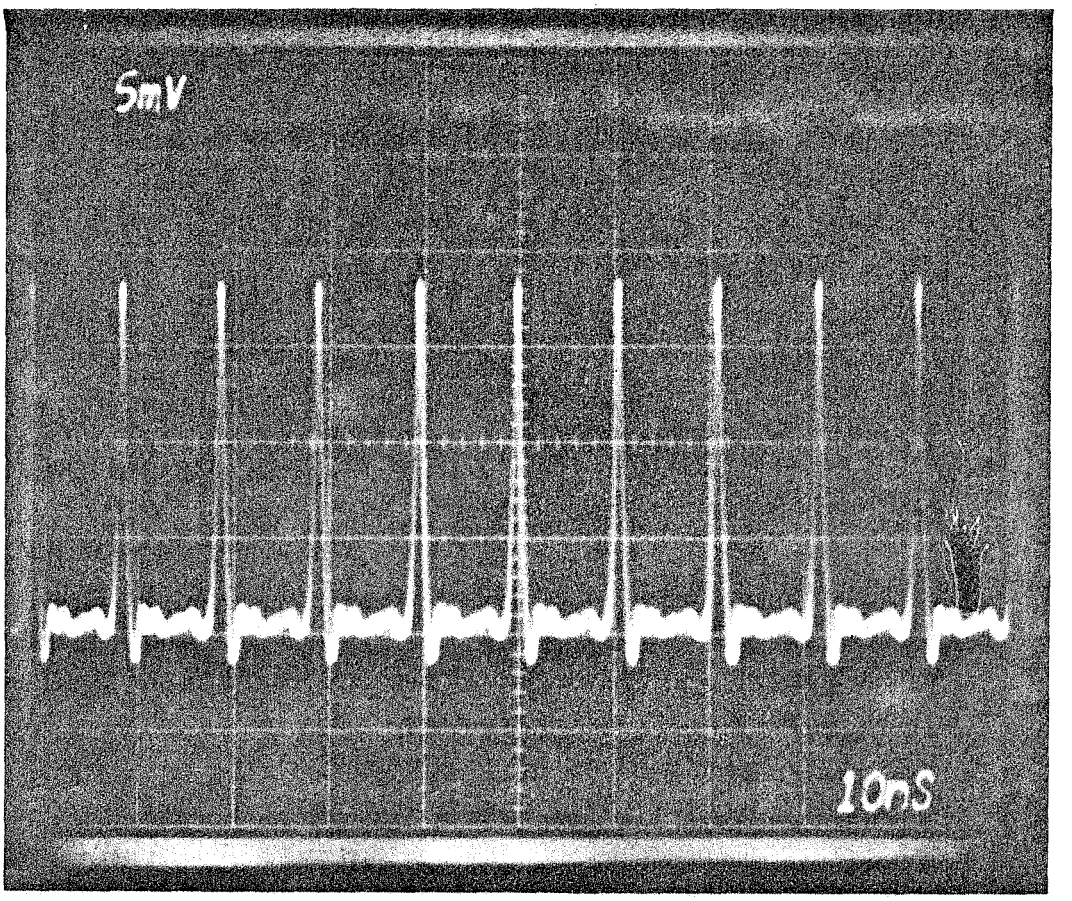

Fig. 5.1.3 Detector-limited pulses generated by the passively mode locked CW dye laser.

It will be seen later that this by itself is not an indication that the laser is completely mode locked. The laser is then aligned by fine adjustments until the bandwidth, which is displayed on the OMA, is wide enough ($\Delta\lambda \gtrsim 10\text{Å}$), as this is a necessary condition for picosecond pulses.

With the SHG set-up adjusted to zero delay between the halves of the pulses, the laser is tuned so as to maximize the SH power. When this is accomplished, a measurement of the SHG as a function of the path delay, as described in Section 4.2, is performed to determine the pulse width. A typical SHG curve is shown in Figure 5.1.4.

When the pumping power increases beyond threshold, the picosecond pulses increase in duration to ∿250-350 psec. At the same time, the bandwidth narrows considerably. When the pumping power increases further, each long pulse breaks into two ultrashort pulses and the bandwidth is wider again, although not as wide as during the single pulse operation. This observation is depicted in Figure 5.1.5. The spectrum of the laser, when displayed by the OMA, can thus be used to monitor the laser operational state in real time.

5.2 Summarizing the Laser Output Characteristics

The laser output characteristics were described in Section 2.7. They are repeated here:

λ = 6100-6150Å

$\Delta t_p \simeq$ 1-2 psec

peak power = 1-4 kW

repetition rate = $\sim 4.4 \times 10^4$ pps

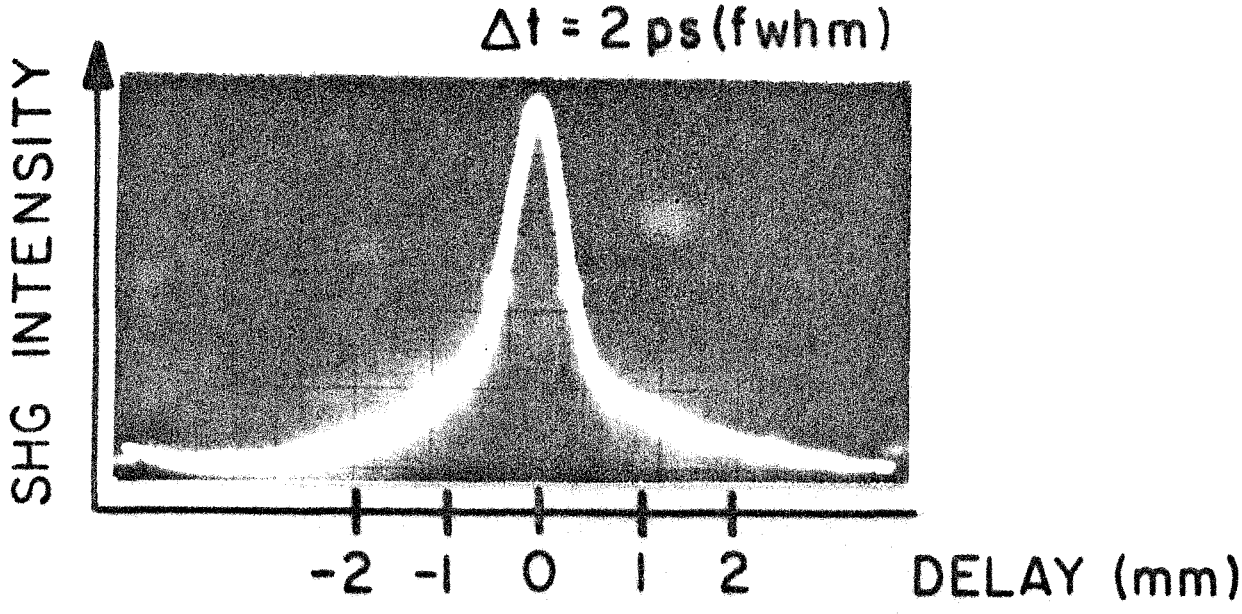

Fig. 5.1.4 A typical trace of a noncolinear second harmonic generation autocorrelation measurement (see Sections 4.1 and 4.2).

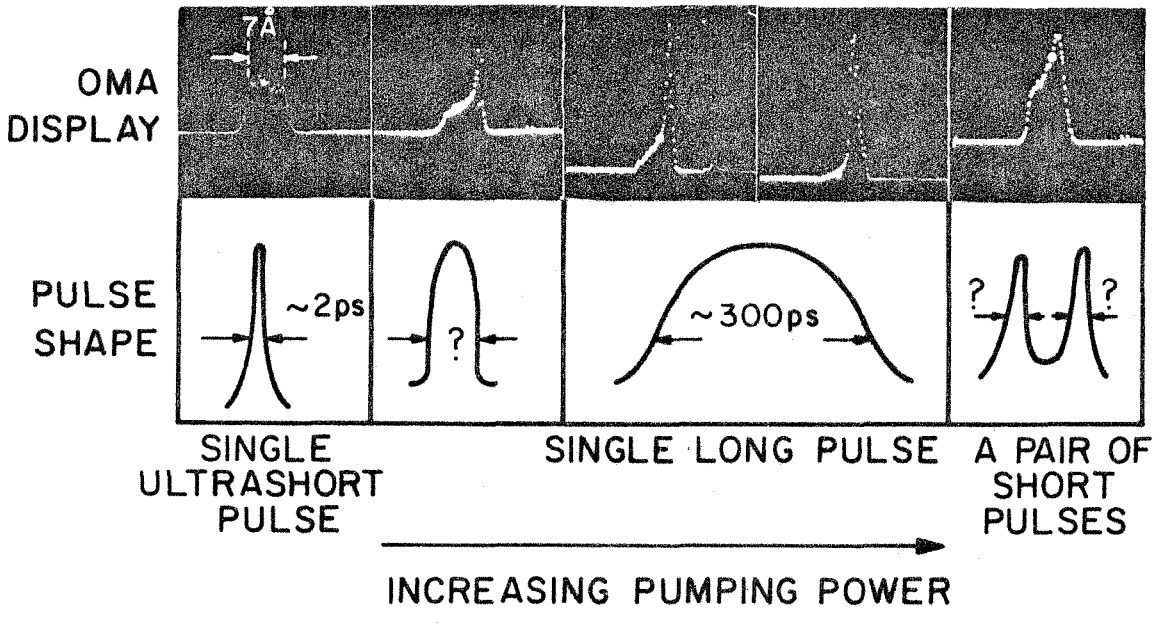

Fig. 5.1.5 Some typical laser pulse shapes and the related spectra at various pump levels.

Note: The pulses can be compressed to 0.3 psec [3]. However, in the experiments which we performed (see following chapters), such a resolution is not required and pulse compression has not been attempted.

REFERENCES - PART I

1. L. E. Hargrove, R. L. Fork, and M. A. Pollack, Appl. Phys. Lett. 5, 4 (1964).
2. C. V. Shank and E. P. Ippen, Appl. Phys. Lett. 24, 373 (1974).
3. E. P. Ippen and C. V. Shank, Appl. Phys. Lett. 27, 488 (1975).
4. A. Yariv, J. Appl. Phys. 36, 388 (1965).
5. E. M. Garmire and A. Yariv, IEEE J. Quant. Electron. QE-3, 222 (1967); Correction: IEEE J. Quant. Electron. QE-3, 377 (1967).
6. I. S. Ruddock and D. J. Bradley, Appl. Phys. Lett. 29, 296 (1976).
7. G.H.C. New, Opt. Comm. 6, 188 (1972).
8. G.H.C. New, IEEE J. Quant. Electron. QE-10, 115 (1974).
9. H. A. Haus, IEEE J. Quant. Electron. QE-11, 736 (1975).
10. Z. A. Yasa, O. Teschke, L. W. Bravermans, and A. Dienes, Opt. Comm. 15, 354 (1975).
11. M. Bass, T. F. Deutsch, and M. J. Weber, in Lasers, vol. 3, ed. by A. K. Levine and A. J. DeMaria (Marcel Dekker, Inc., New York, 1971), Ch. 3.
12. B. B. Snavely, Proc. of IEEE 57, 1374 (1969).
13. M. E. Mack, J. Appl. Phys. 39, 2483 (1968).
14. Coherent Radiation, Palo Alto, CA.
15. D. N. Dempster, T. Morrow, R. Rankin, and G. F. Thompson, J. Chem. Soc. Faraday II 68, 1479 (1972).
16. E. G. Arthurs, D. J. Bradley, and A. G. Roddie, Appl. Phys. Lett. 20, 125 (1972).
17. D. Magde and M. W. Windsor, Chem. Phys. Lett. 27, 31 (1974).
18. C. V. Shank and E. P. Ippen, Appl. Phys. Lett. 26, 62 (1975).

19. E. G. Arthurs, D. J. Bradley, and A. G. Roddie, Chem. Phys. Lett. 22, 230 (1973); Opt. Comm. 8, 118 (1973).

20. G. E. Bush, R. P. Jones, and P. M. Rentzepis, Chem. Phys. Lett. 18, 178 (1973).

21. E. P. Ippen, private communication.

22. This mixture was first recommended by E. P. Ippen through private communication. We have experimented with different concentrations, and this mixture was found to produce the most stable train of picosecond pulses.

23. Eastman Kodak, catalog no. 48.

24. CRC Physics and Chemistry Handbook (The Chemical Rubber Co. 1971-72).

25. Model 10.203, Lansing Research Corp., Ithaca, New York.

26. Weldon Tool Company, Cleveland, Ohio.

27. Acroflow cartridge #12572 and housing #12550.

28. Greer-Olaer "Shockushion" #A71530-200.

29. A. Yariv, Quantum Electronics (John Wiley and Sons, Inc., New York, 2nd ed., 1975): a) Sec. 14.9; b) p. 363, c) Sec. 6.6; d) Sec. 6.1; e) p. 424; f) p. 416.

30. Spectra Physics, Inc., Mountain View, CA.

31. G. H. McCall, Rev. Sci. Instrum. 43, 865 (1972).

32. The counter/pulse generator was designed and built by Mr. D. Armstrong.

33. H. W. Kogelnik, The Bell Sys. Tech. J. 44, 455 (1965).

34. J. R. Pierce, Theory and Design of Electron Beams (D. Van Nostrand Co., New York, 1954), Ch. 11.

35. H. W. Kogelnik, E. P. Ippen, A. Dienes, and C. V. Shank, IEEE J. Quant. Electron. QE-8, 373 (1972).

36. S. A. Tuccio and F. C. Strome, Jr., Appl. Optics 11, 64 (1972).

37. H. W. Kogelnik and T. Li, Appl. Opt. 5, 1550 (1966).

38. For a review, see D. J. Bradley, Ch. 2 in Topics in Applied Physics ed. by S. L. Shapiro (Springer-Verlag, 1977).

39. For a review, see E. P. Ippen and C. V. Shank, Ch. 3 in Topics in Applied Physics, ed. by S. L. Shapiro (Springer-Verlag, 1977).

40. H. P. Weber, J. Appl. Phys. 38, 2231 (1967).

41. J. A. Armstrong, Appl. Phys. Lett. 10, 16 (1967).

42. H. P. Weber and H. G. Danielmeyer, Phys. Rev. A 2, 2074 (1970).

43. F. Zernike, Jr., J. Opt. Soc. of Am. 54, 1215 (1964).

44. G. D. Boyd, A. Ashkin, J. M. Dziedzic, and D. A. Kleinman, Phys. Rev. 137, A1305 (1965).

45. G. D. Boyd and D. A. Kleinman, J. Appl. Phys. 39, 3597 (1968).

46. Nicolet Instrument Corp., Madison, Wisconsin.

Part II

PHOTOCONDUCTIVE IMPULSE RESPONSE AND EXCESS CARRIER LIFETIME OF Cr-DOPED GaAs

Chapter 6

GENERAL INTRODUCTION

6.0 Introduction

Since it was first found that high resistivity GaAs ($\rho \sim 10^8 \Omega$-cm) could be consistently prepared by doping it with chromium [1], semi-insulating Cr:GaAs has been used in a variety of applications. It is widely employed in epitaxial growth as a high resistivity substrate and, due to its relatively high mobility, it is used in microwave devices above the x-band frequencies [2]. Recently, it was suggested as a material suitable for fast photodetectors [3] and high speed optoelectronic switches [4].

Crystals of Cr:GaAs have been the subject of intensive investigations during the last fifteen years. Material growth has been improved to yield high resistivity single crystals. However, not only is the impurity concentration different from one growth to another, but the distribution is not uniform within the same ingot. This explains the wide range of results from photoelectronic measurements performed on this material ([36-40] and many others).

The subject of Part II of this thesis is the photoconductive impulse response and excess carrier lifetime of Cr:GaAs. The photocarrier lifetime in Cr:GaAs has been studied by photoconductivity measurements with both continuous and pulsed illumination. Under steady state conditions and with photon energy near or below the absorption edge, carrier lifetimes of 250 psec [53] to 0.1 μsec [59] have been measured. In contrast, when illuminated with an ultrashort laser pulse ($\sim$ 30 psec) and

photon energy much higher than the band gap energy, lifetimes shorter than 100 psec have been reported [3,4]. The short carrier lifetime in Cr:GaAs was attributed [4 ,53] to recombination centers formed near the GaAs mid-gap by the Cr dopant. However, prior to the work presented in this thesis, no analytical calculations of the process of recombination through flaws in Cr:GaAs have been published, and the inconsistency between the CW and the pulsed measured lifetimes has not been solved.

In our experiment, the photoconductive impulse response of Cr:GaAs was studied by irradiating the material with a continuous train of picosecond light pulses with photon energy above the band-gap energy. The pulses were generated by a mode locked CW dye laser, described in the first part of this thesis. Distortion of the photocurrent pulses by dispersion or reflections were minimized so that they did not affect the observation. A photoconductive decay time of $\sim$67 psec was deduced from the experimental results, and was interpreted as the result of both bulk and surface recombination. It was shown analytically that the 67 psec decay time agreed well with the carrier lifetime measured under steady state conditions.

6.1 Outline of Part II

The photoconductivity experiment and its results are described in Chapter 7. The effects of the electric circuit and the detection system on the observed current impulse are discussed and analyzed in Chapter 8, and the photoconductive impulse response of the samples is deduced from it. In Chapter 9, the photocarrier lifetime of Cr:GaAs is discussed, based on the electric and chemical properties of the material. The

experimental results are compared to analytical calculations which take into account both deep impurity levels and surface states.

Chapter 7

THE EXPERIMENT

7.0 Introduction

In this chapter our experimental set-up used to study the photoconductive impulse response of Cr:GaAs will be described, and the observed photocurrent impulse will be presented.

7.1 The Experimental Set-Up

The experimental set-up is shown in Figure 7.1.1. It resembles a typical arrangement for photoconductivity measurements in which the investigated material is connected in series to the electric circuit and the current is measured as a function of material illumination. In our experiment, the semi-insulating (SI) GaAs sample bridged a gap in the conductive strip of a microstrip transmission line. The microstrip was coaxially connected on one side to a dc power supply, and on the other, directly to a sampling oscilloscope. The optical picosecond pulses were generated by the passively mode locked CW dye laser described in Part I of this thesis. The pulses were of wavelength λ = 6100-6150Å, a duration of less than 2 ps, peak power of about 1 kW, and a repetition rate of 4.4×10^5pps.

Due to the high resistance of the semi-insulating GaAs ($\sim 10^9\Omega$), only a weak dark current flowed in the circuit. When the optical pulse was incident on the Cr:GaAs, electron-hole pairs were generated and the conductance of the gap increased. As a result the line was discharged through it and a current impulse was produced. When the SI-GaAs was restored to its high resistivity state, the current returned to its low level. This caused

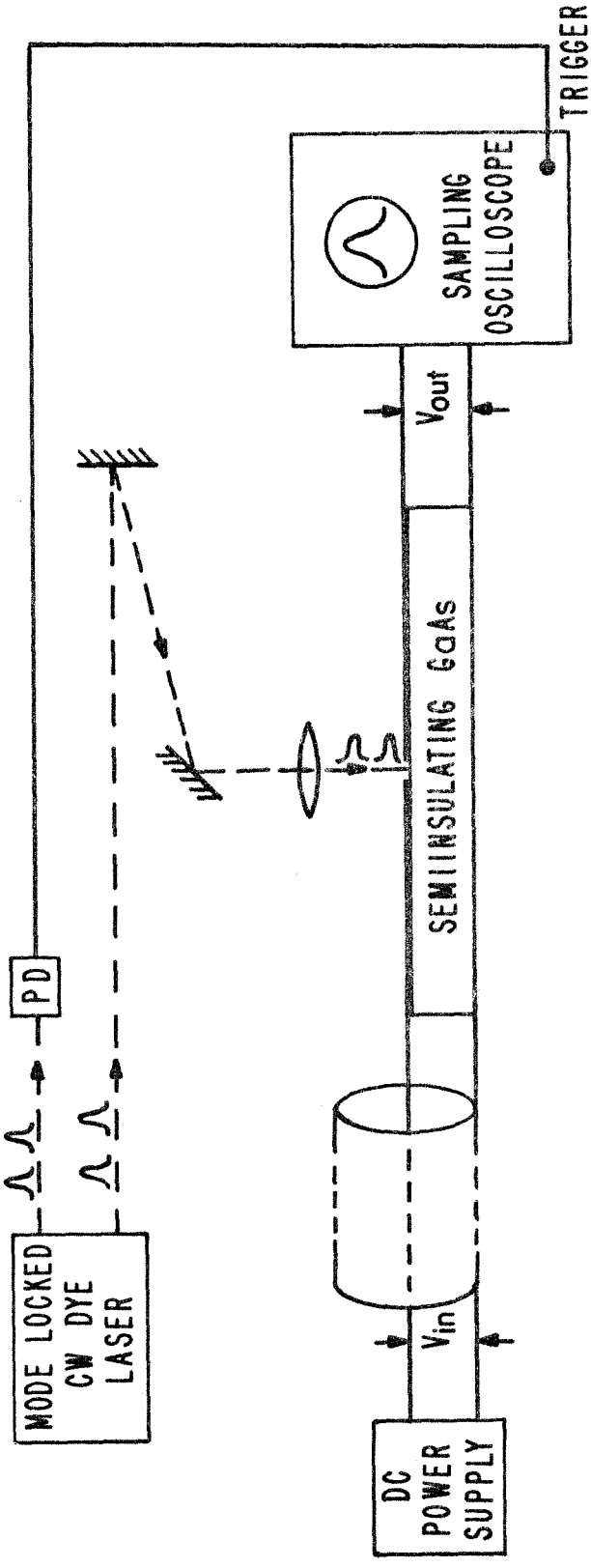

Fig. 7.1.1 Experimental set-up for Cr:GaAs photoconductive impulse response measurements. PD is a fast photodetector. The two pulse trains are mutually synchronized. See text for more details.

electric pulses to propagate in the line at the repetition rate of the optical pulses. The current pulses were detected by the sampling oscilloscope. Because of this switch-like operation, the term "switching unit" will be used to designate the element which consists of the microstrip line with the SI-GaAs at its gap, and the coaxial connectors attached to it.

The oscilloscope used in the experiments was Tektronix 7904/7S11-7T11 with a sampling head S-4 which had a nominal rise time of 25 psec. This oscilloscope had to be triggered about 90 nsec prior to detection. Since a jitter of more than ∿10 ps would affect the observation, it was best to trigger with the same optical pulse which was being detected (the pulse train was not perfectly periodic, as explained in Chapter 2, so that triggering by a previous pulse would not prevent a jitter). In Section 2.6 the acoustooptic dumper was described. It deflected a portion of each internal optical pulse forward, and another portion backward. The backward pulse was used to trigger the sampling oscilloscope, while the forward deflected pulse passed through a 90 nsec optical delay line (in free air) before being focused on the sample by a lens of focal length f = 10 cm. It was possible to change the light spot size and to scan it across the gap. Generally, the spot diameter was big enough to illuminate the whole gap.

7.2 The Various Types of Switching Units

Several methods were employed to connect the Cr:GaAs sample to the circuit. The best temporal resolution was achieved when the semi-

insulator was assembled in a transmission line, bridging a gap in its conductive strip. This package was referred to in the previous section as the "switching unit" (SU). To study the dependence of the current impulse on the electrical circuit, several types of switching units have been studied. Of each type, several units with different parameters and variations in design have been tested. There have been three general types of switching units with fast response. Two are based on the microstrip line and will be referred to as types SUA and SUB, while the third is based on a coaxial transmission line, and will be referred to as type SUC. For purposes of bookkeeping, the switching units are numbered, for instance, SUA-23, SUB-10, etc. The three types of SU's will now be described:

(a) Switching unit of the SUA type

The SI-GaAs was used here as the dielectric filling of the microstrip line, as shown in Figure 7.2.1. Typically, the wafers were of dimension 3 x 1 x 0.036 cm. An Au-Ge conductive strip with a gap was prepared as will be described in Section 7.3. Its width was determined so that the characteristic line impedance was 50Ω, i.e., matched to the input impedance of the sampling oscilloscope. The wafer was then placed on a copper block which, in addition to supporting the SI-GaAs substrate, served as the bottom conductive plane required to complete the microstrip structure. Miniature coaxial connectors designed to operate in the range of dc-18 GHz with maximum voltage standing-wave ratio (VSWR)* of 1.25 [5a]

---

* $\text{VSWR} \equiv \frac{1+|\rho|}{1-|\rho|}$ where ρ is the reflection coefficient.

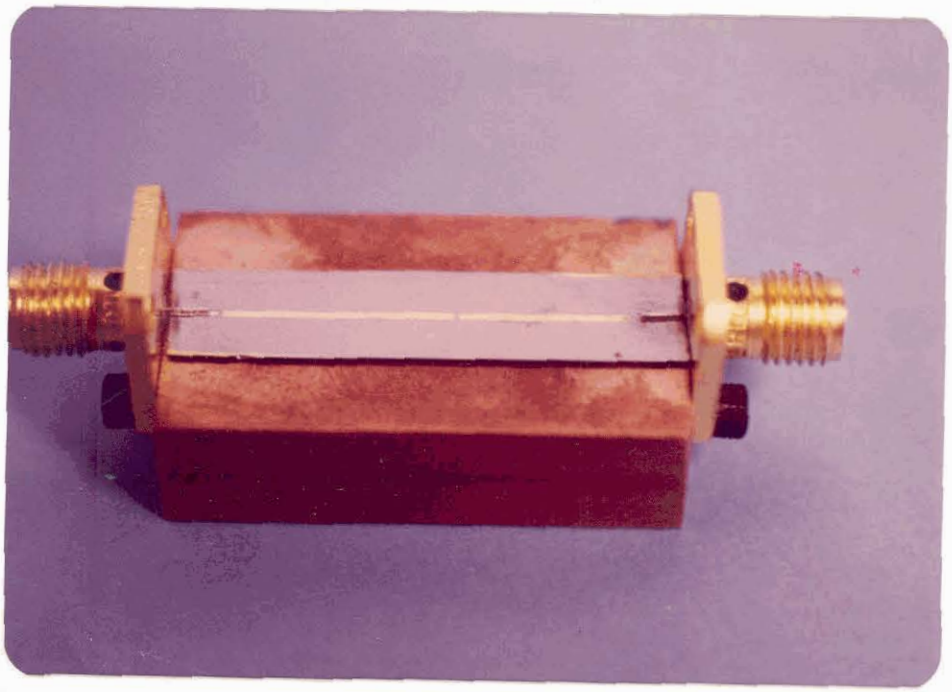

Fig. 7.2.1 Switching unit of SUA type. The copper block is 3 x 1.9 x 1.3 cm. The gap is 400 μm (typically, 100 μm gap was used). More details can be found in the text.

were attached to the copper block. Their inner conductors, which were 0.010" rods, were soldered to the conductive strip on the SI-GaAs wafer. The impedance of the switching unit was tested by a Tektronix time domain reflectometer with 25 ps rise time ($\sim$ 5 mm resolution), and was found to be 50Ω within the impedance resolution of the TDR (see Section 8.1). The gap widths used in the SUA switching units were 70, 100, and 400 μm.

(b) Switching unit of the SUB type

In this type of switching unit, shown in Figure 7.2.2, the SI-GaAs was assembled in a microstrip which had been fabricated from a commercial copper clad substrate with a dielectric filling of polystyrene [6]. The dielectric constant of the polystyrene substrate was 2.54 at 10 GHz, its dissipation factor 0.005, and its thickness 794 $\pm$ 100 μm [6]. For a characteristic impedance of 50μ, it was found empirically that the strip width associated with a dielectric thickness of 794 μm should be 0.188 cm (see Section 8.1). The copper microstrip was prepared photolithographically. Positive photoresist, Shipley 1350J [7] was spin coated on one side while the other was coated with a Q-tip. After conventional exposure to UV light through the appropriate mask, and development of the photoresist (using Shipley MF312 [7]), the exposed copper was etched by a hot aqueous solution of ferric chloride. The the remaining photoresist was removed from both sides. To accommodate the SI-GaAs sample, the copper strip was fabricated with a gap of 1.5 mm. The location of this gap, relative to the distance from the end connectors, varied from one switching unit to another. The samples themselves had pads of Au-Ge, Au-Zn, or Cr as contacts. The pads, which had been prepared photolithographically, were

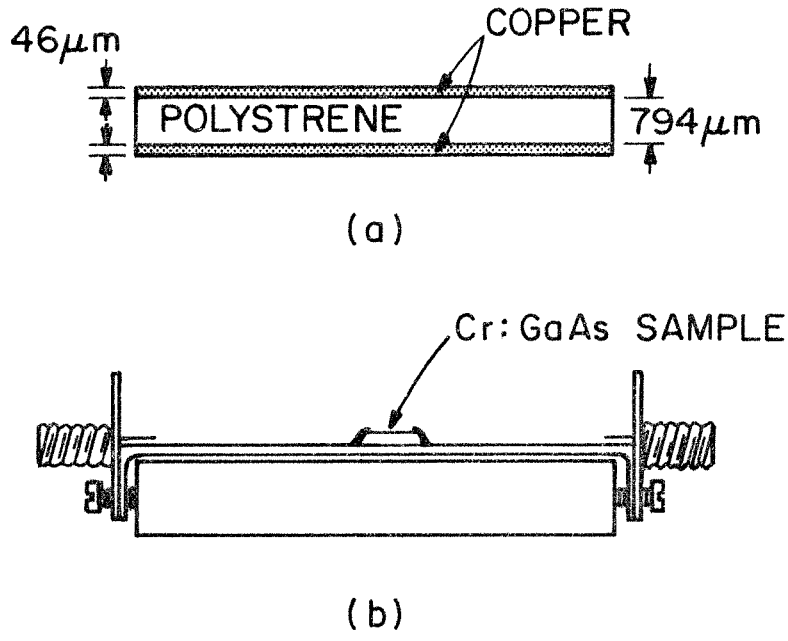

Fig. 7.2.2 A switching unit of type SUB: (a) a cross section along the center of the microstrip, (b) a side view.

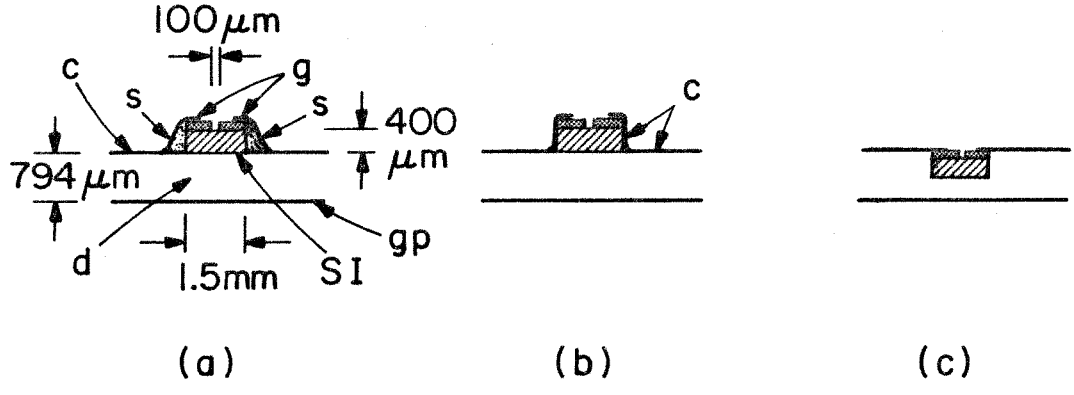

Fig. 7.2.3 Assembly configurations of the Cr:GaAs sample in switching unit SUB: (a) The exposed, (b) the covered, and (c) the buried sample. SI = Cr:GaAs sample, g = gold pads (contacts), c = copper strip, gp = ground plane, d = dielectric filling, and s = solder or conductive epoxy.

separated by 100 μm from each other, and were soldered to the copper line bridging the gap in the conductive strip. The three structures shown in Figure 7.2.3 yielded similar results. Therefore, the switching units of type SUB reported in what follows are, with one exception, of the exposed type (Figure 7.2.3a). The microstrip was supported by a copper or lucite block to which miniature coaxial connectors [5b] were attached. The specifications of these connectors were similar to those used in the SUA switching units. To ensure good contact between the connectors and the ground plane of the microstrip, the ends of the lower copper sheet were folded over the copper block (see Figure 7.2.2b).

(c) Switching unit of the SUC type

This switching unit followed the design of a fast photodiode package [8]. Its exploded diagram is shown in Figure 7.2.4. The Cr:GaAs switching element was connected at one side of the gap to the tip of a miniature coaxial connector [5c] and at the other side to the package [9].

7.3 Sample Preparation

Wafers of semi-insulating Cr:GaAs were purchased from Crystal Specialties, Inc. [10] or received from the Naval Research Laboratories [11]. The wafers had been cut along the (100) crystallographic plane to a thickness of about 400 μm and were mechanically polished. Contacts of Au-Ge, Au-Zn, or Cr were evaporated on the samples. Immediately before evaporation the wafer had been cleaved to size and cleaned thoroughly by acetone, methanol, isopropanol, and HCl or H_2SO_4. During the evaporation, which was performed at 5×10^{-7} torr, layers of the contact material ~ 7000Å were deposited. The conductive strips, in the case of SUA, and the

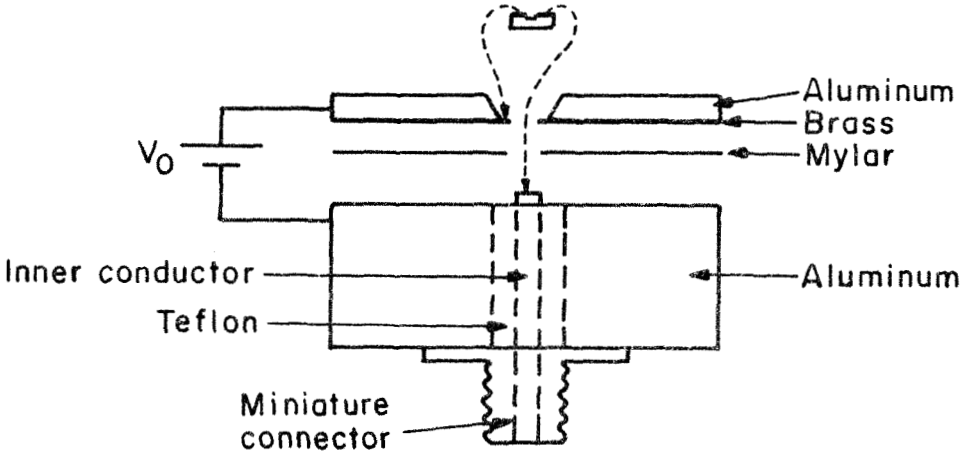

Fig. 7.2.4 Switching unit of type SUC.

conductive pads, in the case of SUB and SUC, were prepared photolithographically, using positive photoresist (Shipley 1350J [7]) and metal-free developer (Shipley MF-312 [7]). When Au-Ge or Au-Zn were used as contacts, the unwanted gold was etched away by a solution of $KI:I_2:H_2O$ = 275:15:250. When Cr was used, the strips were prepared by a lift-off method. The contacts were alloyed in a hydrogenic environment. The Au-Ge contacts were alloyed at 410°C and the Au-Zn at 500°C, typically for 15 seconds, although longer alloying periods were tested too. The Cr contacts were not alloyed.

After being alloyed, the Au-Ge showed relatively high resistance about 10Ω per mm length (corresponds to 2×10^{-4}Ω-cm, which is 100 times the resistivity of pure gold). Its thickness was measured by a Sloan Dektak instrument to be ∿7000Å. This is about 1-1/2 times the penetration depth of pure gold, so that the relatively high resistivity was attributed to the impurity of the Au-Ge. Consequently, another layer of pure gold (99%) was evaporated on top of the Au-Ge, immediately after its evaporation. The resistance of the Au-Ge/Au strip then dropped to less than 2Ω/mm.

7.4 Experimental Results

Two typical oscilloscope displays of the response of the electric circuit to picosecond light illumination of the Cr:GaAs are shown in Figure 7.4.1. The rise time (10-90%) in both is about 25 ps, and the fall time (1/e of the peak) is about 75 ps. The "kink" at the decay is at about 7/10 of the peak.

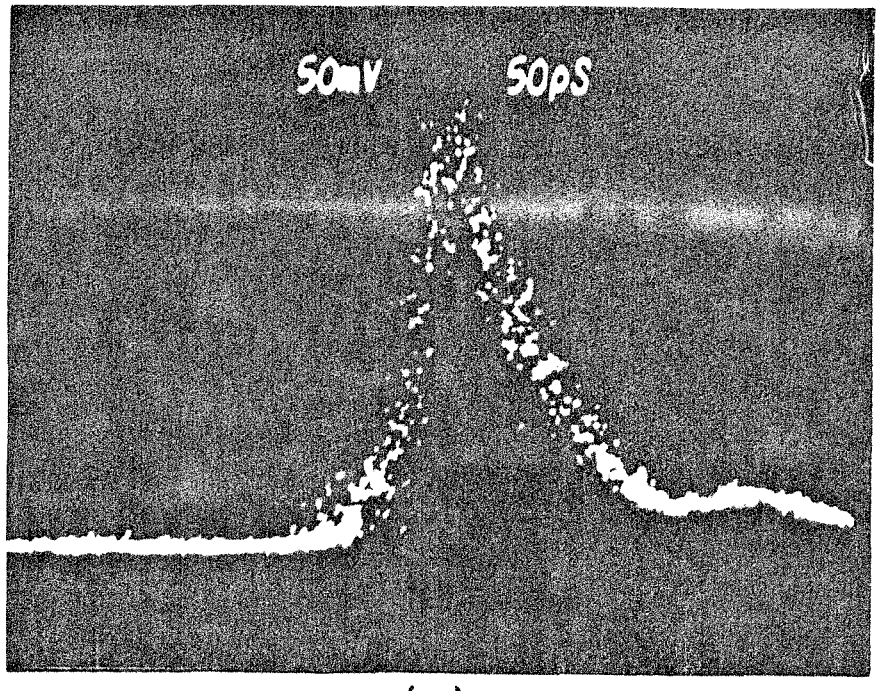

(a)

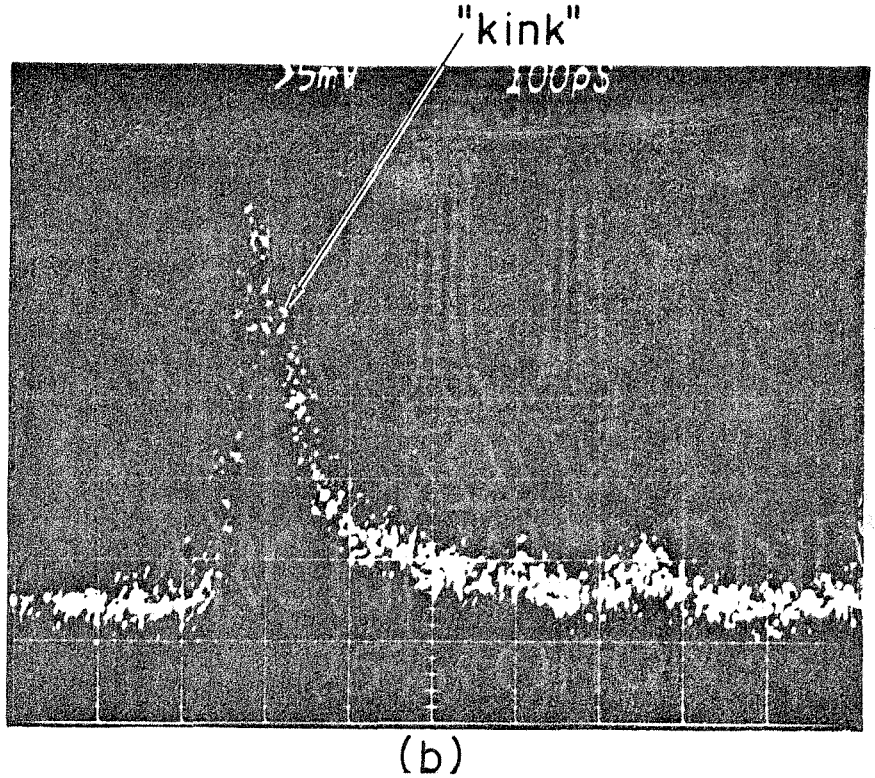

(b)

Fig. 7.4.1 Typical oscilloscope displays of the switching unit response to a picosecond pulse illumination (λ=6100 Å) of the Cr:GaAs.

Fourteen switching units are listed in Table I. Various samples of Cr:GaAs have been investigated. "Standard" means the regular Cr:GaAs as purchased from Crystal Specialties, Inc. [10], while "high doped" indicates samples with higher Cr concentration than "standard" [10b]. More details on this classification will be given in Chapter 9. "NRL" is a sample received from the Naval Research Laboratories [11].

The transmission is defined here as the ratio between the peak voltage displayed on the oscilloscope to the applied dc voltage. When marked by "low," the transmission is below 0.1%. Notice, though, that in studying the photoconductive impulse response the efforts were channeled toward improving the temporal resolution rather than increasing the transmission. The transmission depends on the level of excitation, the quality of the contacts, and the gap length.

The "kink" shown in Figure 7.4.1b has been observed in the impulse response of the switching units which are marked by (x).

The extinction of the switching unit was measured to be at least $1:10^5$ (dark dc current:peak photocurrent), and calculated to be $1:10^7$ at the excitation levels used in the experiment (see Section 7.1).

Table 1

Switch Number	Strip Width	Cr:GaAs Sample	Contact Material	Gap (μm)	Trans-mission	1/e Fall Time (psec)	Kink
SUA-14	356 μm	standard	Au-Ge/Au	100	1-1/2%	60	x
SUA-14a	356 μm	standard	Au-Ge/Au	100	2%	75	x ?
SUA-18	356 μm	standard	Au-Ge/Au	400	0.1%	75	x
SUA-23	356 μm	standard	Au-Ge/Au	100	1%	75	x
SUA-25	356 μm	NRL	Au-Ge/Au	100	1%	75	x ?
SUB-1	1.88 mm	high doped	Au-Zn[a)]	80	low	150	
SUB-2	2.06 mm	standard	Au-Ge[a)]	100	2%	120	
SUB-3	1.73 mm	standard	Cr[a)]	80	1%	100	
SUB-4	2.06 mm	standard	Au-Zn[a)]	100	low	75	x
SUB-5	2.06 mm	standard	Au-Zn[a)]	100	low	100	x
SUB-6	1.88 mm	high doped	Au-Zn[a)]	80	1%	75	x
SUB-8[d)]	2.06 mm	standard	Au-Zn[a)]	100	0.3%	75	x
SUB-9	1.88 mm	standard	Au-Zn[b)]	100	0.1%	70	
SUC-17	coaxial	standard	Au-Ge[c)]	80	1%	90	

[a)] Soldered to the copper strip by an indalloy solder Indium: 90%, Silver: 10% [12].

[b)] Connected to the copper strip by gold epoxy

[c)] Connected to the switching unit by silver epoxy

[d)] Same as SUB-5 but of the buried switching element type (see Figure 7.2.3).

Chapter 8

DEDUCTION OF THE PHOTOCONDUCTIVE IMPULSE RESPONSE OF Cr:GaAs FROM THE EXPERIMENTAL RESULTS

8.0 Introduction

In Chapter 7 the results of the Cr:GaAs photoconductivity experiment have been presented. The observed impulse (Figure 7.4.1) does not exactly correspond to the photoconductive impulse response of the Cr:GaAs sample which we wish to investigate. It is, rather, a convolution of the current pulse which results from the change in the gap conductivity after the picosecond illumination and the impulse response of the oscilloscope. To deduce the temporal behavior of the Cr:GaAs conductivity from the observed impulse, we must first ensure that the current pulses are not distorted while propagating along the transmission line from the gap in the switching unit to the oscilliscope. Such distortion can be a result of reflections from impedance discontinuities and dispersive broadening of the pulses.

We start this chapter by showing that reflections and dispersive effects have been minimized and do not affect the profile of the detected current pulses. Following that, the oscilloscope display is deconvolved and the photocurrent pulses are analyzed so as to determine the photoconductive impulse response of our Cr:GaAs samples. At the end of the chapter, the observed photoconductance of the gap is compared with its theoretical value, calculated from bulk conductivity parameters of Cr:GaAs.

8.1 Impedance Matching of a Microstrip Line

The transmission line chosen for the transient photoconductivity experiments was the microstrip line. A microstrip consists of a strip conductor and a ground plane, separated by a dielectric medium, as shown in Figure 8.1.1. In the figure, ε is the dielectric constant of the substrate, h is the substrate thickness, w is the width of the strip conductor, and t is its thickness. It is relatively easy to fabricate, as the substrate can be wide and only the upper surface requires special photolithographic (or other) treatment. Other types of transmission line which might have been used are the stripline (Figure 8.1.2) and the coaxial line. They are more difficult to fabricate as we need access for the light to illuminate the sample at the line gap, while no significant advantage is gained by using them. Their isolation from neighboring circuits is better than in a microstrip, but this is not an important factor in the present experiment.

Field lines of a microstrip are shown in Figure 8.1.3. Although not all of them are entirely contained within the substrate, and therefore the propagating modes are not purely TEM, quasi-TEM modes are considered in analyzing the microstrip characteristics. In reality, the modes are hybrid. At high frequencies, modes in the form of surface waves and transverse resonances are excited [13]. The surface waves are TM and TE modes which propagate across a dielectric substrate

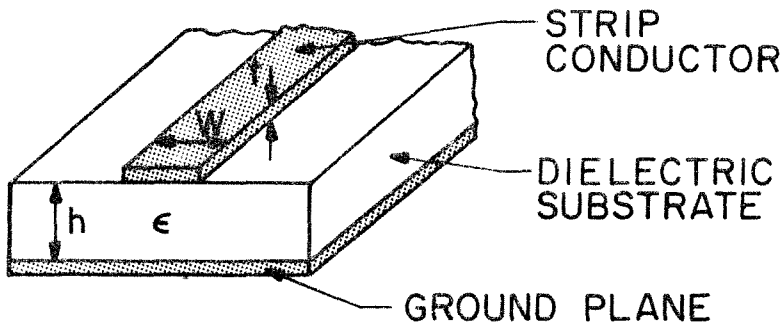

Fig. 8.1.1 A microstrip line.

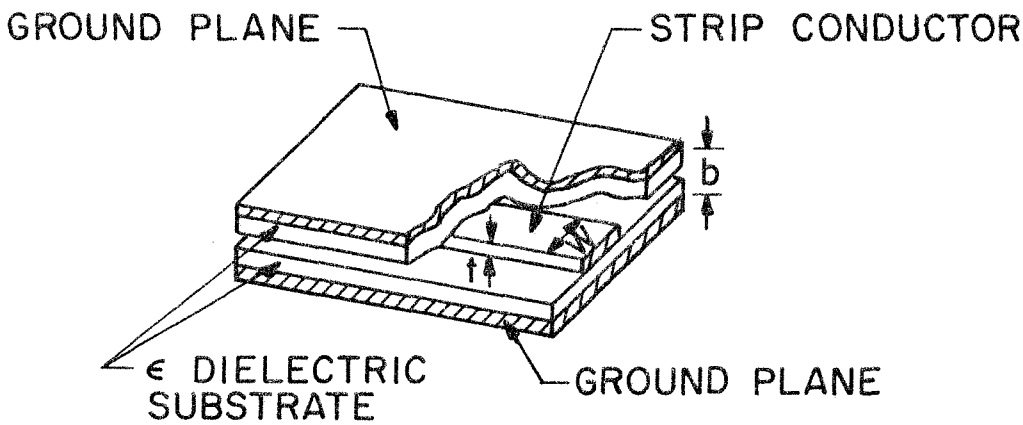

Fig. 8.1.2 A stripline.

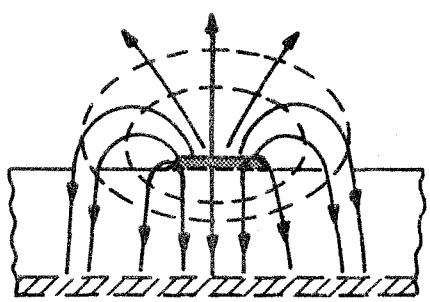

Fig. 8.1.3 Field lines of a microstrip.

with a ground plane. Significant coupling between the quasi-TEM and the surface wave modes occurs above the frequency [14].

$$f_s = \frac{c}{2\pi h}\sqrt{\frac{2}{\varepsilon-1}}\tan^{-1}\varepsilon \qquad (8.1.1)$$

in which c is the speed of light and ε and h are as in Figure 8.1.1. For the microstrips in our experiment, $f_s > 75$ GHz. Since the oscilloscope bandwidth is 13.7 GHz at 3 db, we may assume that only quasi-TEM modes are effective in our measurements.

The most important parameter of the transmission line is its characteristic impedance. For a given substrate, i.e., dielectric constant, ε, and thickness, h, and for a given conductor thickness, t, the impedance depends on the strip width w. To date, there are no exact closed-form formulas for this dependence, and only approximate expressions have been published. These expressions are compared with each other in Figure 8.1.4, where the ratio of strip width to substrate thickness is plotted as a function of the characteristic microstrip impedance. The two dielectric constants used in the calculations correspond to the substrates of switching units SUA [19] and SUB [6], respectively, at f = 10 GHz (see Section 7.2).

Since each formula results in a different value for w/h for a given z, none of them can be used without being first compared with experimental measurements. To do that, microstrips similar to those used in our experiment, but without a gap, were prepared with different strip widths. Their impedance was determined by a Tektronix 7S12 time domain reflectometer (TDR) with a rise time of 25 psec (i.e., a spatial

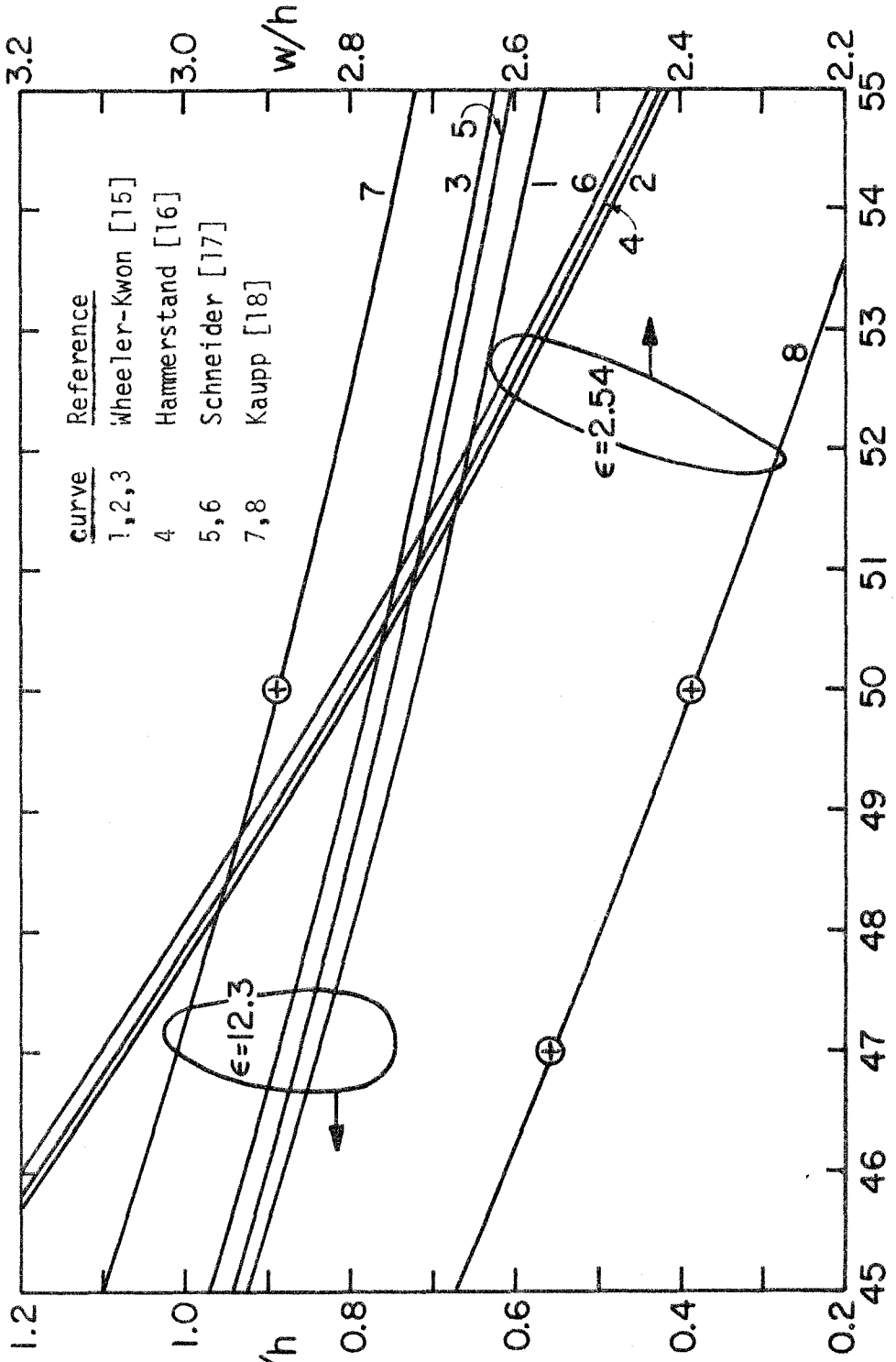

Fig. 8.1.4 Stripwidth to substrate thickness ratio as a function of the characteristic microstrip impedance, calculated from various dispersionless analytical expressions, for zero conductive strip thickness and ε=12.3 (GaAs) and ε=2.54 (Polystrene). The circled marks are our experimental results.

resolution of about 5 mm). The microstrips were connected on one side to the 50Ω exit of the TDR and on the other to a 50Ω termination.

Figure 8.1.5 shows TDR measurement results of three microstrips of the SUB type. The horizontal axis is the distance along the line and the vertical axis is equivalent to the reflection coefficient. The line with the strip width of 0.188 cm is of 50Ω impedance within the instrumental resolution. The discontinuities in the impedance at the connectors determines their VSWR (see footnote in Section 7.2) to be 1.03, while that of the termination is 1.01. Both values are within the manufacturer's specifications [5b],[20]. Similar measurements were done on switching units of the SUA type, as shown in Figure 8.1.6. To obtain 50Ω characteristic impedance, with Cr:GaAs substrate thickness of 400 μm, the strip width had to be 356 μm.

The results of the TDR measurements are marked in Figure 8.1.4, from which it is obvious that they best fit Kaupp's empirical formula [18]

$$\frac{w}{h} = 1.25\left[\frac{5.97}{\exp(Z\sqrt{\varepsilon+1.41}/87)} - \frac{t}{h}\right) \qquad (8.1.2)$$

(for notations, refer to Figure 8.1.1). An effective dielectric constant can be defined by

$$Z = \frac{Z_o}{\sqrt{\varepsilon_{eff}}} \qquad (8.1.3)$$

*The basic operation of a TDR is to send a voltage pulse along the line, and to consequently detect its reflection resulting from discontinuities in the line impedance.

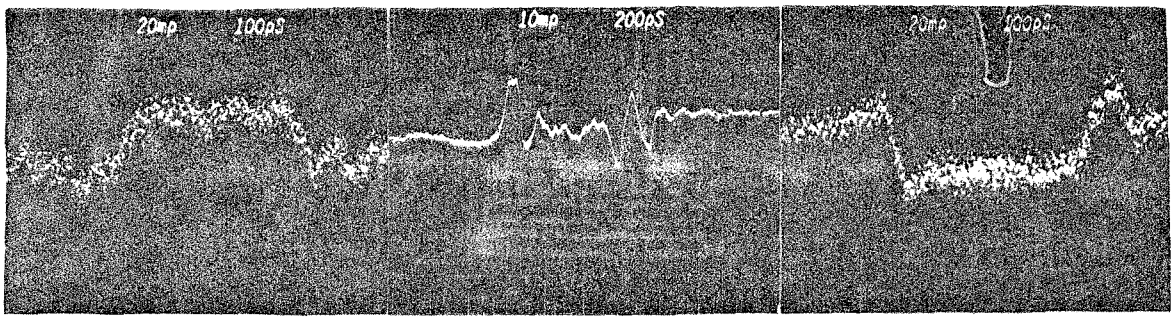

w = 1.63mm
z = 53Ω

w = 1.88mm
z = 50Ω

w = 2.03mm
z = 47Ω

Fig. 8.1.5 Power reflection (vertical axis) from impedance discontinuities along a wave guide which consists of 50Ω lines connected to both sides of a microstrip of type SUB. The transitions occur at the connectors.

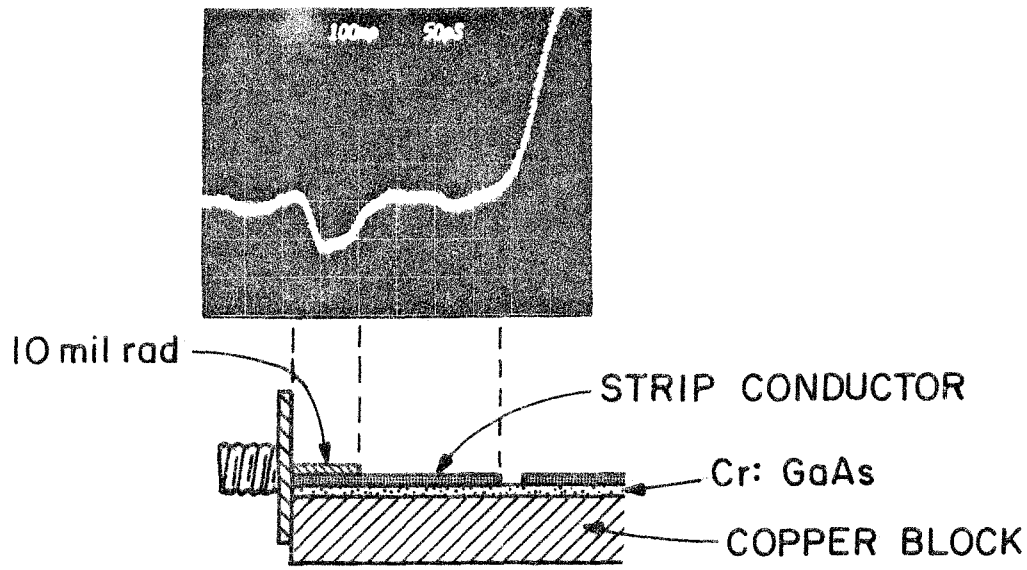

Fig. 8.1.6 Oscilloscope display of impedance discontinuities in a switching unit of type SUA, measured by a TDR. The microstrip is connected on the left to a 50Ω line.

where the subscript "o" denotes a microstrip with an air substrate. Kaupp's expression for ε_{eff} is

$$\varepsilon_{eff} = 0.475\varepsilon + 0.67 \tag{8.1.4}$$

The formulas plotted in Figure 8.1.4 do not take into account any dispersion effect other than the dielectric constant dependence on frequency. However, at high frequencies the effective dielectric constant, defined in (8.1.3), has an additional frequency dependence [21],[13], and therefore the characteristic impedance is more dispersive. The frequency spectrum of the photocurrent pulses can be roughly found by assuming the pulses to follow a step exponential decay function

$$i(t) = \begin{cases} 0 & t < 0 \\ e^{-t/\tau_\ell} & t > 0 \end{cases} \tag{8.1.5}$$

It will be shown (section 8.4) that $\tau_\ell \simeq 70$ psec, therefore the 3 db frequency of the pulse spectrum is $\sim$2.3 GHz. The frequency spectum extends from dc to infinity, but frequencies higher than the 3 db frequency of the oscilloscope, i.e., 13.7 GHz, can be considered ineffective in our measurements. The impedance dependence on frequency can be neglected for frequencies below [19]

$$f_o(\text{GHz}) = \frac{0.3}{(\varepsilon-1)^{1/4}} \sqrt{Z/h} \qquad (h \text{ in cm}) \tag{8.1.6}$$

For both SUA and SUB types of switching units, this frequency is $\sim$6 GHz, which is in the range of frequencies involved in our experiment. Therefore, the effect of dispersion on the impedance must be considered. Two formulas

for $\varepsilon_{eff}(f)$ were found in the literature: In Ref.[21], for $f > f_0$,

$$\varepsilon_{eff}(f) = 1.2 \times 10^{-3}(\varepsilon^2-1)\sqrt{Z \cdot h \cdot w}\,(f-f_0) + \varepsilon_{eff_0} \qquad (8.1.7)$$

and in Ref. [22]

$$\varepsilon_{eff}(f) = \varepsilon - \frac{\varepsilon - \varepsilon_{eff_0}}{1 + G(f/f_1)} \qquad (8.1.8)$$

where $f_1 = Z/8\pi h$ and $G = 0.6 + 0.009Z$. In these formulas f, f_0 , and f_1 are in GHz, and h and w (see Figure 8.1.1) are in cm. Calculated from (8.1.6) and (8.1.7), $\varepsilon_{eff}/\varepsilon$ is plotted in Figure 8.1.7 against f/f_1 . The shaded area is the frequency band involved in the experiment. (For switching unit of the SUA type, f_1 = 50 GHz, while for SUB, f_1 = 25 GHz). From these formulas and from (8.1.3) and (8.1.4) the error in computing Z at low frequency rather than, for instance, 14 GHz is only $\sim$-3% for both types of switching units.

It should be noted that when dispersion is taken into account while calculating the formulas plotted in Figure 8.1.4, none of them agree well with the TDR measurements.

A consequence of the discussion in this section is that it is difficult to eliminate entirely the impedance discontinuities. Therefore, the gap in the microstrip, with the semi-insulating GaAs in it, was placed far from the connectors, so as to avoid an overlap between the main pulse and its reflections.

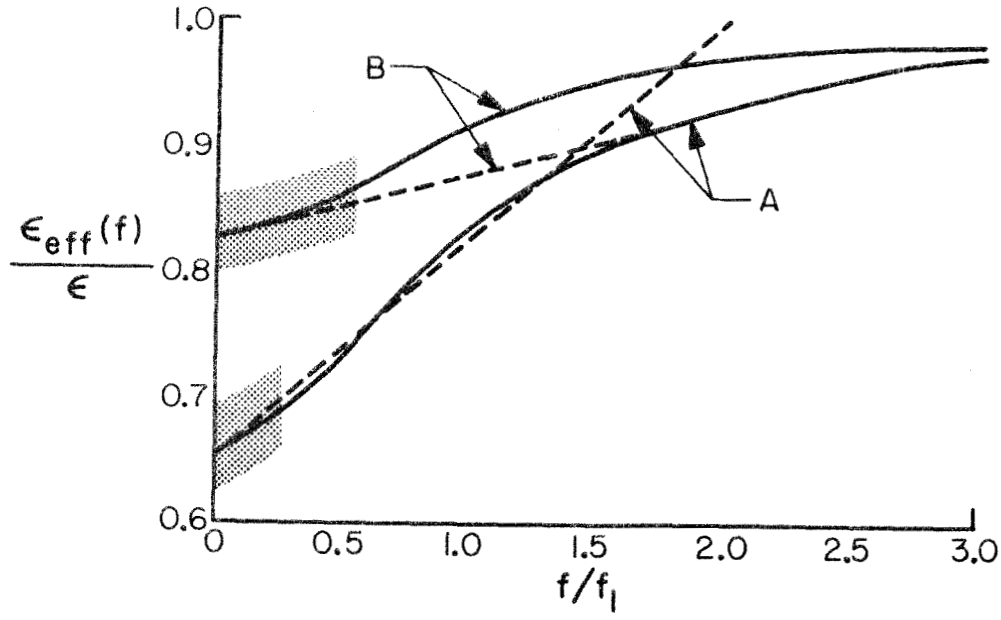

Fig. 8.1.7 The effective dielectric constant dependence on frequency, for microstrips of type SUA (curve A, $\varepsilon = 12.3$, $f_1 = 50$ GHz), and SUB (curve B, $\varepsilon = 2.54$, $f_1 = 25$ GHz). The shaded area indicates the frequency band effective in our experiment.

8.2 The Effect of Pulse Broadening in the Microstrip on the Observed Impulse

When propagating along a microstrip line, the current pulse profile might be distorted as a result of a dispersive group velocity and frequency dependent losses. This effect must be minimized if the photocarrier lifetime of the Cr:GaAs sample is to be deduced from the observed impulse (Figure 7.4.1).

Consider first the group velocity. Assume a pulse with an initial spatial width Δx_o and a variation Δv_g of the group velocity across its frequency band. At time t, the spatial width of the pulse can be approximated by [23]

$$\Delta x(t) = \sqrt{(\Delta x_o)^2 + (\Delta v_g t)^2} \tag{8.2.1}$$

For a transform-limited pulse,

$$\Delta v_g \simeq \frac{d^2\omega}{dk^2}\Delta k \simeq \frac{d^2\omega}{dk^2}\frac{1}{\Delta x_o} \tag{8.2.2}$$

so that

$$\Delta x(t) = \sqrt{(\Delta x_o)^2 + (\frac{d^2\omega}{dk^2}\frac{t}{\Delta x_o})^2} \tag{8.2.3}$$

For practical use, we translate time into distance by $z = tc/n(\omega)$ and define a distance z_d by equating the two terms under the square root in (8.2.3),

$$z_d \equiv \frac{c}{n(\omega)}\frac{(\Delta x_o)^2}{(d^2\omega/dk^2)} \tag{8.2.4}$$

Dispersive broadening of a pulse, propagating a distance z, can be

neglected if $z \ll z_d$. To calculate z_d we differentiate

$$\omega = \frac{c}{n(\omega)} k \tag{8.2.5}$$

which gives

$$\frac{d^2\omega}{dk^2} = - \frac{c^2[2 \frac{dn(\omega)}{d\omega} + \omega \frac{d^2n}{d\omega^2}]}{[n(\omega) + \omega \frac{dn(\omega)}{d\omega}]^3} \tag{8.2.6}$$

We can estimate $d^2\omega/dk^2$ from (8.2.6) by using the dispersion relations given in the previous section for $\varepsilon_{eff}(f)$. For instance, at 14 GHz, which is about the 3 db frequency of our oscilloscope, (8.1.6) and (8.2.4)-(8.2.6) give z_d = 30 cm for a switching unit of the SUA type, and z_d = 124 cm for SUB. Since in our experiment the travel distance between the Cr:GaAs sample and the input of the sampling oscilloscope was shorter than 4 cm, pulse broadening due to dispersive group velocity could be neglected.

Consider now pulse broadening due to the dependence of the loss on the frequency. This effect can be estimated with the aid of an expression for the conductor loss derived by Pucel et al. [24]

$$\alpha_c = \frac{R_s}{Zh} F(h,w,t) \tag{8.2.7}$$

where R_s is the surface conductivity, given by

$$R_s = \sqrt{\frac{\pi\mu_o}{\sigma} f} \tag{8.2.8}$$

in which μ_o is the permeability of free space, and σ is the material conductivity. The other variables in (8.2.7) are defined in Figure 8.1.1. The function F(h,w,t) is given in Ref. [24].

For the two types of switching units we find

$$\alpha_c(\text{SUA}) = 3.7 \times 10^{-2} \sqrt{f} \text{ dB/cm} \tag{8.2.9}$$

and

$$\alpha_c(\text{SUB}) = 1.9 \times 10^{-2} \sqrt{f} \text{ dB/cm} \tag{8.2.10}$$

where f is GHz. Consequently, for the distances involved in SUA (1.5 cm) and SUB (4 cm), both have about the same ohmic loss. To estimate the effect on the pulse width, we compare the losses at 2 GHz and 14 GHz which are about the 3 db frequencies of the photocurrent pulse and of the oscilloscope, respectively (see Section 8.1). In a switching unit of type SUA the ohmic loss after 1.5 cm is 1.8% at 2 GHz and 4.7% at 14 GHz. In a switching unit of type SUB the ohmic loss after 4 cm is 2.4% at 2 GHz and 6.3% at 14 GHz. These differences are small, and therefore pulse broadening due to ohmic losses will be neglected.

Another source of losses is the dielectric substrate. This loss is given by [25],[26]

$$\alpha_d = 27.3 \frac{\varepsilon}{\sqrt{\varepsilon_{eff}}} \frac{\varepsilon_{eff} - 1}{\varepsilon - 1} \frac{\tan \delta}{\lambda_o} \text{ dB/cm} \tag{8.2.11}$$

in which λ_o is the wavelength in free space, and $\tan \delta$ is the loss factor of the dielectric. At low frequencies the dielectric loss is estimated to be 10^{-5} dB/cm for SUA and 4×10^{-3} dB/cm for SUB, so that it can be neglected in comparison to the ohmic loss (note that $\tan \delta = \frac{\sigma}{\omega\varepsilon} \propto \lambda_o$, so that α_d depends on frequency through ε only).

8.3 The Effect of the RC Time of the Gap in the Microstrip on the Observed Impulse

The ohmic resistance and the capacitive coupling across the gap in the microstrip line limit the response rise time of the switching unit (see Section 7.2), and thus may affect the observed current impulse. In this section we investigate the effect of this RC time on the electric circuit response, so as to enable us to deduce the actual photoconductive impulse response of the studied Cr:GaAs sample.

The gaps used in our experiment have widths of 80, 100, and 400μm and are thus much shorter than the voltage wavelengths involved. Therefore, they are considered as discontinuities rather than guiding sections of the transmission line. The gap capacitance depends on the gap width and length, and on the dielectric constant [27]-[29]. Its value is found to be [27] ∿0.02 pf for the 100 μm gaps and ∿0.005 pf for the 400 μm gap.

The response of the microstrip to a current impulse originating at the gap, as is the case in our experiment, cannot be trivially found by multiplying the gap resistance by its capacitance. Instead, a circuit equivalent to the microstrip segment in the immediate vicinity of the gap will be introduced and its response to a time varying conductance will be analyzed. Let us first consider an ideal transmission line with an ideal switch, as shown in Figure 8.3.1. As long as the switch is open, the line preceding it is charged up to the applied dc voltage, V_0. When the switch is closed, the line is discharged and voltage wave fronts start traveling in the two opposite directions. Denote the voltage next to the switch on its two respective sides as V_+ and V_- (see Figure 8.3.1b),

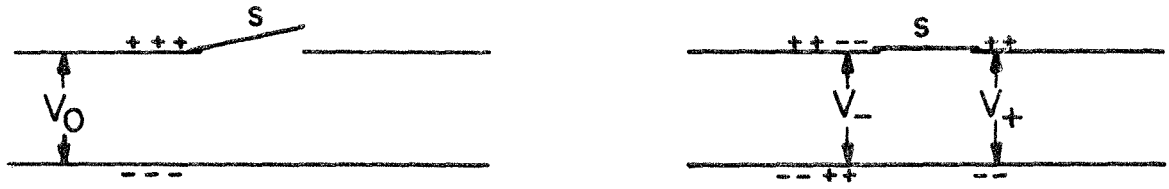

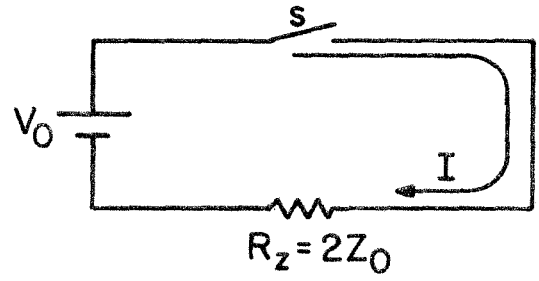

Fig. 8.3.1 An ideal transmission line with an open (a) and closed (b) switch. Its equivalent circuit is shown in (c).

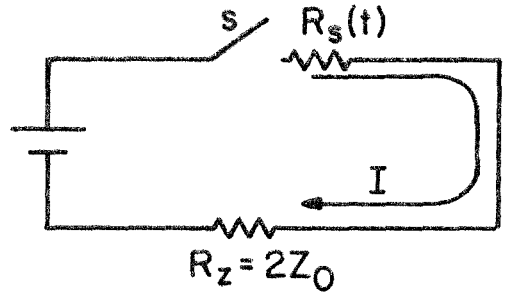

Fig. 8.3.2 An equivalent circuit of the gap in the conductive strip of the switching unit when only its ohmic resistance is considered.

then immediately after the ideal switch is closed $V_o + V_- = V_+$, or

$$V_o = V_+ - V_- \tag{8.3.1}$$

The resulting current is equal on both sides of the switch, i.e.,

$$I \equiv I_+ = I_- \tag{8.3.2}$$

so that, by using $I_+ = V_+/Z_o$ and $I_- = -V_-/Z_o$ [30], where Z_o is the transmission line characteristic impedance

$$V_+ = -V_- = V_o/2 \tag{8.3.3}$$

and

$$I = V_o/2Z_o \tag{8.3.4}$$

If the transmission line is infinite, or if it is properly terminated on both sides, this current will flow through the ideal switch forever. The same current will flow for the same applied dc voltage in a circuit with a series resistance $R_z = 2Z_o$, shown in Figure 8.3.1c.

We now wish to replace the ideal switch by an element which is equivalent to the gap in the microstrip. If one simply assumes that all the current flows through the semi-insulator, then the equivalent element is a variable resistor, $R_s(t)$, and the equivalent circuit is as shown in Figure 8.3.2. The current is then given by

$$I = \frac{V_o}{R_s(t) + 2Z_o} \tag{8.3.5}$$

However, this equivalent circuit ignores the capacitive coupling across the gap, which becomes significant when high Fourier frequencies are

excited. At these frequencies, a portion of the current passes the gap without flowing through the ohmic resistance of the semi-insulator. Therefore, the appropriate equivalent element must consist of a resistance connected in series to an ideal switch, and both connected in parallel to a capacitor [31]. The equivalent circuit is shown in Figure 8.3.3.

Let us denote the voltage between the capacitor plates by V_c, and the capacitor charge immediately prior to illumination by Q_o. If the switch S is closed at $t = 0$, then at $t < 0$

$$V_c = V_o \tag{8.3.6a}$$

$$Q_o = CV_o \tag{8.3.6b}$$

$$i_1 = i_2 = 0 \tag{8.3.6c}$$

while at $t \geq 0$,

$$V_c = R_s(t)\, i_2 \tag{8.3.6d}$$

$$V_o = i_2 R_s(t) + (i_1+i_2)R_z \tag{8.3.6e}$$

$$Q = CV_c \tag{8.3.6f}$$

Therefore, at $t \geq 0$ the current in the line is

$$I_\ell(t) = i_1(t) + i_2(t) = \frac{V_o - i_2(t)\, R_s(t)}{R_z} \tag{8.3.7}$$

so that to determine $I_\ell(t)$, we solve first for $i_2(t)$. Differentiating

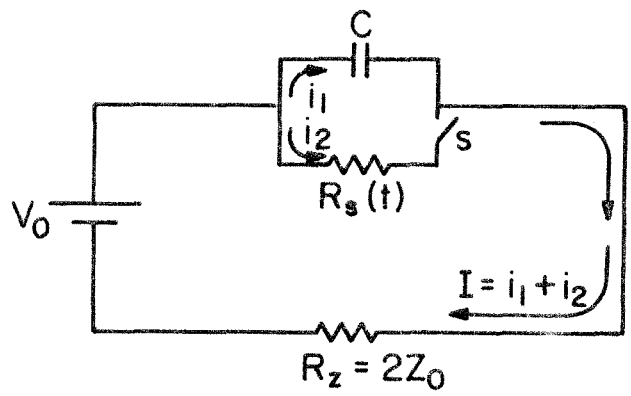

Fig. 8.3.3 The equivalent circuit of the gap in the conductive strip of the switching unit, when both its ohmic resistance and capacitance coupling are considered.

(8.3.8d) and (8.3.8f) with respect to t ($t \geq 0$), and eliminating dV_c/dt from the two equations gives

$$R_s(t)\frac{di_2}{dt} + i_2\frac{dR_s(t)}{dt} = \frac{i_1}{C} \tag{8.3.8}$$

where we used $i_1 = dQ/dt$. Substituting i_1 as given by (8.3.7) gives a general differential equation for i_2:

$$\frac{di_2}{dt} + i_2\left[\frac{dR_s(t)/dt}{R_s(t)} + \frac{1}{R_zC} + \frac{1}{R_s(t)C}\right] = \frac{V_o}{CR_zR_s(t)} \tag{8.3.9}$$

To solve (8.3.9), an analytic expression of $R_s(t)$ is required. Since the observed impulse response in Figure 7.4.1a has a rise time comparable to that of the oscilloscope, and its decay is close to an exponential, we chose a simple model of a step exponential decay for the conductivity of the gap, i.e.,

$$\sigma(t) = \begin{cases} \sigma_o & t < 0 \\ \sigma_o + \sigma_1 e^{-t/\tau_c} & t \geq 0 \end{cases} \tag{8.3.10}$$

which defines σ_o, σ_1, and τ_c. This model will be discussed at the end of this chapter. Since $\sigma_o \simeq 10^{-8}$ mho-cm^{-1} and $\sigma_1 \simeq 5$ mho-cm^{-1}, so that $\sigma_1 e^{-t/\tau_c} >> \sigma_o$ as long as $t < 20\ \tau_c$, we may approximate $R_s(t)$ by

$$R_s(t) = R_o e^{t/\tau_c} \tag{8.3.11}$$

where $R_o = \ell/\sigma_1 A$. Here, ℓ is the gap length and A is the cross sectional area near the surface of the semi-insulator, through which the

photocurrent flows. Substituting (8.3.11) in (8.3.9) gives

$$\frac{di_2}{dt} + i_2\left[\frac{1}{\tau_c} + \frac{1}{R_z C} + \frac{e^{-t/\tau_c}}{R_o C}\right] = \frac{V_o}{CR_z R_o} e^{-t/\tau_c} \tag{8.3.12}$$

This equation is solved in Appendix A. From equations (A.13) and (8.3.7), the line current is found to be

$$\begin{aligned} I_\ell(t) = {} & \frac{V_o}{R_z}\left\{1 - \exp\left[-\frac{\tau_c}{R_o C}\left(1 - e^{-t/\tau_c}\right) - \frac{t}{R_z C}\right]\right. \\ & - \frac{\tau_c}{R_z C}\left(\frac{\tau_c}{R_o C}\right)^{\tau_c/R_z C} \exp\left(\frac{\tau_c}{R_o C} e^{-t/\tau_c} - \frac{t}{R_z C}\right) \\ & \left. \times \left[\Gamma\left(-\frac{\tau_c}{R_z C}, \frac{\tau_c}{R_o C} e^{-t/\tau_c}\right) - \Gamma\left(-\frac{\tau_c}{R_z C}, \frac{\tau_c}{R_o C}\right)\right]\right\} \end{aligned} \tag{8.3.13}$$

where $\Gamma(a,x)$ is the incomplete Γ function defined by:

$$\Gamma(a,x) = \int_x^\infty e^{-t}\, t^{a-1}\, dt \tag{8.3.14}$$

The response of the microstrip line to the exponential decay photoconductive impulse response is shown in Figure 8.4.1b. More details regarding this figure will be given in the next section.

The gap resistance immediately after illumination can be determined from the maximum line current, $(I_\ell)_{max}$. In Appendix A it is shown that

$$(I_\ell)_{max} = \frac{V_o}{R_o e^{t_{m1}/\tau_c} + R_z} = \frac{V_o}{R_o e^{t_{m1}/\tau_c} + 2Z_o} \tag{8.3.15}$$

where t_{m1} is defined by

$$I_\ell(t_{ml}) = (I_\ell)_{max} \tag{8.3.16}$$

Note that the maximum line current found from (8.3.5), where no capacitive coupling across the gap is assumed, is approximately equal to (8.3.15) when $t_{ml} \ll \tau_c$.

8.4 The Photoconductive Impulse Response of the Cr:GaAs Samples

The impulse observed on the oscilloscope screen is the result of the convolution of the line current and the oscilloscope impulse response. By performing this convolution analytically, we can fit the calculated impulse to the displayed one, and then determine the photoconductivity fall time, τ_c, and the minimum gap resistance, R_o.

The impulse response of the oscilloscope is a Gaussian (see Appendix B). It cannot be analytically convolved with the exact form for the line current as given by (8.3.13). However, the line current can be approximated by a step exponential decay

$$I_{\ell a}(t) = \begin{cases} 0 & t < 0 \\ (I_\ell)_{max}\, e^{(t_{ml}-t)/\tau_\ell} & \end{cases} \tag{8.4.1}$$

where $(I_\ell)_{max}$ and t_{ml} are defined in (8.3.15) and (8.3.16), and τ_ℓ is defined by

$$I_\ell(t = t_{ml} + \tau_\ell) = e^{-1}(I_\ell)_{max} \tag{8.4.2}$$

This approximation is excellent for $t \geq t_{ml}$ for the typical values of R_o in our experiment ($\sim 3000\Omega$). At $t = 0$ the exponential approximation is somewhat larger than $(I_\ell)_{max}$ (by about 12%). This will be compensated

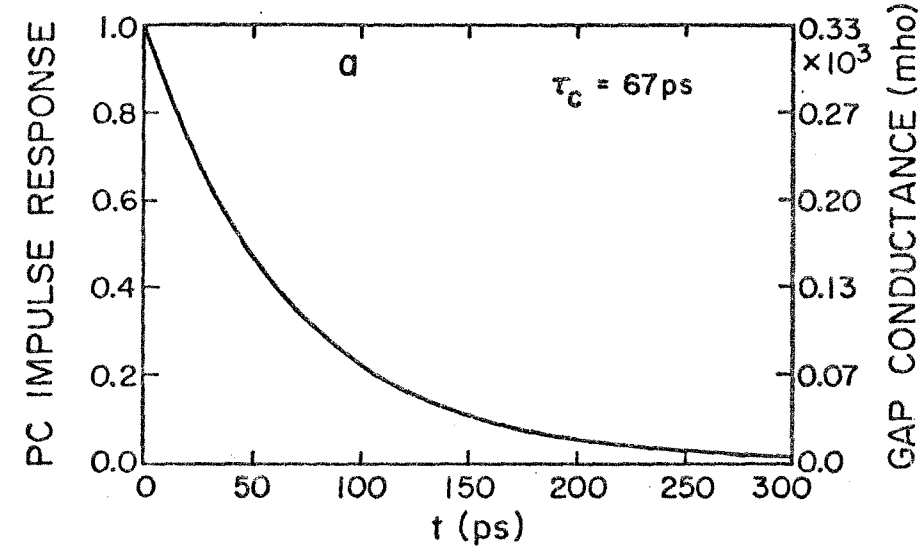
a
τ_c = 67ps
PC IMPULSE RESPONSE
GAP CONDUCTANCE (mho)
×10³
t (ps)

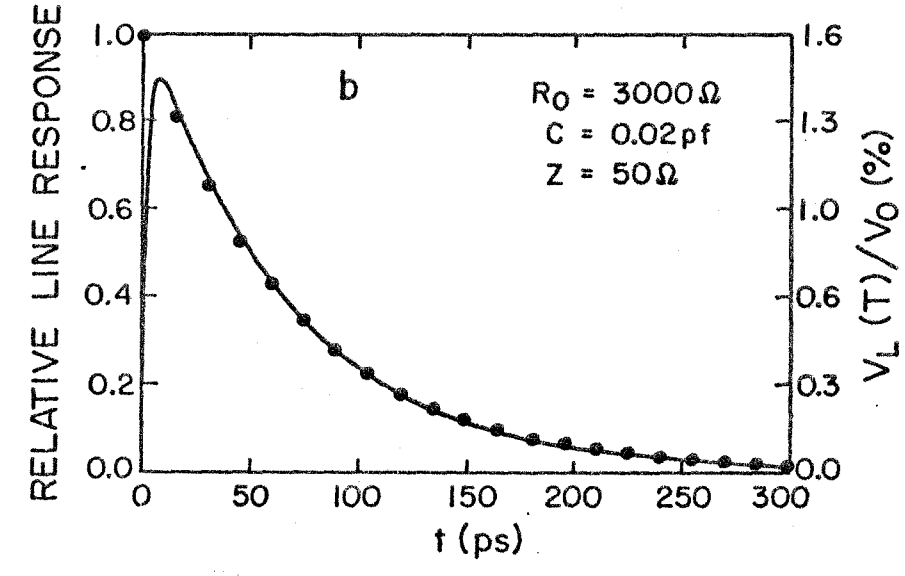
b
R_O = 3000Ω
C = 0.02pf
Z = 50Ω
RELATIVE LINE RESPONSE
$V_L(T)/V_O$ (%)
t (ps)

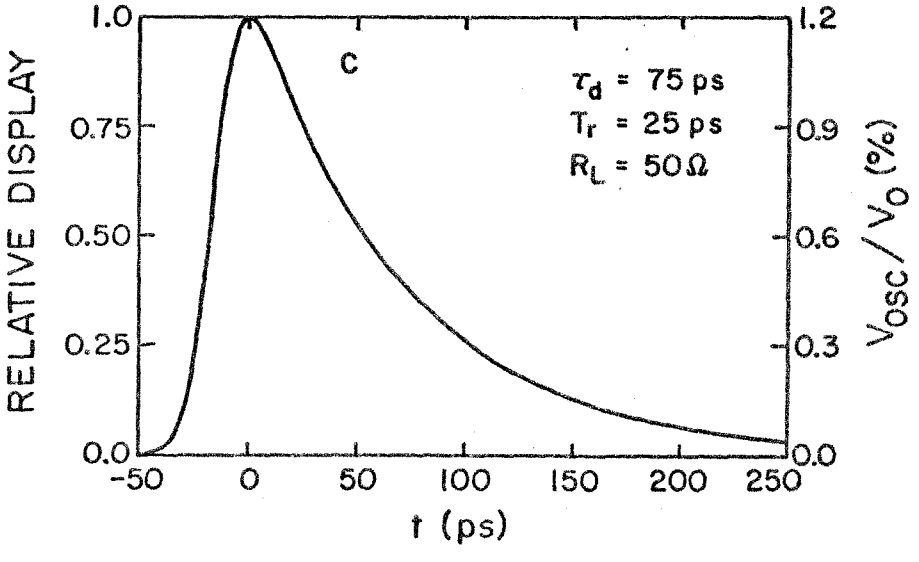
c
τ_d = 75 ps
T_r = 25 ps
R_L = 50Ω
RELATIVE DISPLAY
V_{OSC}/V_O (%)
t (ps)

Fig. 8.4.1 Fitting the Cr:GaAs photoconductive impulse response to the experimental observations. An exponential decay photoconductivity (8.3.10) with decay time of 67 psec is shown in (a). The resulting photocurrent pulse (8.3.13) is depicted in (b). The dotted line is the exponential approximation (8.4.1) with τ_ℓ = 70 psec. The curve in (c) is the calculated oscilloscope response (8.4.3). The left-hand vertical scales are normalized, while the right-hand scales depend on sample illumination level. V_o is the applied dc voltage, V_L is the line voltage, and V_{OSC} is the oscilloscope displayed voltage.

for by the oscilloscope filter response. The convolution of the step exponential decay of the line current (8.4.1) with the Gaussian impulse response results in

$$Y(t) = \frac{1}{2}(I_\ell)_{max}\, e^{t_{ml}/\tau_\ell} \exp\left(\frac{\sigma^2}{2\tau_\ell^2} - \frac{t}{\tau_\ell}\right)\left[1 + \mathrm{erf}\left(\frac{1}{\sqrt{2}}\left(\frac{t}{\sigma} - \frac{\sigma}{\tau_\ell}\right)\right)\right] \qquad (8.4.3)$$

where σ is the standard deviation of the Gaussian, and is related to the oscilloscope rise time, T_r, by (see Appendix B)

$$\sigma = 0.39\ T_r \qquad (8.4.4)$$

We will refer to (8.4.3) as the calculated oscilloscope display.

By fitting (8.4.3) to the observed impulse shown in Figure 7.4.1a the photoconductive impulse response of Cr:GaAs can be found. The computation was performed numerically. The parameters used in the calculations are:

τ_d (1/e decay time of the observed impulse) = 75 psec

C (gap capacitance) = 0.02 pf

R_Z (= $2Z_o$) = 100Ω

R_L (load resistance) = 50Ω

T_r (oscilloscope rise time) = 25 psec

T_o (observed transmission) = 1.2%

where the transmission is defined as the ratio between the amplitude of the observed switched voltage and the applied dc voltage, V_o.

The best fitted photoconductive impulse response of our Cr:GaAs samples, assumed to follow a step exponential decay as in equation (8.3.10), is shown in Figure 8.4.1a. The 1/e fall time is 67 psec. The photocurrent pulse which is generated as a result of such a variation in the gap conductivity is described analytically by equation (8.3.13), and graphically by the solid line in Figure 8.4.1b. The dotted line in this figure is the exponential approximation (8.4.1) of the actual current impulse (8.3.13). Its 1/e fall time is τ_ℓ = 70 psec. Finally, the calculated oscilloscope display (8.4.3) is shown in Figure 8.4.1c. This curve fits well the observed impulse response of Figure 7.4.1a. Note that while the left-hand vertical scales in Figure 8.4.1 are normalized, the right-hand scales, which are typical to our experiment, depend on the sample illumination level.

8.5 Estimation of the Gap Resistance from Bulk Conductivity

The conductivity of the gap can be estimated from the well known formula

$$\sigma = e\mu_n(n + p/b) \tag{8.5.1}$$

where

σ is the bulk conductivity

μ_n = the electrons' mobility

$b = \mu_n/\mu_p$, where μ_p is the holes' mobility

n,p = the respective electron and hole density

Generally, the conduction in Cr:GaAs is mixed [32] and $p \neq n$, but immediately after the picosecond pulse we may assume that

$$\bar{n} = n_o = p_o \tag{8.5.2}$$

so that

$$= e\mu_n(1 + \frac{1}{b})\bar{n} \tag{8.5.3}$$

The initial carrier density can be estimated by

$$\bar{n} = \frac{\varepsilon}{h\nu\ w\ell(\frac{1}{\alpha})}\eta \tag{8.5.4}$$

where

ε = energy contained in an optical pulse

$h\nu$ = photon energy

w = smaller between the strip width and the diameter of light spot

ℓ = gap length ($\leq w$)

$\frac{1}{\alpha}$ = absorption length

η = fraction of pulse photons which generates carriers (accounting for reflection and other losses)

When (8.5.4) is substituted in (8.5.1), the conductivity becomes

$$\sigma = \frac{e\mu_n(1 + \frac{1}{b})\varepsilon\eta}{h\nu\ w\ell(\frac{1}{\alpha})} \tag{8.5.5}$$

The resistance of the high conductive layer, the thickness of which is $1/\alpha$, is given by

$$R = \frac{1}{\sigma}\frac{\ell}{w(\frac{1}{\alpha})} \tag{8.5.6}$$

or

$$R = \frac{h\nu}{\eta\varepsilon}\frac{\ell^2}{e\mu_n(1 + \frac{1}{b})} \tag{8.5.7}$$

Typical values to use in (8.5.7) are $\eta\frac{\varepsilon}{h\nu} = 10^8$ photons/pulse,

μ_n = 3000 cm^2/V-sec, b = 18 (see Section 9.4), and ℓ = 0.01 cm. The gap minimum resistance is then estimated to be

$$R \simeq 2000\Omega \tag{8.5.8}$$

which is in good agreement with the experiment (see Section 8.4).

8.6 Conclusion

We have seen that the observed impulse response is not significantly affected by reflections at impedance discontinuities which might appear at the connections between various components of the circuit, or by dispersion in the microstrip. Based on the oscilloscope display, we assumed a simple model of exponential decay for the photoconductive impulse response of Cr:GaAs. It overlooks the complexity that might be involved in the decay of excess carriers in this material, a subject discussed in Chapter 9. However, it fits the experimental results well, when the response of the transmission line and of the oscilloscope are taken into account.

The fall time of the photoconductivity is found to be 67 ± 10 psec. This value will be used in the following analysis of transient photoconductivity in Cr:GaAs.

Appendix A

The differential equation (8.3.12) is solved here [31]. The equation is

$$\frac{di_2}{dt} + i_2\left[\frac{1}{\tau} + \frac{1}{R_z C} + \frac{e^{-t/\tau}}{R_o C}\right] = \frac{V_o}{C R_z R_o} e^{-t/\tau} \tag{A.1}$$

Define

$$d = \frac{V_o}{C R_z R_o} \qquad f = \frac{i_2}{\tau_d}$$

$$a = \frac{\tau}{R_z C} + 1 = g + 1 \qquad b = \frac{\tau}{R_o C} \tag{A.2}$$

and $s = t/\tau$. Then (A.1) becomes

$$\frac{df}{ds} + f[a + be^{-s}] = e^{-s} \tag{A.3}$$

The complementary function (the solution of the homogeneous equation) is

$$f_h = D \exp(-as + be^{-s}) \tag{A.4}$$

where D = const, and the particular solution is

$$f_p = e^{-as+be^{-s}} \int_{s_o}^{s} ds' \, e^{as'-be^{-s'}} e^{-s'} \tag{A.5}$$

Substituting

$$X_1 = be^{-s'} \tag{A.6}$$

in the integral gives

$$f_p = e^{-as+be^{-s}}\ b^{a-1} \int_{x}^{x_o} e^{-x_1}\ x_1^{-a}\ dx_1 \qquad (A.7)$$

Using the definition of the incomplete gamma function [33a],

$$\Gamma(z,x) \equiv \int_{x}^{\infty} e^{-x_1}\ x_1^{z-1}\ dx_1 \qquad (A.8)$$

the particular solution becomes

$$f_p = e^{-as+be^{-s}}\ b^{a-1}\ \Gamma(1-a,be^{-s}) + \text{const} \qquad (A.9)$$

To determine the constants in (A.4) and (A.7), we use the initial condition

$$f(s=0) = \frac{V_o}{R_o \tau_d} = \frac{1}{a-1} \qquad (A.10)$$

The general solution is then found to be

$$f(s) = f_h(s) + f_p(s)$$

$$= \{\frac{e^{-b}}{a-1} + b^{a-1}[\Gamma(1-a,be^{-s}) - \Gamma(1-a,b)]\}\ \exp(-as+be^{-s}) \qquad (A.11)$$

Using the normalization of (A.2) in equation (8.3.6) of the text,

$$\frac{I}{\tau_d} = b^{-1}[1 - (a-1)\ e^{s}\ f(s)] \qquad (A.12)$$

which leads to the following expression for the total current:

$$I(s) = \frac{V_o}{R_z} \{1 - (e^{-b} + gb^{g}[\Gamma(-g,be^{-s}) - \Gamma(-g,b)])e^{-gs+\ be^{-s}}\} \qquad (A.13)$$

Substituting the normalization of (A.2) in (A.13) gives equation (8.3.13) of the text.

To find the maximum of the total current we differentiate (A.13) with respect to s, and equate it to zero. This leads to

$$(e^{-b} + gb^{g}[\Gamma(-g,be^{-s_m}) - \Gamma(-g,b)])e^{-gs_m+be^{-s_m}} = \frac{g}{g + be^{-s_m}} \qquad (A.14)$$

where we used

$$\frac{\partial\Gamma(z,x)}{\partial x} = -x^{z-1}\, e^{-x} \qquad (A.15)$$

and s_m is defined by

$$I(s_m) = I_{max} \qquad (A.16)$$

When (A.14) is substituted in (A.13), and using the definition of g and b as in (A.2), the maximum total current is found to be

$$I_{max} = \frac{V_o}{R_o e^{s_m} + R_z} \qquad (A.17)$$

Appendix B

The response of an oscilloscope to an input signal can be described in terms of response of a filter. The response to a δ-function signal is called the "impulse response," and will be denoted here by $f_\delta(t)$. The response to a step function is called the "step response," and will be denoted $f_s(t)$.

The response of the filter to a general signal $x(t)$ is given by its convolution with the impulse response [61]

$$Y(t) = \int_{-\infty}^{\infty} f_\delta(t-t')\, x(t')\, dt' \tag{B.1}$$

It is common to approximate the response of the sampling oscilloscope by a Gaussian filter [34], i.e.,

$$f_\delta(t) = \frac{1}{\sigma\sqrt{2\pi}}\, e^{-t^2/2\sigma^2} \tag{B.2}$$

To test this approximation, we compare the step response of this filter to the oscilloscope display of an approximated step function current with rise time shorter than 25 ps, generated by the Tektronix S-52 pulse generator. The step response is easily found to be

$$Y_s(t) = \frac{1}{2}\left[\mathrm{erf}\left(\frac{t}{\sqrt{2}\sigma}\right) + 1\right] \tag{B.3}$$

and it is plotted in Figure B.1. The response of the oscilloscope is shown in Figure B.2.

The step response rise time is defined by

$$T_r = t_{0.9} - t_{0.1} \tag{B.4}$$

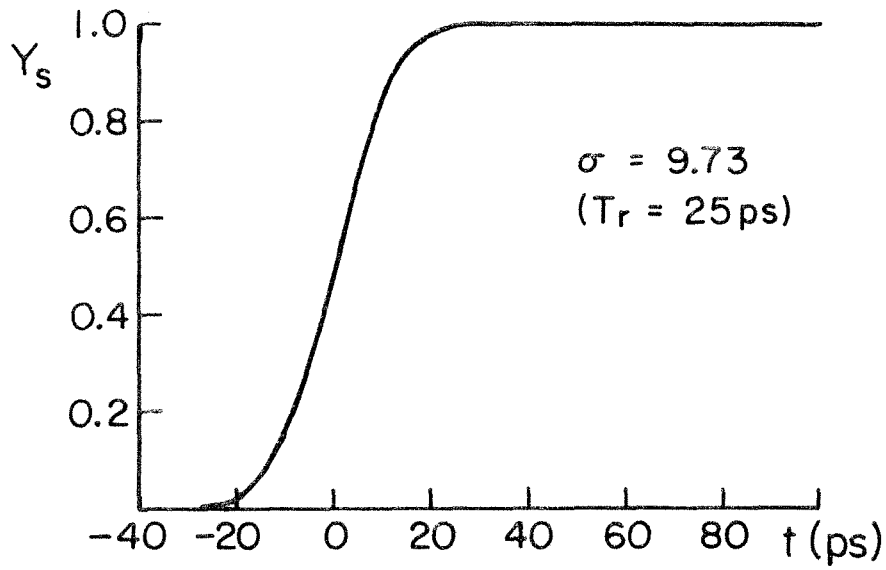

Fig. B.1 Step response of a Gaussian filter.

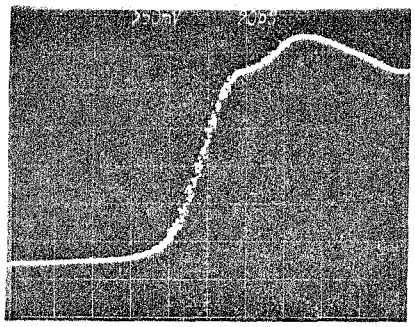

Fig. B.2 The response of the oscilloscope (Tektronix 7904/7S11-7T11 with S-4 sampling head) to an approximate step function current (generated by Tektronix S-52 pulse generator).

which gives

$$T_r = 2.57\sigma \tag{B.5}$$

Assume now a signal

$$x(t) = \begin{cases} 0 & t < 0 \\ e^{-t/\tau} & t \geq 0 \end{cases} \tag{B.6}$$

When (B.6) is substituted in (B.1), the response of the oscilloscope is found to be

$$Y(t) = \frac{1}{2} \exp\left(\frac{\sigma^2}{2\tau^2} - \frac{t}{\tau}\right)\left[1 + \operatorname{erf}\left(\frac{1}{\sqrt{2}}\left(\frac{t}{\sigma} - \frac{\sigma}{\tau}\right)\right)\right] \tag{B.7}$$

Notice that since we chose the Gaussian maximum to be at t = 0, the response Y(t) is nonzero for t < 0 in spite of (B.6). There is no contradiction since we ignore the delay in the oscilloscope lines. The response amplitude is not unity, as is the amplitude of the signal. It is given by

$$Y_{max} = \frac{\tau}{\sqrt{2\pi}\sigma} \exp\left(-\frac{t_{m2}^2}{2\sigma^2}\right) \tag{B.8}$$

where

$$t_{m2} = \left(\sqrt{2}\, z_m + \frac{\sigma}{\tau}\right)\sigma \tag{B.9}$$

and z_m is the root of the equation.

$$1 + \operatorname{erf}(z) - \sqrt{\frac{2}{\pi}}\, \frac{\tau}{\sigma}\, e^{-z^2} = 0 \tag{B.10}$$

Equation (B.10) can be rewritten as

$$e^{z^2} \operatorname{erfc}(z) = -\sqrt{\frac{2}{\pi}}\, \frac{\tau}{\sigma} + 2e^{z^2} \tag{B.11}$$

This form of the equation is very helpful in estimating z_m, and therefore Y_{max}. Not only is the left side plotted in the literature [33b], but it can also be estimated from the inequality [33c]

$$\frac{2}{\sqrt{\pi}} \frac{1}{z + \sqrt{z^2 + 2}} \leq e^{z^2} \operatorname{erfc}(z) \leq \frac{2}{\sqrt{\pi}} \frac{1}{z + \sqrt{z^2 + \frac{4}{\pi}}} \tag{B.12}$$

or, from (B.11):

$$A(z) + K \equiv \frac{1}{\sqrt{\pi}} \frac{1}{z + \sqrt{z^2 + 2}} + K \leq e^{z^2} \leq K + \frac{1}{\sqrt{\pi}} \frac{1}{z + \sqrt{z^2 + \frac{4}{\pi}}} \quad K + B(z) \tag{B.13}$$

where $A(z)$ and $B(z)$ are defined, and

$$K = \frac{\tau}{\sqrt{2\pi}\,\sigma} \tag{B.14}$$

Estimation of z_m can now be done by calculating (B.13) iteratively, i.e.,

$$\exp(z_{i+1}) = K + \frac{1}{2}\left[A(z_i) + B(z_i)\right] \tag{B.15}$$

starting with $z_1 = \infty$.

Example: $\tau = 70$ ps (see Figure 8.4.1), $\sigma = 9.73$ ps (i.e., $T_r = 25$ ps), then in the first step

$$e^{z_1^2} = K = 2.87 \tag{B.16}$$

so that

$$z_1 = 1.03 \tag{B.17}$$

The second step is

$$e^{z_2^2} = K + 0.21 \tag{B.18}$$

so that

$$z_2 = 1.06 \tag{B.19}$$

and from (B.9) and (B.8) we find

$$Y_{max} = 0.75 \tag{B.20}$$

Note: A Gaussian function has been used to describe the oscilloscope impulse response, in spite of the slight discrepancy between the calculated (Figure B.1) and observed (Figure B.2) oscilloscope step response. It is impossible to deduce the exact oscilloscope step response from Figure B.2. There is no other mean to test the Tektronix S-52 pulse generator, but the sampling oscilloscope we use, so that it is not known whether the bump in Figure B.2 is in the generated pulse or is due to the oscilloscope response. In any event, if it had affected the experimental results at all, it would not have been by more than several percent, as seen by comparing the temporal and amplitude behavior of Figure B.1 to those of Figure 7.4.1. This error is insignificant in view of the total experimental error (± 15%) and the interpretation of the experimental results discussed in Chapter 9.

Chapter 9

PHOTOCARRIER LIFETIME IN Cr:GaAs

9.0 Introduction

In the previous chapters, experimental results of Cr:GaAs photoconductive response to picosecond pulse illumination were presented and analyzed. It was concluded that following the photoexcitation, the conductivity decayed nearly exponentially with 1/e fall time of $\sim$ 67 psec. This indicates photocarrier lifetime much shorter than that of undoped GaAs ($\gtrsim$ 1 ns) and of Cr:GaAs when measured under different experimental conditions (250 psec [53] to 0.1 μsec [59]). In this chapter photocarrier lifetime in Cr:GaAs will be theoretically investigated, based on physical and chemical properties of the material. These properties will be summarized from the abundance of literature published on this matter. Bulk recombination through deep flaws will be discussed. It will be shown to be an effective lifetime reduction mechanism in Cr:GaAs, although, in contrast to propositions by previous investigators [4], not solely responsible for our observed ultrafast photoconductive decay time. A model which considers the combined effect of bulk and surface recombination will be shown to be capable of interpreting our experimental results.

9.1 Material Growth

In general, Cr:GaAs samples were purchased from Crystal Specialties, Inc. [10b]. One sample from another source [11] was also studied, but as the results were similar to the other samples, it was not

further investigated. The information in this section is thus related directly to the material purchased from Crystal Specialties, Inc.

The crystals were grown by the horizontal Bridgeman technique. High resistivity was achieved by compensation; chromium, as a deep acceptor, was added to the melt to compensate residual shallow donors. The major source of these donors was Si contamination from the quartz boat and growth ampule. At high temperatures (1250°C) quartz breaks down according to

$$2SiO_2 \rightarrow 2SiO + O_2 \qquad (9.1.1)$$

As SiO is volatile, it eventually finds itself in the GaAs melt, thus producing Si contamination. The O_2 reacts with the Ga to form Ga_2O_3, which is also volatile and transports to the cool part of the growth ampule. By raising the temperature above 1000°C, the Ga_2O_3 dissociates, supplying O_2 to reverse the reaction

$$2SiO_2 \rightleftarrows 2SiO + O_2 \qquad (9.1.2)$$

and, as a result, the Si presence is reduced. The Si concentration obtained was about 10^{15} cm^{-3}. Although this was also the concentration of chromium needed for compensation, concentrations of about 10^{16}-10^{17} cm^{-3} were used. At this doping level the resistivity is 10^8-10^9 Ω-cm.

9.2 Impurity Concentration in Cr:GaAs and its Energy Levels

The impurities and their concentrations in Cr:GaAs crystals depend strongly on growing conditions. Not only do they vary from growth to growth, but they are also distributed non-uniformly within the volume of

the ingot [35]. It is, therefore, not surprising that impurity concentrations reported by different investigators for "similar" growth conditions are not the same but fall within a wide range. The spread of this range can be seen in Figure 9.2.1, where published data of impurity concentrations measured by mass spectroscopy are compiled in a histogram. This non-uniformity of impurities and their concentrations is consistent with the wide range of results of electronic and photoelectronic measurements performed on Cr:GaAs ([36]-[38], and many others).

The solubility of Cr in GaAs is relatively low, 10^{18} atoms/cm^3 (higher concentrations precipitate [39]); it is impossible to increase its concentration much above that shown in Figure 9.2.1. The Cr atoms are found at the Ga sites [39]. In n-type there are Cr^{2+} ions with electronic configuration $3d^4$. The crystal field splits its ^5D term into two levels, an upper ^5E and a lower $^5T_2$. The lower one lies in the energy gap. In p type, in addition, there are neutral Cr^{3+} acceptors with electronic configuration $3d^3$. A tetragonal crystal field splits the ^4F term of the free ion into three levels: $^4T_1$, $^4T_2$, and $^4A_2$. The lowest, i.e., the $^4T_1$ level, is in the energy gap [46,50].

The impurity energy levels have been a subject of several investigations. They have been generally deduced from spectra of absorption, photoluminiscence, and photoconductivity. The exact identification of some of the levels and their location are still disputed. The important common feature is the deep levels associated with chromium and oxygen.*

---

*The identification of one of the deep impurity levels as oxygen is common, but as yet not entirely conclusive [42].

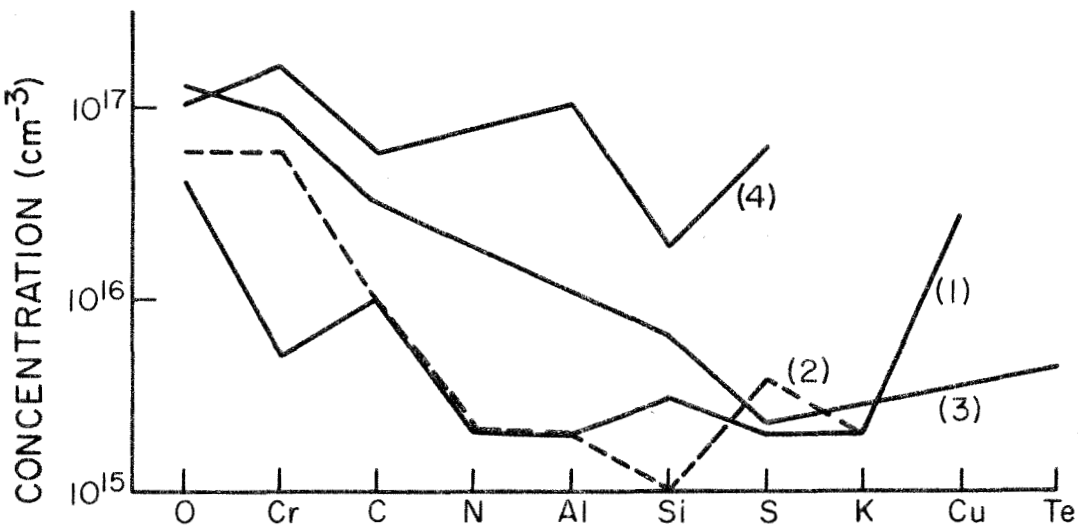

Fig. 9.2.1 A histogram of impurity concentrations, measured by mass spectroscopy. Curves (1) and (2) are from Ref. [37] for low and high Cr concentration samples, respectively. Curve (3) is from [38], and (4) is from [36].

The closeness of the concentration and energy levels of oxygen and Cr impurities must be taken into account in any analysis before identifying any phenomenon with only one of the two impurities. This is true in steady state photoelectronic measurements [36], as well as in transient photoconductivity, which is the subject of the present investigation.

Two of the energy level diagrams which have been suggested are shown in Figure 9.2.2. Look [40] suggested the diagram of Figure 9.2.2a for the deep levels in Cr:GaAs. Other impurities are considered to be shallow, although Cu is associated with relatively deep levels at 0.24 eV and 0.51 eV above the valence band, as well as two other shallower levels [41]. Lindquist [38] suggested the diagram in Figure 9.2.2b. He suggested these four levels as a model to explain some bulk electrical properties.

9.3 The Fermi Level and the Predicted Resistivity of Cr:GaAs

Knowledge of the exact location of the Fermi level is required if electronic properties are to be calculated from an energy diagram. Cr:GaAs is a compensated semiconductor, consequently, the Fermi level is expected to be in the vicinity of the center of the energy gap. At room temperature, the gap energy is $E_g = 1.43$ eV and $kT = 0.026$ eV, so that

$$\frac{E_c - E_f}{kT} \simeq \frac{E_f - E_v}{kT} \simeq \frac{\frac{1}{2}E_g}{kT} = 27.5 \gg 1 \qquad (9.3.1)$$

It is, therefore, possible to express the total electron density in the conduction band and the total hole density in the valence band at

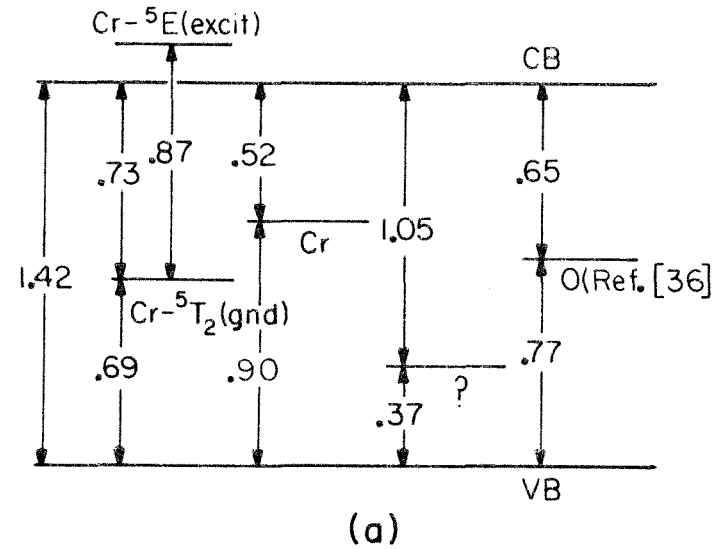

(a)

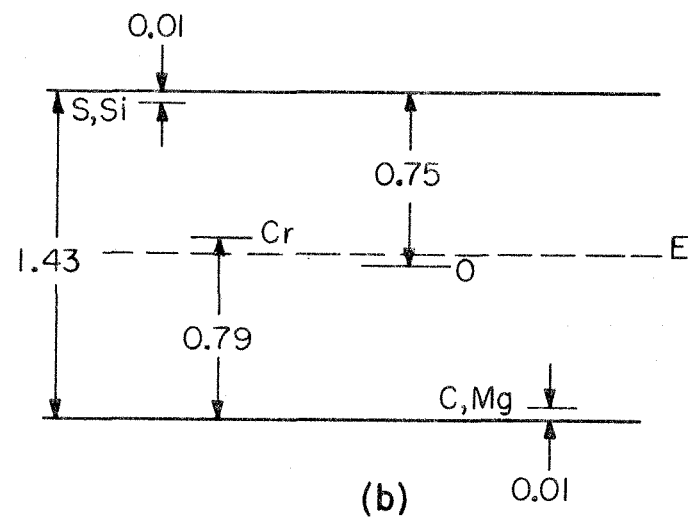

(b)

Fig. 9.2.2 Deep impurity energy level diagrams of Cr:GaAs at room temperature: (a) Ref.[40], (b) Ref.[38]. The energy units are eV.

thermal equilibrium by [43a]

$$n_o = N_c \, e^{-(E_c - E_f)/kT} \tag{9.3.2}$$

$$p_o = N_v \, e^{-(E_f - E_v)/kT} \tag{9.3.3}$$

where E_c, E_v, and E_f are the energies of the bottom of the conduction band, the top of the valence band, and the Fermi level, respectively. N_c and N_v are the effective densities of states at the proper bands, given by

$$N_c = 2\left(\frac{2\pi m_e kT}{h^2}\right)^{3/2} \tag{9.3.4}$$

$$N_v = 2\left(\frac{2\pi m_h kT}{h^2}\right)^{3/2} \tag{9.3.5}$$

in which m_e and m_h are the effective masses of electrons and holes, respectively. Using $m_e = 0.07\ m_o$ and $m_h = 0.5\ m_o$ [39], where m_o is the free electron mass, we find at room temperature

$$N_c = 4.64 \times 10^{17}\ \text{cm}^{-3} \tag{9.3.6}$$

$$N_v = 8.86 \times 10^{18}\ \text{cm}^{-3} \tag{9.3.7}$$

To find the Fermi level, one solves, in principle, the charge neutrality equation

$$n_o + \sum_j N_{ja}^- = p_o + \sum_j N_{jd}^+ \tag{9.3.8}$$

where N_{ja}^- and N_{jd}^+ are the ionized acceptors and donors, respectively, present in the material. A consideration of all the ionized impurities

would make a solution intractable. Zucca [37] suggested considering only one deep donor and one deep acceptor to interpret experimental data of electronic measurements. This assumption simplifies the solution of (9.3.8), and will be used here to calculate the energy of the Fermi level. A further simplification of (9.3.8) is obtained when n_o and p_o are neglected. To justify this step, we get an estimate of n_o and p_o by assuming that the Fermi level lies at the center of the gap, then from (9.3.2) and (9.3.3), at T = 300°K

$$n_o \sim 5.3 \times 10^5 \text{ cm}^{-3} \tag{9.3.9}$$

$$p_o \sim 1 \times 10^7 \text{ cm}^{-3} \tag{9.3.10}$$

The concentrations of the impurities were given in the previous section. They are of the order of magnitude of 10^{16} cm^{-3}. Most of them are ionized, and therefore

$$N_a^-, N_d^+ >> n_o, p_o \tag{9.3.11}$$

and (9.3.8) becomes

$$N_a^- = N_d^+ \tag{9.3.12}$$

It can be rewritten explicitly as

$$\frac{N_a}{1 + g_a \exp[(E_a - E_f)/kT]} = \frac{N_d}{1 + g_d \exp[(E_f - E_d)/kT]} \tag{9.3.13}$$

where g_a and g_d are the degeneracies, and E_a and E_d are the energies of the acceptor and the donor levels, respectively. Solving (9.3.13) gives [27]

$$E_f = \frac{E_a + E_d}{2} - kT \ln G \tag{9.3.14}$$

where

$$G = \frac{1}{2g_a}\left\{-\left(1-\frac{N_a}{N_d}\right) e^{(E_d-E_a)/2kT} + \left[\left(1-\frac{N_a}{N_d}\right)^2 e^{(E_d-E_a)/kT} + 4\left(\frac{N_a}{N_d}\right) g_d g_a\right]^{1/2}\right\} \qquad (9.3.15)$$

We may use this model and the energy level diagrams to obtain an order of magnitude estimate of the Fermi level, n_o, p_o, and ρ. Using, for instance, the diagram of Figure 9.2.2b and $N_a/N_d = 0.59$ [38], we find $E_f = 0.74$ eV, $n_o = 1.5 \times 10^6$ cm^{-3}, $p_o = 3.5 \times 10^6$ cm^{-3}. When we take $\mu_n = 3000$ cm^2/V sec and $b = \mu_n/\mu_p = 18$ (see Section 9.4), the resistivity is calculated from $\rho_o^{-1} = e\mu_n (n_o + p_o/b)$ to be $1.2 \times 10^9 \Omega$-cm. In this example, the conduction is mixed, although due to the large mobility ratio, the material is an n-type. The Fermi level is close to mid-gap, consistent with the assumption which led to (9.3.9) and (9.3.10).

9.4 Electron and Hole Mobilities in Cr:GaAs

A correct value of the carrier mobility is required if excess carrier lifetime is to be calculated from photoconductivity measurements. The conductivity mobility is defined by $\mu = \sigma/ne$, where σ is the conductivity, n is the majority carrier density, and e is the electron charge. It can be calculated from Hall effect measurements; however, it should not be confused with the Hall mobility which is a parameter with the same dimensions. The ratio between the conductivity and the Hall mobilities, which depends on the mechanism of scattering and on the degree of degeneracy, varies between one-half and unity [44a].

The conductivity of Cr:GaAs is mixed [32], and therefore Hall effect measurements are not sufficient to solve for μ_n and μ_p. Magnetoresistance measurement supplies the complementary information. This effect is based on the lowering of the conductivity along the sample axis due to the deflection of the charge carriers by the magnetic field. Following these considerations, Philadelpheus and Euthymiou [45] measured the Hall and the magnetoresistance effect in one n-type and six p-type samples and calculated their carrier mobility. The calculated values were close to each other and their average was

$$\mu_n = 3030 \pm 342 \text{ cm}^2/\text{V sec} \tag{9.4.1}$$

and

$$b \equiv \mu_n/\mu_p = 18.3 \pm 2.3 \tag{9.4.2}$$

The electron mobility is thus lower than in low resistivity GaAs where $\mu_n = 8600 \text{ cm}^2/\text{V sec}$ and $b = 21$ [46]. A similar phenomenon is found in high resistivity gold doped silicon [47]. The low mobility is related to the weakening of the screening of the ionized impurities which are the most important scattering centers for electrons.

Based on (9.4.1) and (9.4.2), the electron mobility and the mobility ratio used in the following sections will be:

$$\mu_n = 3000 \text{ cm}^2/\text{V sec} \tag{9.4.3}$$

$$b = 18 \tag{9.4.4}$$

Having introduced chromium doped GaAs and its properties, we now turn to deal with the main subject of this chapter, the return of carrier density to equilibrium following an excitation by picosecond optical pulses.

9.5 Carrier Density Return to Equilibrium

In an unperturbed semiconductor, the carrier concentrations are in a state of equilibrium. If disturbed, they will attempt to return to this state through generation of new carriers or by recombination of the excess ones.

When a semiconductor is illuminated by radiation with photon energy higher than the energy gap, the main generation process is that of electron-hole excitation. The contribution to the conductivity by other processes which might take place, such as excitation from impurities, or Auger generation, is smaller.

The recombination process is far more complex. There are several paths of recombination, and an electron-hole pair has some probability to proceed along any one of them. The simplest path is the band to band recombination: An electron from the conduction band fills a hole in the valence band. In a direct transition, both electron and hole have the same momentum. In an indirect transition they do not, and a phonon is absorbed or emitted to make up for the momentum difference. If a photon is emitted in this process, it is called a "radiative transition." Radiative transitions in GaAs are more probable than nonradiative transitions. In a nonradiative transition the energy of the electron-hole pair can be dissipated as phonons or can be given to a third carrier. The later process is the Auger (or impact) recombination. Another recombination

path involves energy levels which lie in the energy gap. These levels have finite cross section for the capture of electrons and holes, and for their consequent release. When, for example, an electron from the conduction band is captured by such a level, the next step can be one of two: The electron is released thermally and returns to the conduction band, or a hole is captured by the same center, thus annihilating the electron-hole pair. If the probability for the first process is higher, the level is called a trap. Otherwise it is called a recombination center. A specific level can be a trap under some conditions and a recombination center under others. A similar process can be described for holes.

Traps and recombination centers play very important roles in the process of returning to equilibrium. They have opposite effects on the decay time of excess carriers. A carrier captured by a trap is not statistically available for recombination. Such a carrier can be released to its appropriate band long after the uncaptured carriers have recombined. Therefore, the conductivity decay time can be longer than the free electron lifetime. On the other hand, the recombination centers relieve the wave vector selection rules, thus increasing the probability of an electron-hole pair to recombine. As a result, the conductivity decay time can be reduced. In the presence of traps and recombination centers, the electron lifetime can differ from that of the hole. Also, it is possible that the transient decay time will not be equal to the steady state lifetime.

In light of the observed ultrashort photocarrier decay time in Cr:GaAs ($\sim$ 67 ps, see Chapter 8), it seems that the band-to-band and

the Auger recombination processes are not the dominant ones (in GaAs, they are known to give rise to carrier lifetimes longer than 1 ns). On the other hand, the presence of deep levels in Cr:GaAs might reduce the carrier lifetime. Therefore, the process of recombination through recombination centers is the subject of the following sections, where it is analyzed and compared with the experiment.

9.6 Electron-Hole Recombination through Recombination Centers

Since the recombination centers assist in annihilating electron-hole pairs by capturing free carriers from their appropriate bands, it is expected that they would be most effective when they lie close to the middle of the gap. The carrier lifetimes are then shorter. In Section 9.2 we saw that there were several deep levels in Cr:GaAs. They can act as recombination centers, and therefore might be responsible for the short photoconductivity decay time. An exact analysis of this recombination process under conditions of our experiment is impractical [43]. These conditions include the multiple deep levels in the Cr:GaAs, the trap and excess carrier concentrations which are higher than the carrier density at thermal equilibrium, and the pulsed illumination. However, some insight can be gained by resorting to the theory of recombination through the mechanism of trapping, as developed by Shockley and Read [47] and Hall [48] under much simplified conditions. The general lines of the following discussion are based, in part, on Blakemore [43]. Let us assume a single monovalent flaw level at energy E_t. Such a level has two states only, empty or full (with respect to an electron), and is charged accordingly. The density of states of the

level will be denoted by N_t. Denote by $F(E_t)$ the fraction of the filled states. In thermal equilibrium

$$F(E_t) = f(E_t) = \frac{1}{1 + \exp(\frac{E_t - E_f}{kT})} \tag{9.6.1}$$

which is the Fermi-Dirac probability. For convenience we define

$$n_1 = N_c e^{(E_t - E_c)/kT} = n_o e^{(E_t - E_f)/kT} = n_i e^{(E_t - E_i)/kT} \tag{9.6.2}$$

$$p_1 = N_v e^{(E_v - E_t)/kT} = p_o e^{(E_f - E_t)/kT} = n_i e^{(E_i - E_t)/kT} \tag{9.6.3}$$

where n_i is the electron density and E_i is the Fermi level in an intrinsic GaAs crystal, and n_1 and p_1 would be the free carriers at thermal equilibrium if the Fermi level coincided with the flaw level. In terms of n_o, n_1, p_o, and p_1, the Fermi-Dirac distribution can be written as

$$f(E_t) = \frac{n_o}{n_o + n_1} = \frac{p_1}{p_o + p_1} \tag{9.6.4}$$

When a deviation from thermal equilibrium occurs, with excess electrons n_e and excess holes p_e, the fraction of the filled states becomes

$$F(E_t) = f(E_t) + \frac{p_e - n_e}{N_t} \tag{9.6.5}$$

as long as the semiconductor remains electrically neutral. The rate $(sec^{-1} \cdot cm^{-3})$ in which electrons from the conduction band are captured is given by

$$r_{nc} = n\langle C_n \rangle N_t (1 - F(E_t)) \tag{9.6.6}$$

where n is the conductive electron density. The brackets around the

constant C_n denote an average over all states in the conduction band [43d]. The dimension of $\langle C_n \rangle$ is cm^3/sec, and it is commonly written as σv_{th}, where σ is the capture cross section, and v_{th} is the thermal velocity ($\simeq \sqrt{3kT/m^*}$). Define now

$$\tau_{no} \equiv \frac{1}{\langle C_n \rangle N_t} \tag{9.6.7}$$

τ_{no} is the shortest possible time constant for electron capture. Substituting in (9.6.6) gives

$$r_{nc} = \frac{n}{\tau_{no}} (1 - F(E_t)) \tag{9.6.8}$$

Similarly, the hole trapping rate is

$$r_{pc} = \frac{p}{\tau_{po}} F(E_t) \tag{9.6.9}$$

Electrons are released from trapping flaws at a rate

$$r_{nr} = R_n N_t F(E_t) \tag{9.6.10}$$

and holes

$$r_{pr} = R_p N_i (1 - F(E_t)) \tag{9.6.11}$$

where R_n and R_p are the release probabilities per second for electrons and holes, respectively. R_n and R_p can be estimated at thermal equilibrium with no external generation, by equating $r_{nc} = r_{nr}$ and $r_{pc} = r_{pr}$. It is easily shown, with the aid of (9.6.2) and (9.6.3) that r_{nr} and r_{pr} become

$$r_{nr} = \frac{n_1 F(E_t)}{\tau_{no}} \tag{9.6.12}$$

$$r_{pr} = \frac{p_1(1 - F(E_t)}{\tau_{po}} \tag{9.6.13}$$

The net rate of electron capture is then

$$r_{nc}-r_{nr} = \frac{1}{\tau_{no}} [n(1 - F(E_t)) - n_1 F(E_t)] \tag{9.6.14}$$

and that of the holes is

$$r_{pc}-r_{pr} = \frac{1}{\tau_{po}} [pF(E_t) - p_1(1 - F(E_t))] \tag{9.6.15}$$

By using (9.6.5) and (9.6.4) in (9.6.14) and (9.6.15), the net rates of capture become

$$r_{nc}-r_{nr} = \frac{1}{\tau_{no}} [\frac{(n_o+n_1+n_e)(n_e-p_e)}{N_t} + \frac{n_e n_1}{n_1+n_o}] \tag{9.6.16}$$

and

$$r_{pc}-r_{pr} = \frac{1}{\tau_{po}} [\frac{(p_o+p_1+p_e)(p_e-n_e)}{N_t} + \frac{p_e p_1}{p_1+p_o}] \tag{9.6.17}$$

Before carrying the analysis further, we can gain insight into the process of recombination through a flaw by assuming steady state illumination. Under this condition the net rates of electron and hole captures are equal. By equating (9.6.14) to (9.6.15), the fraction of the filled flaws is found to be

$$F(E_t) = \frac{\tau_{po} n + \tau_{no} p}{\tau_{no}(p+p_1) + \tau_{po}(n+n_1)} \tag{9.6.18}$$

Substituting in (9.6.14) gives

$$U = r_{nc} - r_{nr} = \frac{pn - n_i^2}{\tau_{no}(p+p_1) + \tau_{po}(n+n_1)} \tag{9.6.19}$$

where U is the recombination rate through the mediation of the flaw. The dependence of U on E_t is through n_1 and p_1, as given by (9.6.2) and (9.6.3), i.e.,

$$U = \frac{pn - n_i^2}{\tau_{no}[p+n_i e^{(E_i-E_t/kT}] + \tau_{po}[n+n_i e^{(E_t-E_i)/kT}]} \tag{9.6.20}$$

For the special case of $\tau_{no} = \tau_{po}$

$$F(E_t) = \frac{n+p}{p+n+2n_i \cosh(\frac{E_t-E_i}{kT})} \tag{9.6.21}$$

$$U = \frac{1}{\tau_{no}} \frac{pn-n_i^2}{p+n+2n_i \cosh(\frac{E_t-E_i}{kT})} \tag{9.6.22}$$

The closer the flaw level to the intrinsic Fermi level, the higher the recombination rate. Recalling that

$$E_i \equiv \frac{1}{2} E_g + \frac{1}{2} kT \ln \frac{N_v}{N_c} \tag{9.6.23}$$

we can calculate the intrinsic Fermi level of GaAs at room temperature by using the values of N_v and N_c given in (9.3.6) and (9.3.7),

$$E_i = 0.75 \text{ eV} \tag{9.6.24}$$

above the valence band. We may thus conclude that, at least at the condition under which (9.6.22) has been derived, the deep levels are more

effective in the recombination process than the shallower ones.

These calculations suggest that the deep levels in the Cr:GaAs may be responsible for the observed short photocarrier lifetime. Note, though, that this is not yet conclusive because when trapping of the carriers occurs, the electron and hole lifetimes cannot be determined from the recombination rate alone.

Returning now to the net capture rates, (9.6.16) and (9.6.17), we proceed to discuss the transient decay of the excess carriers. If we assume that the recombination through the flaw levels is the only probable process in which electron-hole pairs are annihilated, then the carrier lifetimes are given by

$$\tau_n = \frac{n_e}{r_{nc} - r_{nr}} \quad , \qquad \tau_p = \frac{p_e}{r_{pc} - r_{pr}} \tag{9.6.25}$$

and if we ignore for the moment drift or diffusion current, the continuity equation becomes

$$\frac{dn_e}{dt} = g - \frac{n_e}{\tau_n} = g - \frac{1}{\tau_{no}} \left[\frac{(n_o+n_1+n_e)(n_e-p_e)}{N_t} + \frac{n_e n_1}{n_o+n_1} \right] \tag{9.6.26}$$

$$\frac{dp_e}{dt} = g - \frac{p_e}{\tau_p} = g - \frac{1}{\tau_{po}} \left[\frac{(p_o+p_1+p_e)(p_e-n_e)}{N_t} + \frac{p_e p_1}{p_o+p_1} \right] \tag{9.6.27}$$

Unfortunately, this is almost as far as one can proceed analytically for arbitrary N_t, n_e, and p_e. The equations can be linearized and solved only under very restrictive conditions, such as low excitation level ($n_e, p_e \ll n_o, p_o$), or small density of flaws. References for these solutions are given in [43c]. It is possible, though, to follow the decay

of photocarriers by dividing the decay process into stages. If the excess carriers are generated by a δ-function illumination, then initially $n_{eo} = p_{eo}$, and

$$\tau_n = \tau_{n1} = \tau_{no}(1 + \frac{n_o}{n_1}) \tag{9.6.28}$$

$$\tau_p = \tau_{p1} = \tau_{po}(1 + \frac{p_o}{p_1}) \tag{9.6.29}$$

where τ_{n1} and τ_{p1} are the decay times at this first stage. These decay times prevail as long as the first terms on the right hand side of (9.6.26) and (9.6.27) are much smaller than the second ones. This condition is trivially satisfied if $\tau_{n1} = \tau_{p1}$, so that $n_e = p_e$ through the all decay process. But if a trapping cross-section of one type of carrier is larger than that of the other, this may not be the case, and a difference between the densities starts to evolve so that $p_e - n_e \neq 0$. The new values of τ_n and τ_p depend then on the sign of $(p_e - n_e)$. For $p_e - n_e < 0$, $\tau_{p2} > \tau_{p1}$ and $\tau_{n2} < \tau_{n1}$, and vice versa (τ_{n2} and τ_{p2} are the decay times at the second stage of decay).

In our experiment, $n_{eo} = p_{eo} \sim 10^{16}\text{cm}^{-3}$, while $n_1 = n_o \sim 10^{6}\text{cm}^{-3}$. We can therefore write the condition for $\tau_n \simeq \tau_{n1}$ as [see (9.6.26)]

$$\left|\frac{n_e - p_e}{N_t}\right| << \frac{1}{n_o/n_1 + 1} \tag{9.6.30}$$

and for $\tau_p \simeq \tau_{p1}$ as

$$\left|\frac{n_e - p_e}{N_t}\right| << \frac{1}{p_o/p_1 + 1} \tag{9.6.31}$$

From the definition of n_1 and p_1 in (9.6.2) and (9.6.3),

$$\frac{n_o}{n_1} = \frac{p_1}{n_o} = e^{(E_f - E_t)/kT} \tag{9.6.32}$$

In Section 9.3, E_f was calculated for the energy level diagram of Figure 9.2.2b. Using this value and regarding the Cr level as the most important recombination center, we find at room temperature

$$\frac{n_o}{n_1} = \frac{p_1}{p_o} = 0.15 \tag{9.6.33}$$

and (9.6.30) and (9.6.31) become

$$\left|\frac{n_e - p_e}{N_t}\right| \ll 0.9 \tag{9.6.34}$$

and

$$\left|\frac{n_e - p_e}{N_t}\right| \ll 0.1 \tag{9.6.35}$$

Since $N_t \sim 10^{17}\text{cm}^{-1}$ (see Section 9.2) and $n_{eo} = n_{po} \sim 10^{16}\text{cm}^{-3}$, (9.6.34) seems to be satisfied not only at the early stages of the decay, but also at the later ones. Consequently, (9.6.28) can be taken as an estimate of τ_n,

$$\tau_n \simeq 1.15\ \tau_{no} \tag{9.6.36}$$

9.7 Multiple Recombination Centers and Traps

The previous section dealt with the case of a single recombination center. Continuity equations which describe the evolution of the excess carriers were presented, but no general solution has been found. Matters become much more complicated when several recombination centers as well as traps are present, as is the case of Cr:GaAs. The contribution of the deep levels is not only to recombination, but also to trapping. Their total effect can either be of shortening or lengthening the free carrier lifetime. If, for instance, one deep level initially traps holes, while the other initially traps electrons, clearly the probability of recombination, and thus its rate, decreases. Or, as another example, if one impurity has a much higher trapping cross section for one type of carrier, that carrier will not be available for recombination, and the carriers of the other type might enjoy a longer lifetime (doping of a material with such a center is sometimes called "Sensitization").

The problem of multiple recombination centers has been treated under simplified conditions, which do not apply to our case. For small modulation and steady state stimulation, Kalashnikov [49] concluded that the excess carrier lifetime can be expressed by

$$\frac{1}{\tau} = \sum_j \frac{1}{\tau_j} - \nu_{coup} \qquad (9.7.1)$$

where τ_j is the lifetime which would apply if only the j^{th} center existed, with Fermi level unchanged, and ν_{coup} represents the coupling between them.

Unlike recombination centers, traps can lengthen the decay time, unless the trapping time is longer than the recombination time. If the trapping time is shorter, then carriers will be trapped first. Since the trapping levels and the recombination centers lie at different locations in the crystal, trapped carriers must first be thermally released to the appropriate bands before reaching the recombination center. The new decay times can be estimated from steady state considerations to be [62]

$$\tau_{dn} = (1 + n_t/n)\tau_n \tag{9.7.2}$$

$$\tau_{dp} = (1 + p_t/p)\tau_p \tag{9.7.3}$$

where p and n are the free carrier densities, p_t and n_t are the densities of trapped carriers, and τ_n and τ_p are the free carrier lifetimes. If the traps are in thermal contact with the bands,

$$n_t = n\left(\frac{N_{tn}}{N_c}\right) \exp\left(\frac{E_c - E_{tn}}{kT}\right) \tag{9.7.4}$$

$$p_t = p\left(\frac{N_{tp}}{N_v}\right) \exp\left(\frac{E_{tp} - E_v}{kT}\right) \tag{9.7.5}$$

where N_{tn} and N_{tp} are the densities of the traps which are in thermal contact with the conduction and the valence bands, respectively, and E_{tn} and E_{tp} are their energies. N_c and N_v are the effective densities of states, and E_c and E_v are the energies of the conduction and valence band, respectively.

From the energy level diagram of Figure 9.2.2b, where shallow levels in Cr:GaAs are shown, it is seen that at room temperature $kT \gg (E_c - E_{tn})$,

$(E_{tp} - E_v)$. Using the values of N_c and N_v as given in (9.3.6) and (9.3.7), and using $N_{tn} \sim 10^{16} cm^{-3}$ and $N_{tp} \sim 3 \times 10^{16}$ (from Figures 9.2.1 and 9.2.2b) we find

$$\frac{n_t}{n} = \frac{N_{tn}}{N_c} \simeq 0.02 \tag{9.7.6}$$

and

$$\frac{p_t}{p} = \frac{N_{tp}}{N_v} \simeq 0.003 \tag{9.7.7}$$

Consequently $\tau_{dn} \simeq \tau_n$ and $\tau_{dp} \simeq \tau_p$, even if the trapping time is shorter than the recombination time. If the recombination time is shorter, as might be the case in the Cr:GaAs, then trap-controlled decay will start long after most of the excess carrier density has already decayed in the manner of a trap-free material.

9.8 Excess Carrier Lifetime in Cr:GaAs: Bulk Calculations and Steady State Measurements

In Section 8.4, we saw that the photoconductivity of Cr:GaAs, following carrier excitation by an optical picosecond pulse of wavelength $\lambda = 6100\text{Å}$, decayed to its 1/e peak value in about 67 psec. In this section we compare our experimental photocarrier decay time with the electron lifetime in Cr:GaAs, calculated by the formulas developed in Section 9.6 and measured under continuous illumination with longer wavelengths.

i) Calculation of the carrier lifetime by the recombination center formalism

Immediately after the picosecond pulse illumination, the electron and hole densities are equal. Since the conductive electrons are about

twenty times more mobile than holes (see Section 9.4), they carry the major part of the photocurrent until their density decays to about one twentieth of the holes' density. Therefore, if $\tau_p < \tau_n$, the observed photocurrent transient is the result of the electron density decay, and the experimental results should be compared to τ_n. Moreover, since it will be shown that the calculated lifetimes are much longer than the observed 67 psec decay time, it is enough to compare it to τ_n even if $\tau_p > \tau_n$.

Under the conditions of our experiment, the electron lifetime in Cr:GaAs due to recombination through the Cr center was shown in Section 9.6 to be given by (9.6.36), i.e.,

$$\tau_n \simeq \frac{1.15}{\sigma_n v_n N_t} \tag{9.8.1}$$

In (9.8.1) σ_n is the electron capture cross section, v_n is the thermal velocity given by $\sqrt{3kT/m_n^*} \simeq 4.5 \times 10^7$ cm/sec at room temperature, and N_t is the recombination center density.

Assume first the Cr level near the center of the energy gap (Figure 9.2.2). In both n- and p-type Cr:GaAs, the electron cross section is $\sim 3 \times 10^{-17} cm^2$ [39]. If we assume a Cr concentration of $10^{17} cm^{-3}$ (see Section 9.3), then $\tau_n^{Cr} \simeq 8$ nsec, which is much longer than the 67 psec photoconductive decay time observed by us.

If (9.8.1) is assumed valid, several explanations are possible to accommodate the inconsistency with the observation: a) The cross section is higher, (b) the trap concentration is higher, (c) other impurity levels assist in shortening the carrier lifetime, (d) other recombination channels, rather than through recombination centers are active. We are

not in a position to judge the nominal values of the cross section. The same is true with regard to the trap concentration. If the mass spectroscopy analysis (see Section 9.2) is reliable, then $10^{17}cm^{-3}$ is above the average Cr concentration reported (see Figure 9.2.1). It is possible, though, that other impurity levels assist in the recombination process, such as the level associated with oxygen which lies near the center of the gap (see Figure 9.2.2). This level cannot be ignored in explaining photoelectronic properties of Cr:GaAs, as pointed out in Section 9.3.

The electron capture cross section of the oxygen impurity level is expected to be large, as the dopant is a donor and mostly ionized (see Figure 9.2.2). Lang and Logan [42] measured this cross section in LPE n-type Cr:GaAs to be $\sigma_n = 2 \times 10^{-16}cm^3$. Using this number and $N_t = 10^{17}cm^{-3}$ in (9.6.28) we find $\tau_n^o = 5.4$ nsec. Here, too, the uncertainty in σ_n and N_t makes this estimate rough. However, some support to this value of τ_n is given by lifetime measurements performed on high resistivity unintentionally doped n-type Cr:GaAs which gave $5 \text{ ns} < \tau_n < 0.2 \mu s$ [50c,51]. It is common to identify deep levels in this material as associated with oxygen (see footnote in Section 9.2).

Since the electron lifetime due to recombination through centers is not shorter than a few nanoseconds, the contribution of the radiative band to band recombination should also be considered. The electron lifetime due to that process alone is $\tau_{bb} \simeq 3$ nsec [52].

If we assume the three recombination processes to be uncoupled from each other (see Section 9.7), then we can roughly estimate the

electron lifetime by

$$\frac{1}{\tau_{n,tot}} = \frac{1}{\tau_{bb}} + \frac{1}{\tau_n^{Cr}} + \frac{1}{\tau_n^{o}} \qquad (9.8.2)$$

which, for the values found in this section, gives $\tau_{n,tot} \simeq 1.6$ nsec.

ii) Steady state measurements

Under steady state conditions, the carrier lifetime in Cr:GaAs has been calculated from data acquired by measuring the photoconductivity and photomagnetoelectric effects. A carrier lifetime measured under these conditions is generally not expected to be equal to the photocarrier decay time following a δ-function excitation. At steady state, the density of the ionized traps depends on the excitation level, while immediately after δ-function illumination, the state of the traps is essentially the same as in thermal equilibrium. At very high injection levels, such that $p_e, n_e >> N_t, n_o$, the densities of the excess electrons and holes are almost equal to each other. Then, the steady state electron lifetime (9.6.26) is reduced to (9.6.36), which is also the electron lifetime under the conditions of our experiment. Hence, we may compare the photocarrier lifetime observed by us to that reported by Li and Huang [53], who have measured the steady state electron lifetime at very high injection levels to be 250 psec. At lower injection levels, the lifetime is longer [53]. The photoexcitation in this experiment was obtained by a high intensity tungsten light source.

To conclude, in this section we have seen that recombination through deep flaws cannot, by itself, explain the ultrafast photoconduc-

tive decay of Cr:GaAs as observed by us. This ultrashort decay time seems also to disagree with lifetime measurements under continuous illumination with wavelengths longer than 6100Å, the wavelength used in our experiment. In the following chapters, a model which considers both surface and bulk recombination will be shown to resolve this disagreement.

9.9 The Surface Effect on the Measured Photocarrier Lifetime--An Analysis

In our experiment, laser light with wavelength $\lambda = 6100$Å is absorbed in Cr:GaAs within a layer as shallow as ~ 0.23 μm from the surface [54]. As a result, the surface strongly affects the carrier lifetime [59,60]. The allowed energy bands for electrons and holes in semiconductors are calculated under the assumption of an infinite perfect lattice. Imperfections in this ideal structure change this picture. The surface is such an imperfection. Tamm [55] showed that when the Kronig-Penney periodic square-well potential is terminated on one side by a surface potential barrier, there would be discrete allowed levels lying in the forbidden energy gap, corresponding to wave functions localized near the surface. These levels were later studied by Shockley [56], who showed that there would be one surface state for each surface atom, and additional states which arise from impurities and structure defects.

Let the direction normal to the surface be denoted by x, then the carrier flux toward the surface is given by $D_p \frac{\partial p}{\partial x}$ for holes and $D_n \frac{\partial n}{\partial x}$ for electrons, where D is the diffusion coefficient and p and n are the hole and electron densities, respectively. In equilibrium, the carrier flux is

equal to the rate of carrier recombination per unit area. For example, for holes

$$D_p \frac{\partial p}{\partial x} = \sigma_p v_{th} N_{st}[p_s - p_o] \tag{9.9.1}$$

where σ_p is the hole capture cross section, v_{th} is the free electron thermal velocity, N_{st} is the trap surface density (in cm^{-2}), and p_s and p_o are the hole densities at the surface and in the bulk, respectively. A similar equation can be written for electrons. The product $\sigma_p v_{th} N_{st}$ has the dimensions of velocity and is referred to as the surface recombination velocity. To study the evolution of carrier densities near the surface, the appropriate transport equations are solved with (9.9.1) as a boundary condition at the surface. The sample surface recombination velocity is either an adjustable parameter or else it is found by an independent experiment. In this section the transport equation appropriate to our experiment will be derived from the carrier continuity equations. Its solution will be given in the next section, where the surface effect on the observed photoconductive impulse response of our Cr:GaAs samples will be concluded. The reader who is not interested in the detailed derivation may turn directly to Section 9.10.

Generally, the continuity equations for holes and electrons can be written as

$$-\vec{\nabla} \cdot \vec{J}_p + g_p - \frac{p}{\tau_p} = \frac{\partial p}{\partial t} \tag{9.9.2}$$

$$-\vec{\nabla} \cdot \vec{J}_n + g_n - \frac{n}{\tau_n} = \frac{\partial n}{\partial t} \tag{9.9.3}$$

where J is the particle flux, g is the generation rate (in $cm^{-3}\cdot sec^{-1}$), τ is the carrier lifetime, and p and n are the hole and electron densities, respectively. We assume here that the carrier lifetimes τ_n and τ_p are independent of the carrier density (see discussion following (9.6.29)). The particle flux is given by

$$\vec{J}_p = -D_p \vec{\nabla}p + p\mu_p \vec{E} \tag{9.9.4}$$

$$\vec{J}_n = -D_n \vec{\nabla}n - n\mu_n \vec{E} \tag{9.9.5}$$

The first term in each of these equations is the diffusion current, while the second is the drift current. The constant D is the diffusion coefficient. When phonon scattering is dominant, the mean free path of the particle is velocity independent, and it can be shown [57b] that the diffusion coefficients are given by

$$D_n = \frac{\mu_n\ kT}{e} \quad ; \quad D_p = \frac{\mu_p\ kT}{e} \tag{9.9.6}$$

which are called the Einstein relations. By substituting (9.9.4) and (9.9.5) in (9.9.2) and (9.9.3), the continuity equations become

$$D_p\nabla^2 p - \mu_p(\vec{E}\cdot\vec{\nabla}p + p\vec{\nabla}\cdot\vec{E}) + g'_p - (\frac{p}{\tau_p} - \frac{p_o}{\tau_{po}}) = \frac{\partial p}{\partial t} \tag{9.9.7}$$

$$D_n\nabla^2 n + \mu_n(\vec{E}\cdot\vec{\nabla}n + n\vec{\nabla}\cdot E) + g'_n - (\frac{n}{\tau_n} - \frac{n_o}{\tau_{no}}) = \frac{\partial n}{\partial t} \tag{9.9.8}$$

in which the subscript "o" designates thermal equilibrium, $g'_n = g_n - g_o$, and $g'_p = g_p - g_o$ ($g_o = n_o/\tau_{no} = p_o/\tau_{po}$). The field $\vec{E}$ in (9.9.7) and (9.9.8) is the sum of the applied and the internal fields

$$\vec{E} = \vec{E}_{int} + \vec{E}_{app} \tag{9.9.9}$$

Since $\vec{\nabla}\cdot\vec{E} = \rho/\varepsilon$ and $\vec{E}_{app}$ is uniform, we have

$$\vec{\nabla}\cdot\vec{E}_{int} = \frac{e}{\varepsilon}\,(p-n + N_d^+ - N_a^-) \tag{9.9.10}$$

There is no general analytical solution to these equations. A solution does exist, though, in the case of charge neutrality, i.e., $n(x) = p(x)$. It is not immediately obvious that this assumption is valid for our Cr:GaAs samples. Consider, for instance, the Debye length

$$L_D = \sqrt{D\varepsilon/\sigma} \tag{9.9.11}$$

which is a characteristic distance within which charge neutrality might be violated. For $D = 10\ cm^2/sec$, $\varepsilon = 12\ \varepsilon_o$, and $f = 1/\sigma = 10^8 \Omega$-cm, the Debye length is $\sim$300 μm, which is on the order of the Cr:GaAs wafer thickness used in our experiment. Equivalently, we may calculate the dielectric relaxation time

$$\tau_d = \varepsilon/\sigma \tag{9.9.12}$$

which is a characteristic time within which any deviation from charge neutrality is ironed out. For the same parameter values as above, we find $\tau_d = 11$ ms, i.e., much longer than the 67 ps photocarrier decay time observed by us (see Section 8.4). Consequently, in general, charge neutrality cannot be assumed in our Cr:GaAs samples. However, the situation is different in our experiment in which excess carriers are generated near the surface in a layer on the order of magnitude of the radiation absorption length, α^{-1}. In this layer the dielectric relaxation time and the Debye

length are shorter than in the bulk, as long as the photoconductivity has not decayed. After the picosecond pulse illumination, the conductivity near the surface can be written as

$$\sigma \simeq e\mu_n n_{eo} e^{-t/\tau_c} \tag{9.9.13}$$

where n_{eo} is the electron density immediately after illumination, and τ_c is the photocarrier lifetime. Substituting (9.9.13) in (9.9.12) gives

$$\tau_d = \frac{\varepsilon}{e\mu_n n_{eo}} e^{t/\tau_c} \tag{9.9.14}$$

Using $\mu_n = 3000\ cm^2/V\cdot sec$ and $n_{eo} = 10^{16} cm^{-3}$, which is a typical initial carrier density in our experiment, the dielectric relaxation time is found to be

$$\tau_d = 0.2\ e^{t/\tau}\ psec \tag{9.9.15}$$

or, equivalently, the Debye length will be given by

$$L_D \simeq 15\ e^{t/2\tau_c}\ nm \tag{9.9.16}$$

For a time period of $t_m \simeq 5\ \tau_c \simeq 350$ psec after the picosecond pulse excitation, and within a layer of thickness $\alpha^{-1} \simeq 0.23\ \mu m$ from the surface, the inequalities $\tau_d << t_m$ and $L_D << \alpha^{-1}$ hold, and we may use the charge neutrality assumption. This approximation will be checked later for consistency with the solution of the continuity equation.

We now apply the charge neutrality approximation to the continuity equations (9.9.7) and (9.9.8). Using, as previously, n_o and p_o for the electron and hole thermal equilibrium densities, and n_e and p_e for the excess carrier densities, we substitute in these equations,

$n = n_o + n_e$ and $p = p_o + p_e$. Then, after some straightforward manipulations, the two continuity equations are merged into a single one, called the ambipolar diffusion equation:

$$D^*\nabla^2 p_e - \mu^*\vec{E} \cdot \vec{\nabla} p_e + g' - \frac{p_e}{\tau} = \frac{\partial p_e}{\partial \tau} \tag{9.9.17}$$

where

$$D^* = \frac{(n+p)D_n D_p}{nD_n + pD_p} = \frac{(n_o + p_o + 2p_e)D_n D_p}{(n_o+n_e)D_n + (p_o+p_e)D_p} \tag{9.9.18}$$

is the ambipolar diffusion coefficient, and

$$\mu^* = \frac{(n_o-p_o)\mu_n\mu_p}{n\mu_n + p\mu_p} = \frac{(n_o-p_o)\ \mu_n\mu_p}{(n_o+n_e)\mu_n + (p_o+p_e)\mu_p} \tag{9.9.19}$$

is the ambipolar mobility. The excess carrier lifetime τ is defined by

$$\frac{p_e}{\tau} = \frac{p_o + p_e}{\tau_p} - \frac{p_o}{\tau_{po}} = \frac{n_o + n_e}{\tau_n} - \frac{n_o}{\tau_{no}} \tag{9.9.20}$$

where the subscript "o" designates thermal equilibrium. Since we assume $n_e \simeq p_e$, we may use p_e as the unknown variable without loss of generality. Note that in spite of the charge neutrality assumption, we do not neglect the internal electric field which is built in the material as a result of unbalanced charge distributions. On the contrary, this field is responsible for the ambipolar diffusion, as it prevents a large separation of the positive and negative charge distributions, thus forcing them to move together.

In our experiment, we measured the conductivity of a Cr:GaAs sample which was determined by the total carrier density rather than by

its exact spatial distribution. The applied electric field was parallel to the sample surface and was typically about 3000 V/cm. The electrode spacing was 100 μm, which implied an electron transit time of about 1 nsec and hole transit time of about 18 nsec. Since the photocarriers decayed within ∿67 psec, we may assume that the applied field did not significantly affect the total density of excess carriers. Consequently, we will treat the transport problem as one dimensional, i.e., if x is the direction normal to the surface, (9.9.17) becomes

$$D^* \frac{\partial^2}{\partial x^2} p_e - \mu^* E_{in} \frac{\partial}{\partial x} p_e + g' - \frac{p_e}{\tau} = \frac{\partial p_e}{\partial \tau} \tag{9.9.21}$$

Under the experimental injection levels $p_e, n_e >> n_o, p_o$ so that the ambipolar diffusion coefficient (9.9.18) can be approximated by

$$D^* \simeq \frac{2D_n D_p}{D_n + D_p} \tag{9.9.22}$$

and the ambipolar mobility by

$$\mu^* \simeq \frac{n_o - p_o}{p_e} \frac{\mu_n \mu_p}{\mu_n + \mu_p} \tag{9.9.23}$$

Since $p_e >> n_o, p_o$, the ambipolar mobility is very small and it is possible to simplify equation (9.9.21) by neglecting its drift term as compared to the diffusion term. To justify this step, assume first that $\frac{\partial p_e}{\partial t} = 0$, $g' = 0$, and $E = 0$; then (9.9.21) becomes

$$\frac{\partial^2 p_e}{\partial x^2} - \frac{p_e}{D^* \tau} = 0 \tag{9.9.24}$$

so that

$$p_e \sim e^{-x/L_D} \tag{9.9.25}$$

where $L_D = \sqrt{D^*\tau}$ is the diffusion length. Assume now $\frac{\partial p_e}{\partial t} = 0$, $g' = 0$, $D^* = 0$, then

$$\frac{\partial p_e}{\partial x} + \frac{p_e}{\mu^* E \tau} = 0 \tag{9.9.26}$$

or

$$p_e \sim e^{-x/\mu^* E\tau} \tag{9.9.27}$$

Comparing (9.9.25) to (9.9.27) shows that as long as $\mu^* E\tau << \sqrt{D^*\tau}$ or

$$|E| << \frac{1}{|\mu^*|} \sqrt{D^*/\tau} \tag{9.9.28}$$

holds, we may neglect the effect of the electric field on the excess carrier distribution. Referring to our experiment, if the x-direction is normal to the surface, then the electric field in (9.9.28) is mostly due to the internal field. Therefore, we will show that (9.9.28) is satisfied by the internal field.

To estimate the ambipolar mobility we take $|n_o - p_o| = 10^6 cm^{-3}$ (see Section 9.3), $p_{eo} = 10^{16} cm^{-3}$, $\mu_n = 3000\ cm^2/V\cdot sec$, and $\mu_p = 167\ cm^2/V\cdot sec$, then from (9.9.23)

$$|\mu^*| = 1.6 \times 10^{-8} cm^2/V\cdot sec \tag{9.9.29}$$

From the Einstein relations (9.9.6), $D_n = 78\ cm^2/sec$ and $D_p = 4.3\ cm^2/sec$, so that

$$D^* = 8.2\ cm^2/sec \tag{9.9.30}$$

Using (9.9.28), (9.9.30), and $\tau = 300$ psec (see next section) as the bulk recombination time, the right-hand side of (9.9.28) is

$$\frac{1}{|\mu^*|}\sqrt{\frac{D^*}{\tau}} = 1 \times 10^{13} \text{ V/cm} \tag{9.9.31}$$

To estimate the internal field, so as to compare it with (9.9.31), we use the fact that no net current flows normal to the surface because there is not an external electric field in this direction. As a result the electron flux is equal to the hole flux, so that from equation (9.9.4) and (9.9.5)

$$0 = e(J_{px} - J_{nx}) = -e(D_p - D_n)\frac{\partial p_e}{\partial x} + \sigma E_{in} \tag{9.9.32}$$

where σ is the conductivity. Solving for E_{in} and using the Einstein relations (9.9.6) and $\sigma = e\mu_n p_e(1+\frac{1}{b})$, we find

$$E_{in} = -\frac{kT}{e}\frac{b-1}{b+1}\frac{1}{p_e}\frac{\partial}{\partial x}p_e \tag{9.9.33}$$

To get an estimate of E_{in}, we assume $p_e = p_{eo}\, e^{-\alpha x}$, where for $\lambda = 6100\text{Å}$ in Cr:GaAs $\alpha = 4.35 \times 10^4 \text{cm}^{-1}$ [54] so that for the mobility ratio $b = 18$ we obtain

$$|E_{in}| = 1 \times 10^3 \text{ V/cm} \tag{9.9.34}$$

Comparing (9.9.34) with (9.9.31) we see that the strong inequality of (9.9.28) holds, and as a result we may neglect the drift term in (9.9.21). The transport equation now becomes

$$D^*\frac{\partial^2}{\partial x^2}p_e + g' - \frac{p_e}{\tau} = \frac{\partial}{\partial t}p_e \tag{9.9.35}$$

It will be solved in the following section. However, first we would like to evaluate the charge neutrality assumption which has led to this ambipolar diffusion equation.

Earlier in this section, it was stated that the charge neutrality assumption would not be used in calculating the internal electric field, since then its divergence would vanish [see (9.9.10)]. To evaluate the charge neutrality assumption we will calculate the departure from this neutrality which is required to set up the internal field. From Poisson's equation and (9.9.33) we have

$$\frac{\partial}{\partial x} E_{in} = \rho/\varepsilon = e \frac{p_e - n_e}{\varepsilon} = - \frac{kT}{e} \frac{b-1}{nb+p} \frac{\partial^2}{\partial x^2} p_e \tag{9.9.36}$$

or

$$\left| \frac{p_e - n_e}{p_e} \right| = \left| L_{Di}^2 \frac{n_i (b-1)}{nb+p} \frac{1}{p_e} \frac{\partial^2}{\partial x^2} p_e \right| \tag{9.9.37}$$

where L_{Di} is the intrinsic Debye length given by

$$L_{Di} = \sqrt{\frac{kT\varepsilon}{e^2 n_i}} \tag{9.9.38}$$

Since $n_e \simeq p_e >> n_o, p_o$, equation (9.9.37) can be approximated by

$$\left| \frac{p_e - n_e}{p_e} \right| = \left| L_{Di}^2 \frac{n_i}{p_e} \frac{b-1}{b+1} \frac{1}{p_e} \frac{\partial^2}{\partial x^2} p_e \right| \tag{9.9.39}$$

To evaluate (9.9.39), p_e is found from the ambipolar diffusion equation. If, as a result, we find that $\left| \frac{p_e - n_e}{p_e} \right| << 1$, then the charge neutrality assumption and the internal electric field are consistent. To get an estimate of (9.9.39), we calculate it at $t = 0$, i.e., when $p_e = p_{eo} e^{-\alpha x}$. At that time (9.9.39) is given by

$$\left| \frac{p_e - n_e}{p_e} \right| = \alpha^2 L_{Di}^2 \frac{n_i}{p_{eo}} e^{\alpha x} \frac{b-1}{b+1} \tag{9.9.40}$$

In GaAs, at room temperature $n_i = 2.3 \times 10^6 cm^{-3}$, so that for $p_{eo} = 10^{16} cm^{-3}$ as in our experiment, (9.9.40) is calculated to be

$$\left|\frac{p_e - n_e}{p_e}\right| \simeq 3 \times 10^{-2}\, e^{\alpha x} \tag{9.9.41}$$

Therefore, in a layer of about $\alpha^{-1} = 0.23\ \mu m$

$$\left|\frac{p_e - n_e}{p_e}\right| << 1 \tag{9.9.42}$$

so that in this layer charge neutrality is a good assumption.

To summarize this section, we have shown that the ambipolar diffusion equation in the form of (9.9.35) can be used to describe the temporal and spatial evolution of the photocarrier density involved in our experiment. To derive that equation, we applied the charge neutrality approximation to the electron and hole continuity equations. This was after we had shown that it was applicable within the light absorption depth α^{-1}, and during a time period of about five times the photocarrier decay time, τ_c, following the picosecond pulse excitation. In the next section, the solution of the transport equation will be given and the surface effect on our experimental results will be concluded.

9.10 The Surface Effect on the Measured Photocarrier Lifetime--Conclusion

In the previous section we derived the transport equation which describes the excess carrier evolution in our Cr:GaAs sample following picosecond pulse excitation. In this section the solution of this equation will be given and the surface effect on the observed photocarrier lifetime

of Cr:GaAs will be determined. It will be shown that surface recombination can explain the seeming disagreement between our experimental results and steady state measurements (see Section 9.8).

The transport equation (9.9.35) can be written as

$$\frac{\partial}{\partial t} p_e = D^* \frac{\partial^2}{\partial x^2} p_e - \frac{p_e}{\tau} + g\, f(t)\, e^{-\alpha x} \tag{9.10.1}$$

where we take a time and space dependent generation function $g\, f(t)e^{-\alpha x}$, which accounts for the absorption of the radiation in the Cr:GaAs sample, and for the temporal profile of the illumination. The boundary conditions of the solution are

$$\text{a)} \qquad p_e(0,t) = \frac{D^*}{s} \frac{\partial}{\partial x} p_e \Big|_{x=0}$$

$$\text{b)} \qquad p_e(\infty,t) = 0$$

$$\text{c)} \qquad p(x,0) = 0 \tag{9.10.2}$$

where s is the surface recombination velocity introduced in Section 9.9. A general solution of (9.10.1) is [58]

$$p_e(x,t) = g \int_0^t f(t-\theta)\, \phi(x,\theta)\, e^{-\theta/\tau}\, d\theta \tag{9.10.3}$$

where

$$\phi(x,\theta) = e^{-x^2/4D^*\theta} \left\{ \frac{1}{2} \left[w\left(\alpha\sqrt{D^*\theta} - \frac{x}{2\sqrt{D^*\theta}}\right) + \frac{\alpha D^* + s}{\alpha D^* - s}\, w\left(\alpha\sqrt{D^*\theta} + \frac{x}{2\sqrt{D^*\theta}}\right) \right] - \frac{s}{\alpha D^* - s}\, w\left(s\sqrt{\theta/D^*} + \frac{x}{2\sqrt{D^*\theta}}\right) \right\} \tag{9.10.4}$$

and

$$w(z) \equiv e^{z^2}\ \mathrm{erfc}(z) \tag{9.10.5}$$

Under the conditions of our experiment, we may assume a δ-function generation, i.e., $f(t) = \delta(t)$. Thus

$$p_e(x,t) = g\ \phi(x,t)\ e^{-t/\tau} \tag{9.10.6}$$

Recall that $n_e \simeq p_e$, so that (9.10.6) describes the evolution of the electron and hole density distribution in a layer $\sim\alpha^{-1} = 0.23\ \mu m$ from the surface during a time period of about 350 psec following the picosecond pulse illumination (see Section 9.9, following equation (9.9.16)). The function $\phi(x,t)$ is plotted in Figure 9.10.1 as a function of x at various times after the excitation. Notice that to obtain the carrier density distribution each curve has to be multiplied by $e^{-t/\tau}$, with the appropriate bulk carrier lifetime, τ. The values used for s and D will be discussed shortly.

The conductivity of the Cr:GaAs sample is given by

$$\sigma(t) = e(\mu_n n_e(t) + \mu_p p_e(t)) \tag{9.10.7}$$

but since $n_e \simeq p_e$,

$$\sigma(t) = e(\mu_n + \mu_p)\ p_e(t) \tag{9.10.8}$$

The total hole density is proportional to $\int_{x=0}^{\infty} p_e(x,t)\ dx$, so that

$$\sigma(t) \propto \int_{x=0}^{\infty} p_e(x,t)\ dx \equiv g\ \phi^*(t)\ e^{-t/\tau} \tag{9.10.9}$$

where

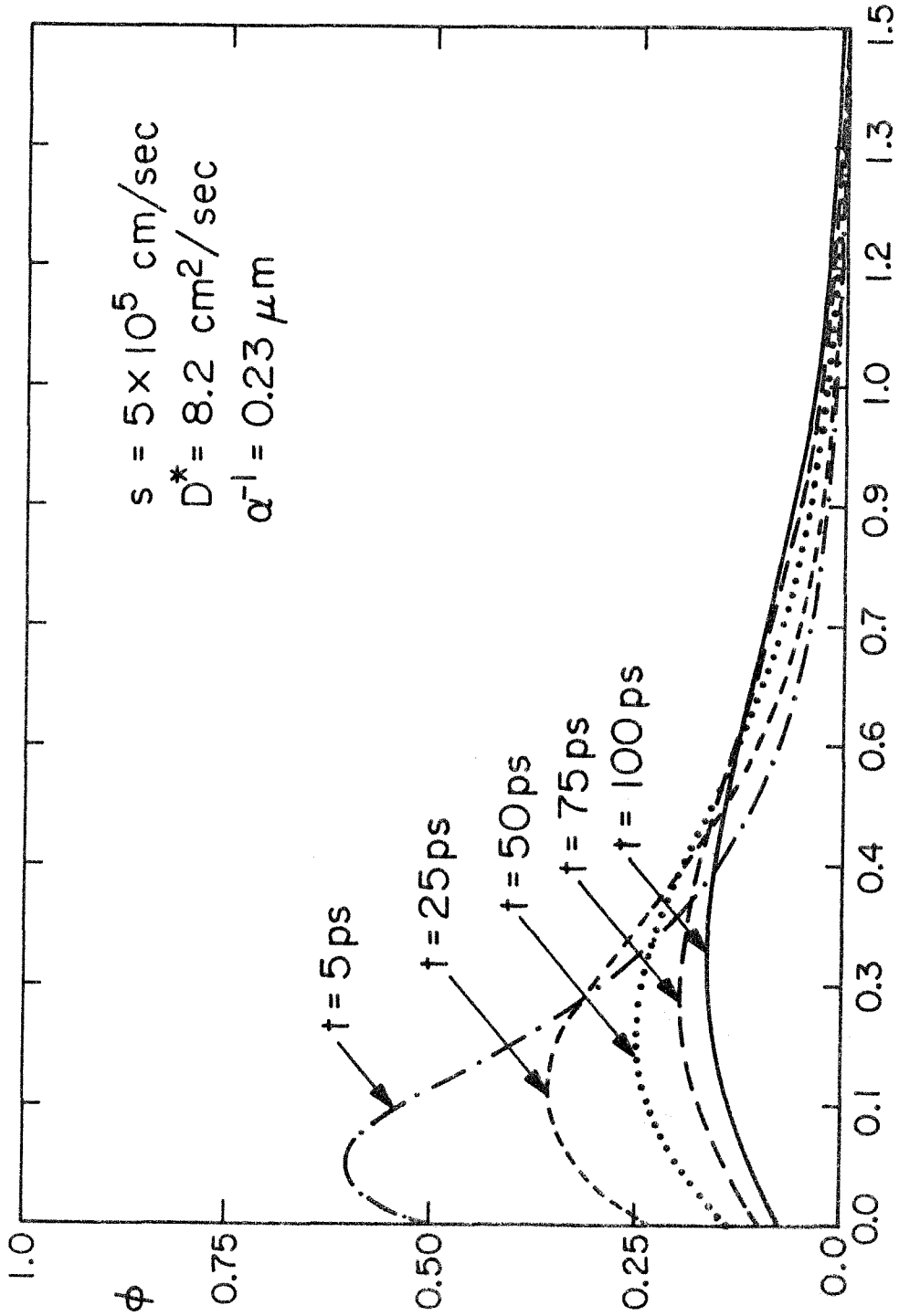

Fig. 9.10.1 Carrier density as a function of depth under the Cr:GaAs surface for infinite bulk recombination time τ, at various times following a picosecond pulse excitation (λ = 6100Å). For finite τ, each curve should be multiplied by $e^{-t/\tau}$.

$$\phi^*(t) = \frac{s}{\alpha(s-\alpha D^*)} w(\alpha\sqrt{D^*t}) - \frac{D^*}{s-\alpha D^*} w(s\sqrt{t/D^*}) \qquad (9.10.10)$$

As expected from (9.10.9) at $t = 0$, $\phi^* = \phi^*_{max} = \alpha^{-1}$. The temporal behavior of the normalized function $\alpha\phi^*(t)$ following a δ-function excitation is plotted in Figure 9.10.2 for various values of surface recombination velocity. The ambipolar diffusion coefficient D* is calculated from (9.9.22) and Einstein's relations (9.9.6) to be 8.2 cm^2/sec ($\phi^*(t)$ is insensitive to the exact value of D*).

Referring to each curve in Figure 9.10.2, we find the appropriate bulk carrier lifetime τ which, together with the respective surface recombination velocity s, yields the measured photoconductive decay time τ_c = 67 psec (see Section 8.4). These pairs of s and τ are tabulated in Table 1.

Table 1

The surface recombination velocity, s, and bulk carrier lifetime, τ, which yield a photoconductive decay time of $\tau_c = (67 \pm 5)$ psec

s (cm/sec)	τ (psec)
1×10^5	78 ± 6
2.5×10^5	94 ± 7
5×10^5	119 ± 9
1×10^6	163 ± 12
5×10^6	375 ± 24
∞	464 ± 35

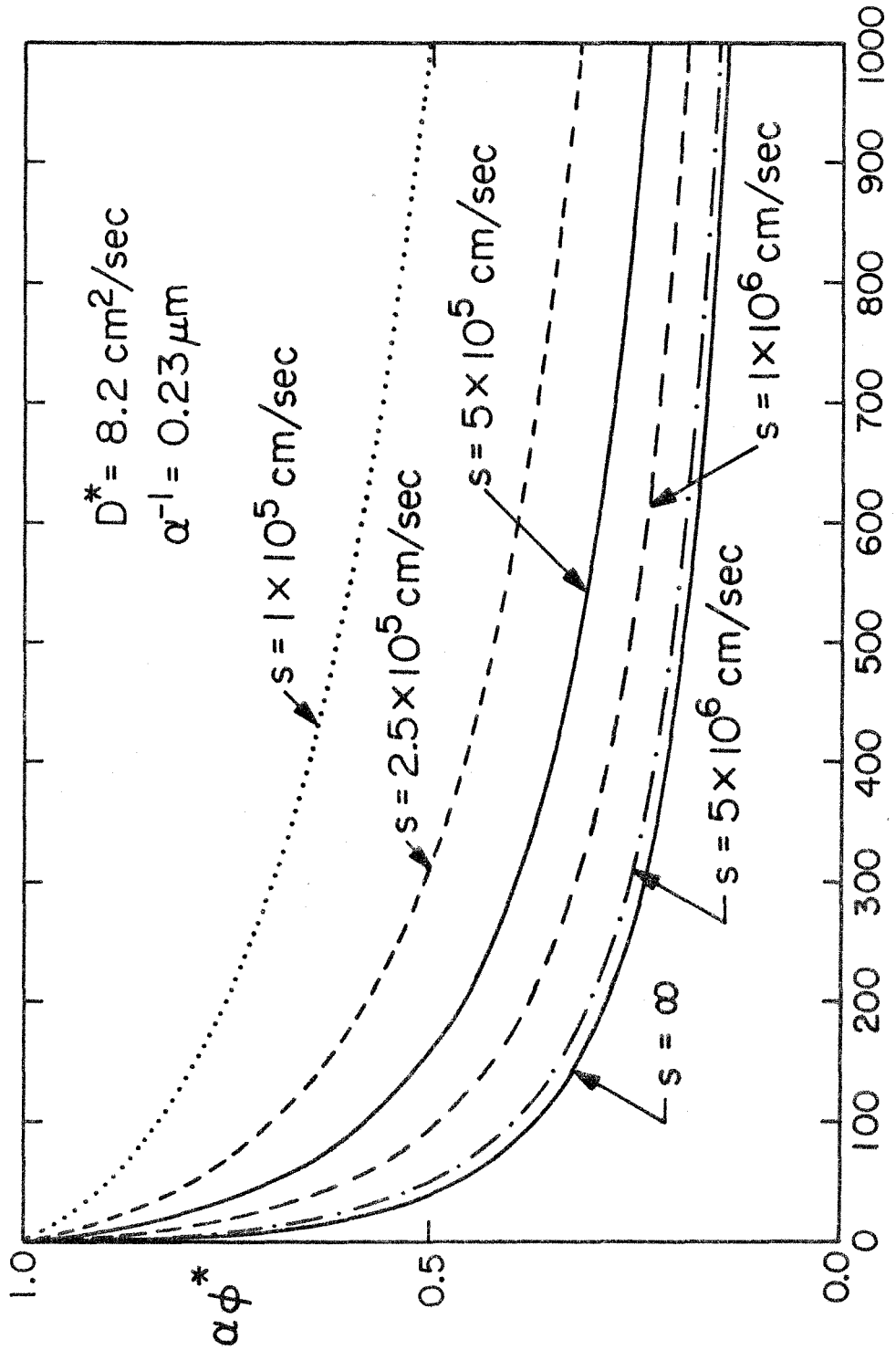

Fig. 9.10.2 The photoconductive impulse response of the Cr:GaAs samples for infinite bulk recombination time τ and various surface recombination velocities. For finite τ, each curve should be multiplied by $e^{-t/\tau}$.

We estimate the surface recombination velocity of our Cr:GaAs samples to be $s \geq 1 \times 10^6$ cm/sec [60]. Accordingly, the bulk lifetime in our samples is ≥ 160 psec. Notice that even if $s = \infty$, the bulk lifetime is short: $\tau \simeq 460$ psec. These values of τ agree well with the carrier lifetime measured with CW illumination near the absorption edge (see Section 9.8).

9.11 Conclusion

In Chapter 7 an experiment was described in which the photoconductive impulse response of Cr:GaAs has been studied by irradiating the material with a continuous train of picosecond pulses. The photon energy was 2.03 eV, well above the GaAs absorption edge. In Chapter 8 the experimental results were shown to be reliable and the Cr:GaAs photoconductive decay time was deduced to be 67 ± 5 psec.

In this chapter, it has been shown that contrary to interpretations given by previous authors [4], the chromium recombination centers in Cr:GaAs cannot, by themselves, be responsible for the observed short excess carrier lifetime. Instead, a model has been introduced in which both bulk and surface recombination processes are considered. This model explains the ultrafast photocarrier decay in Cr:GaAs, observed by us and by others [3,4], following a picosecond pulse excitation of photocarriers near the surface. It agrees well with the carrier lifetime calculated from the Shockley-Read model and measured with CW radiation near the absorption edge.

References - Part II

1. G. R. Cronin and R. W. Haisty, J. Electrochem. Soc. 111, 874 (1964).
2. P. L. Hower et al. in Semiconductors and Semimetals, ed. by R.K. Willardson and A. C. Beer (Academic Press, New York, 1971), Vol. 7, p. 147.
3. R. A. Lawton and A. Scavannec, Elec. Lett. 11, 74 (1975).
4. C. H. Lee, A. Antonetti, and G. Mourou, Opt. Comm. 21, 158 (1977).
5. a) Omni Spectra, American #26805 (0.010" tab).
   b) " #2043-600 8-00 (0.050" tab)
   c) " #2052-1201 OSM 204 cc
6. Product bulletin for Custom Poly "C", 3M Company, Chelmsford, Mass.
7. Shipley Company, Newton, Mass. 02162.
8. G. H. McCall, Rev. Sci. Instrum. 43, 865(1972).
9. This type of switching unit was suggested by R. H. Moyer.
10. a) Crystal Specialties, Monrovia, Calif.
    b) W. P. Allred, Crystal Specialties - private communication.
11. E. Swiggard, Dept. of the Navy, NRL, Washington, D.C.
12. The Indium Corporation of America, Utica, New York.
13. I. J. Bahl and D. K. Trivedi, Microwave, pp. 174-182 (May 1977).
14. G. D. Vendelin, Microwave Journal, pp. 63-69 (May 1970).
15. A. H. Kwon, Microwave Journal, pp. 61-63 (Jan. 1976).
16. E. O. Hammerstad, Proc. Europ. Micro. Conf. Hamburg (Germany), pp. 268-272 (Sept. 1975).
17. M. V. Schneider, Bell Sys. Tech. J. 48, 1421 (1969).
18. H. R. Kaupp, IEEE Trans. Electronic Computers EC-16, 185 (1967).
19. Somewhat lower and higher values of ε(GaAs) can be found in the literature. See for example, K. C. Champlin and G. H. Glover, Appl. Phys. Lett. 12, 231 (1968).

20. Weinschel Engineering Co, Inc. Gaitherburg, Maryland.

21. W. J. Chidobiak et al., IEEE Trans. MTT, MTT-19, 783 (1971).

22. W. J. Getsinger, IEEE Trans. MTT, MTT-21, 34 (1973).

23. J. D. Jackson, Classical Electrodynamics (John Wiley & Sons, Inc., New York, 1975), p. 303.

24. R. A. Pucel, D. J. Masse, and C. P. Hertwing, IEEE Trans. MTT, MTT-16, 342 (1968), and MTT-16, 1064 (1968).

25. J. D. Welch and W. J. Pratt, NEREM Rec. 8, 100 (1966).

26. M. V. Schneider, Bell Sys. Tech. J. 48, 2325 (1969).

27. M. Maeda, IEEE Trans. MTT, MTT-20, 390 (1972).

28. Y. Rahmat-Samii, T. Itoh, and R. Mittra, IEEE Trans. MTT, MTT-22, 372 (1974).

29. The Microwave Engineering Handbook and Buyers' Guide, New York, Horizon House, Feb. 1969, p. 77.

30. S. Ramo and J. R. Whinnery, Fields and Waves in Modern Radio (John Wiley, New York, 1953), 2d edition, p. 27.

31. T. L. Koch and P. Agmon - unpublished.

32. T. Inoue and M. Ohyama, Solid State Comm. 8, 1309 (1970).

33. M. Abramowitz and I. A. Stegun, Handbook of Mathematical Functions (Dover, Eighth printg.), a) p. 260, eq. 6.5.3; b) p. 297, Fig. 7.1; c) p. 298, eq. 7.1.13.

34. See, for example, S-4, Tektronix instruction manual.

35. G. M. Martin et al., J. Appl. Phys. 50, 467 (1979)

36. A. L. Lin and R. H. Bube, J. Appl. Phys. 47, 1859 (1976).

37. R. Zucca, J. Appl. Phys. 48, 1987 (1977).

38. P. F. Lindquist, J. Appl. Phys. 48, 1262 (1977).

39. W. Plessiewicz, J. Phys. Chem. Solids 38, 1079 (1977).

40. D. C. Look, Solid State Comm. 24, 825 (1977).

41. S. M. Sze and J. C. Irvin, Solid State Elect. 11, 599 (1968).

42. D. V. Lang and R. A. Logan, J. Elect. Mater. 4, 1053 (1975).

43. J. S. Blakemore, Semiconductor Statistics (Pergamon Press, New York, 1962), a) p. 79; b) p. 357; c) p. 283; d) p. 188.

44. R. H. Bube, Photoconductivity of Solids (John Wiley, New York, 1960), p. 263.

45. A. Th. Philadelpheus and P. C. Euthymiou, J. Appl. Phys. 45, 955 (1974).

46. J. I. Pankove, Optical Processes in Semiconductors (Dover, 1971), p. 412.

47. W. Shockley and W. T. Read, Jr., Phys. Rev. 87, 835 (1952).

48. R. N. Hall, Phys. Rev. 87, 387 (1952).

49. Kalashnikov, J. Tech. Phys. USSR 26, 241 (1956).

50. See, for example, O. Madelung, Physics of III-V Compounds (John Wiley, New York, 1964), a) p. 109; b) p. 140; c) p. 220.

51. R. H. Bube, J. Appl. Phys. 31, 315 (1960).

52. R. Dingle and K. F. Rodgers, Jr., Appl. Phys. Lett. 14, 183 (1969); A. V. Dudenkova and V. V. Nikitin, Sov. Phys. Solid State 8, 2432 (1967); see also Ref. [50], p. 220.

53. S. S. Li and C. I. Huang, J. Appl. Phys. 43, 1757 (1972).

54. M. D. Sturge, Phys. Rev. 127, 768 (1962).

55. I. Tamm, Physik Z. Sowjetunion 1, 733 (1932).

56. W. Shockley, Phys. Rev. 56, 317 (1939).

57. J. P. McKelvy, Solid State and Semiconductor Physics (Harper and Row, New York, 1966), a) p. 486; b) p. 324.

58. J. Vaitkus, Phys. Stat. Sol. A 34, 769 (1976).

59. H. Milner-Brown and E. Fortin, Can. J. Phys. 47, 2789 (1969).

60. G. P. Peka and L. G. Shepel, Fiz. Trend. Tela 14, 2340 (1972); (Sov. Phys. Solide State 14, 2025 (1973));
G. P. Peka, S. A. Spektor, and L. P. Shepel, Fiz. Tekh. Poluprovod 9, 1920 (1975 (Sov. Phys. Semicond. 9, 1261 (1976);
G. P. Peka and L. G. Shepel, Fiz. Tekh. Poluprovod 10, 1911 (1976) (Sov. Phys. Semicond. 10, 1140 (1976)).

61. See, for example, R. W. Daniels, Approximation Methods for Electronic Filter Design (McGraw Hill, 1974), Ch. 14-15.

62. A. Rose, Concepts in Photoconductivity and Allied Problems (Interscience Publishers, John Wiley & Sons, New York, 1963), p. 22.